EXPERIMENTAL AND THEORETICAL INVESTIGATIONS OF GLASS SURFACE CHARGING PHENOMENA

BY

GABRIEL AGNELLO

A THESIS

SUBMITTED TO THE FACULTY OF

ALFRED UNIVERSITY

IN PARTIAL FULFILLMENT OF THE REQUIREMENTS
FOR THE DEGREE OF

DOCTOR OF PHILOSOPHY

IN

MATERIALS SCIENCE AND ENGINEERING

ALFRED, NEW YORK

APRIL, 2016

EXPERIMENTAL AND THEORETICAL INVESTIGATIONS OF GLASS SURFACE CHARGING PHENOMENA

BY

GABRIEL AGNELLO

B.A. UNION COLLEGE (2000)

M.S. STATE UNIVERSITY OF NEW YORK AT ALBANY (2004)

SIGNATURE OF AUTHOR_____

APPROVED BY _____
WILLIAM LACOURSE, ADVISOR

_____
ALASTAIR CORMACK, ADVISORY COMMITTEE

_____
ALEXIS CLARE, ADVISORY COMMITTEE

_____
DOREEN EDWARDS, ADVISORY COMMITTEE

_____
CHAIR, ORAL THESIS DEFENSE

ACCEPTED BY _____
DOREEN D. EDWARDS, DEAN
KAZUO INAMORI SCHOOL OF ENGINEERING

ACCEPTED BY _____
NANCY J. EVANGELISTA, ASSOCIATE PROVOST
FOR GRADUATE AND PROFESSIONAL PROGRAMS

ABSTRACT

Charging behavior of multi-component display-type (i.e. low alkali) glass surfaces has been studied using a combination of experimental and theoretical methods. Data obtained by way of a Rolling Sphere Test (RST), streaming/zeta potential and surface energy measurements from commercially available display glass surfaces (Corning EAGLE XG® and Lotus™ XT) suggest that charge accumulation is highly dependent on surface treatment (chemical and/or physical modification) and measurement environment, presumably through reactionary mechanisms at the surface with atmospheric moisture. It has been hypothesized that water dissociation, along with the corresponding hydroxylation of the glass surface, are important processes related to charging in glass-metal contact systems. Classical Molecular Dynamics (MD) simulations, in conjunction with various laboratory based measurements (RST, a newly developed ElectroStatic Gauge (ESG) and Diffuse Reflectance Infrared Fourier Transform Spectroscopy (DRIFTS)) on simpler Calcium AluminoSilicate (CAS) glass surfaces were used to further explore these phenomena. Analysis of simulated high-silica content (≥50%) (CAS) glass structures suggest that controlled variation of bulk chemistry can directly affect surface defect concentrations, such as non-bridging oxygen (NBO), which can be suitable high-energy sites for hydrolysis-type reactions to occur. Calculated NBO surface concentrations correlate well with charge based measurements on laboratory fabricated CAS surfaces. The data suggest that a directional/polar shift in contact-charge transfer occurs at low silica content (≤50%) where the highest concentrations of NBOs are observed. Surface charging sensitivity with respect to NBO concentration decreases as the relative humidity of the measurement environment increases; which should be expected as the highly reactive sites are progressively covered by liquid water layers. DRIFTS analysis of CAS powders expand on this analysis showing a gradual increase in molecular water absorption at the surface in samples containing ≥60% silica, and an abrupt decrease in those with ≤60% silica. This behavior is very likely related to the aforementioned charge polarity shift (negative (-) to positive (+)) in low silica containing glasses, leading to the conclusion that structural defect mediated charge accumulation and/or

transfer are likely to be important mechanisms related to the contact charging of glass surfaces.

For Dad. I miss you every second of every day.

Forward

The following pages largely outline the course of my research and/or life over the past several years, specifically from approximately April 2012 to the present. As with any research effort, the actual work ebbs and flows with the passage of time. Often, the final product does not closely resemble what was originally intended, as is somewhat the case with this dissertation. For clarity, I felt it necessary to provide some context for what will follow, namely explanations for how the project was initiated, how those close to it technically became involved, and details on how the chronological order of the research, as it is presented, took form.

On April 10th, 2012 my father had a massive stroke and passed away. One of the last conversations I ever had with him was about how I had made the decision to return to school and finish my PhD; something that I had begun some 8 years earlier but had never finished. Being a doctor himself (M.D.) he was absolutely thrilled, and only wished that he could help in some way, whether that be monetarily or just purely through fatherly support. For a few months after his death, I was just desperately trying to pick up the pieces of my seemingly shattered life. While we didn't see eye to eye on most things, he was one of my best friends in the truest sense of the word. Around June-July of that year, I decided to pick myself up and pursue what clearly made him so happy just weeks before he died. I decided to choose Alfred University for several reasons, the most important of which being that Alfred has a world renowned glass science program and I work for Corning Incorporated…..it seemed like a perfect fit. I applied for the PhD program in materials engineering and was accepted for the fall term of 2012. Two main obstacles lay before me that had to be overcome before I could begin my program. The first of which was to find a project that was attractive to Corning from a business/commercial perspective while at the same time had enough fundamental space within it to produce a worthwhile academic thesis that would satisfy Alfred's interests. The second obstacle was to convince my directorate at Corning that all of this was worth funding a PhD student. As it turned out, these two things were directly linked.

Due to a restructuring in Corning R&D, I was transferred to a new position with different management precisely when I was due to start part time (1 class per semester) at Alfred. With the university's help and understanding, I was given a postponement of admission until fall of the following year so I could get my work situation in order. This turned out to be a blessing in disguise, as it gave me more time to explore potential PhD projects while I established my worth to new management. Over the course of 2013, I had countless meetings with directors, managers and technical experts in various groups/departments all over Corning with the express purpose of finding an area that had academic as well as industrial promise. Over the same span of time, I had successfully contributed to several projects which lead to my director agreeing to fund one class per semester, so I had the go ahead to officially start the program on a part time basis. I felt like this was "victory #1 for the good guys!" but I knew there was much more to do for me to get the nod for full time funding. I needed to step up my search for a project at Corning, if that was indeed the route I was going to take, so that is exactly what I did.

In late 2013, it came to my attention that there was an ongoing issue we were having with various customers that had to do with unwanted charging of glass when put through panel manufacturing processes. After speaking with several of my colleagues that were involved in different facets of the effort to solve the problem, it became apparent to me that very little was known from a fundamental perspective on *why* and *how* glass surfaces charge when put into contact with other surfaces. This seemed surprising to me considering how commonly electrostatic attraction/charging can be observed in the real world, but sometimes the greatest types of discoveries can come from concepts often considered mundane or unimportant. I decided that this was the area I was going to focus my efforts on. I drafted a proposal that included basic theory/background of glass contact electrification/charging, commercial impact for Corning along with why we should care about learning about contact electrification on a deep fundamental level, example experiments with key outcomes and logistics/timing/funding. This document was placed on several directors' and managers' desks in early spring of 2014.

At this time, I was taking a class taught by Professor LaCourse on the surface properties of glasses. The content of the course, along with Dr. LaCourse's deep background in glass and/or surface science, lead me to think that he would be a perfect faculty member to oversee/advise the research. I shared my ideas with him one day after class while we sat in the library. He thought the overall field had much potential and indicated that he would be happy to take me on as an advisee. Now that I had obtained faculty support at Alfred for my proposal, I began to run experiments (with the assumption that Corning would eventually approve my PhD funding) looking at Corning glass' surface charging behavior under variable conditions, namely surface treatment and/or environment (relative humidity). Fortunately, there was already a funded project in Corning Display Development (CDT) with the ultimate goal of finding a surface engineering based solution for charge accumulation, so these experiments fit quite nicely into an already established scope. The primary hypothesis for my thesis came directly out of these early experiments; namely that a glass surface's propensity to accumulate/dissipate charge is closely related to its ability to cause close proximity water to dissociate. Simply put, the more reactive a glass surface is the more it will charge under a contact scenario. Corning management officially approved my research proposal in August, 2014 and I enrolled as a full time graduate student for the fall semester. My long time plan of attempting to link my job directly to my PhD research was finally realized.

As part of the PhD program at Alfred, I needed to take a couple of core courses that did not transfer from my previous graduate transcript. One of these was "defects and defect related processes", that was taught by Prof. Cormack. Over the course of the class, it dawned on me that highly reactive surface sites, such as under-coordinated network formers and/or non-bridging oxygens (NBO) may be the primary vehicles for charge accumulation. After a literature search, I realized that one of the best (and only) ways to study defect mediated reaction with water at a glass surface was through Molecular Dynamics (MD), and it turned out that my current professor was a world leader in this area! After class in the early fall, I sat down with Prof. Cormack to share my current results with him and to propose an MD study to study the relationship between glass charging and surface-water reactivity. He was immediately interested in

the prospect, so in late 2014 I officially began to work part time under Dr. Cormack learning the “art” of MD. For the target material system, we chose a set of calcium aluminosilicate (CAS) compositions, with the thought being that a ternary system would be easier to work with then the complicated, multi-component ones typical of Corning Incorporated display glasses. This also served the dual purpose of making the research less of an IP concern for my employer, therefore making it easier to publish the results. While the eventual goal of surface study appeared to be “simple” when stated in conversation, I found out relatively quickly that nothing could be further from the truth. Over the course of the next year, significant efforts were put forth to optimize bulk glass structure generation to ensure that surfaces generated from these bulk glasses would be acceptable. Key areas that were addressed were the optimization of cooling rates, and the vetting of macroscopic structural properties such as radial/angular distributions and structural defect/coordination states. Final “vacuum fracture” generation of quality CAS surfaces was completed in 10-15 with the next step being the study of reactionary dynamics.

With the MD model surfaces completed, the final piece of the “puzzle” was the comparison of model properties/predictions (such as native coordination states at the surfaces and reactivity with close proximity water) with experimental measurements of CAS surfaces created in the lab. Representative surfaces of the target compositions were generated in 11-15. Primary experiments/measurements made on laboratory surfaces included Rolling Sphere Testing (RST), Electrostatic Gauge (ESG) measurements (ESG is a new measurement technology developed to study glass contact electrification phenomena), surface resistivity and Diffuse Reflectance Infrared Fourier Transform Spectroscopy (DRIFTS). All of these measurements were made under variable humidity and/or temperature. Final comparison(s) between our simulated and experimental results on the CAS ternary system and its application to the original charge transfer hypothesis resulted from these experiments. This work was completed in early 2016.

Taking into account the information/timeline presented here, this dissertation is spaced over five chapters, and where upon conclusion there is a "closing remarks and future directions" section:

Chapter 1: Brief theoretical basis for glass surface charging/conduction, potential transfer mechanisms and contact electrification in the real world. This was the first half of my original proposal for research, as provided to Corning management/technical leadership as well as my thesis committee at Alfred University.

Chapter 2: Investigation of contact-induced charging kinetics on variably modified glass surfaces. This chapter outlines initial experimentation on multicomponent glass surfaces to explore charging kinetics. The primary hypothesis of glass surface-water reactions driving contact electrification came from this work.

Chapter 3: Coordination state and defect evolution in SiO_2 structures formed under variable cooling conditions via molecular-dynamics (MD) simulation. This chapter is the first of two detailing the MD component of my research. Here, structure generation is discussed with specific attention given to cooling rate effects on final structure properties. Structural defect states (coordination defects) are specifically examined, where evolutionary trends based on temperature changes are explored.

Chapter 4: Bulk and surface structure of silica rich calcium aluminosilicate (CAS) glasses along the molar $CaO/Al_2O_3 = 1$ join via Molecular Dynamics (MD) simulation. This is the second of two MD based chapters, where learnings from chapter 3 are applied to generate the target set of CAS structures. Bulk properties of the simulations are vetted against those reported in the literature for both theoretical as well as experimental studies. Surfaces created using the vetted bulk structures are analyzed for defect densities.

Chapter 5: Triboelectric properties of Calcium Aluminosilicate (CAS) glass surfaces. This final chapter is centered on a comparison between the MD results and complementary measurements made on laboratory fabricated CAS surfaces. Circling back around, we discuss how these results relate to our original hypotheses detailed in chapter 1.

Finally, I would like to take this opportunity to thank those in my life who made this work possible, for without you a few of the most fruitful and productive years of my professional/scientific life would not have happened.

- Drs. Doreen Edwards, William LaCourse and Alastair Cormack: If the three of you hadn't helped me fashion the path I took to get here, then none of this would have been possible.
- Correy Ustanik: If Correy, as my manager, had not been supportive of my dream to complete this program, there is virtually no way Corning would have supported me.
- Drs. James Hamilton, Nicholas Smith and Robert Manley: As technical advisors/program managers on the Corning end, they helped shape and guide my experiments. Success of this work is partially due to them.
- A.J. Lamphere: A.J. really helped me get on my feet at Alfred with learning MD, even coming down from Rochester a few times to help me after he graduated.
- My wife Anastatia: Without her constant support and understanding, especially with the birth of my first child, Layne, in December…….well, I don't really want to think about it.

And lastly to the reader, I hope reading what follows provides even a fraction of the enjoyment it gave me to write it.

CHAPTER I: TABLE OF CONTENTS

LIST OF FIGURES

LIST OF TABLES

BRIEF THEORETICAL BASIS FOR GLASS SURFACE CHARGING/CONDUCTION, POTENTIAL TRANSFER MECHANISMS AND CONTACT ELECTRIFICATION IN THE REAL WORLD

Gabriel Agnello

INTRODUCTION

The charging of common surfaces has been a well-known phenomenon to both scientists as well as lay people for nearly all of recorded history. Any child who has rubbed his/or her head with a balloon or scuffed their feet along a carpet and then touched a doorknob is keenly aware of these effects. In the flat panel glass industry, glass surface charging post contact with other surfaces has been a persistent issue since the advent of the technology. Preventative measures have been progressively implemented to avoid contact electrification between sheets after packing, as well as during customer processes (a-Si, p-Si, oxide TFT, ect.) that utilize vacuum chucking and/or conveyance systems. One possible approach to help mitigate the effects of charge accumulation is to roughen the glass surface effectively reducing contact area and leading to a lower surface charge. With this said, it is widely accepted that roughening is not a solution that addresses the fundamental physics governing charge transfer, accumulation and/or transport between surfaces; and will therefore always be a "Band-Aid" approach to fixing the problem. With the accelerating pace towards manufacture of increasingly thinner, as well as higher strain point glasses, it is of paramount importance to gain fundamental understanding of the physics and chemistry involved in these processes, and to propose effective, more educated solutions.

This introduction will be presented in two parts. The first section will aim to establish a fundamental framework for charging and conduction phenomena. Initially, the generalized case for a charged surface in contact with an aqueous solution will be considered. The concepts discussed here will then be applied to a silica surface in

contact with water, where a qualitative model for surface conduction in silica gel will be presented. Conduction on a surface of flat sheet glass in contact with atmosphere (especially display glass with only trace amounts of mobile alkali) should be similar to the presented SiO_2 system. The second section will review charge buildup and transfer mechanisms when glass surfaces come into contact with other surface systems. Common issues arising from contact electrification as well as hypothesized charge transfer mechanisms during contact between insulating surfaces will be discussed.

PART I: SURFACE CHARGING AND CONDUCTION PHENOMENA

Ionic behavior at solid/aqueous solution interface

Figure 1a shows a schematic of an arbitrary charged surface in contact with an aqueous (electrolytic) solution. This is accompanied by a calculation of average electrostatic potential as a function of distance normal to the surface (figure 1b). The ionic activity surrounding this interface is typically referred to as the "electrical double layer" [1,2]. Within this system there are three distinct regions (subsets) of charge [1]:

1. The immediate material surface has a layer of positive charge stemming from covalently bonded cations.
2. Close to the solid surface, some of the counter ions accumulate in an immobile layer, referred to as the "Stern Layer" [3].
3. The remaining anions remain close to the material surface forming a largely mobile diffuse ion "cloud" called the "Gouy-Chapman layer".

The physics of bound and mobile charges in this 3 region system can be described with 3 equations (detailed derivations can be found in refs. 2- 4, 6). The Poisson-Boltzmann equation provides a qualitative description of different ion concentrations found in the Guoy-Chapman layer for a given system [1].

$$\nabla^2\psi_d = \frac{2cze}{\varepsilon_0\varepsilon}\sinh\left(\frac{ze\psi_d}{kT}\right) \quad (1)$$

where ψ_d is the electrical potential corresponding to the localized charge density in the solution, z is a species specific valence parameter and c a parameter that is directly proportional to the concentrations of anionic and cationic species.

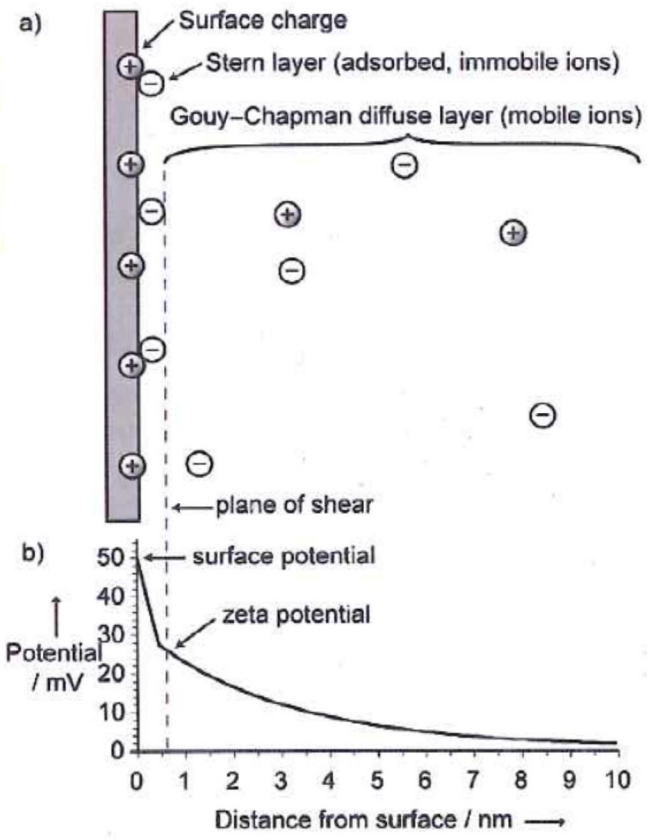

Figure 1: (a) Schematic of "electrical double layer" which can be characterized as a charged solid surface in contact with an aqueous solution. (b) Calculation of average electrostatic potential of model in (a). Discontinuity in potential at the plane of shear is a mathematical artifact and not a real effect. (Ref 1)

Using the P-B equation, one can essentially calculate equilibrium electrical potential anywhere in the solution as well as the effective size of the diffuse ionic region surrounding the surface. The diffuse electrical potential can then be expressed in terms of surface charge density, σ, and Stern layer capacity, C, which is a function of the electrical potential at the surface, ψ_o [5].

$$\psi_d(\sigma) = \frac{1}{\beta e}\ln\frac{-\sigma}{e\Gamma+\sigma} - (pH - pK)\frac{ln10}{\beta e} - \frac{\sigma}{C} \qquad (2)$$

Here, β is inverse KT and Γ is analogous to c in the previous equation (concentration of ionic species). This relation reflects the chemical nature of the interfacial region and it's

charging behavior [5] Assuming the Gouy-Chapman layer can be described by the P-B equation, the Grahame equation can be employed to express surface charge at the interface as a function of the diffuse electrical potential and the Debye screening length parameter, κ [5].

$$\sigma(\psi_d) = \frac{\epsilon\kappa}{2\pi\beta e}\sinh\left(\frac{\beta e\psi_d}{2}\right) \quad (3)$$

Here ϵ refers to the permittivity of the solution and is not to be confused with $\varepsilon_0\varepsilon$ in the P-B equation, which denotes regional dielectric constants. The Debye length (1/κ) is the distance at which the potential is reduced to 1/e the value at the interface [1]. Using these equations in tandem theoretically characterizes the equilibrium of bound and mobile charges throughout the interfacial region in figure 1.

If we designate the solid surface to be that of SiO_2 and the solution to be water, then the primary mechanism for charge buildup is the dissociation of silanol groups [4] given by the reaction

$$SiOH \leftrightarrow SiO^- + H^+ \quad (4)$$

where SiO^- would be the anion and H^+ would be the cation in figure 1, respectively. Using a basic Stern model [3] and the overall approach of equations 1-3, Behrens et al. have calculated the charge density at the SiO_2/H_2O interface [5]. Calculations were made considering two separate systems, one being a flat glass plate and the other being a 1 micron silica sphere (fig 2). The data is expressed as functions of solution pH and is given in terms of “bare” and “effective” values. Bare refers to values obtained from using equations 1-3 directly and effective values involve linearizing equation 3 to account for only areas of the system that are observable in experimental space [5].

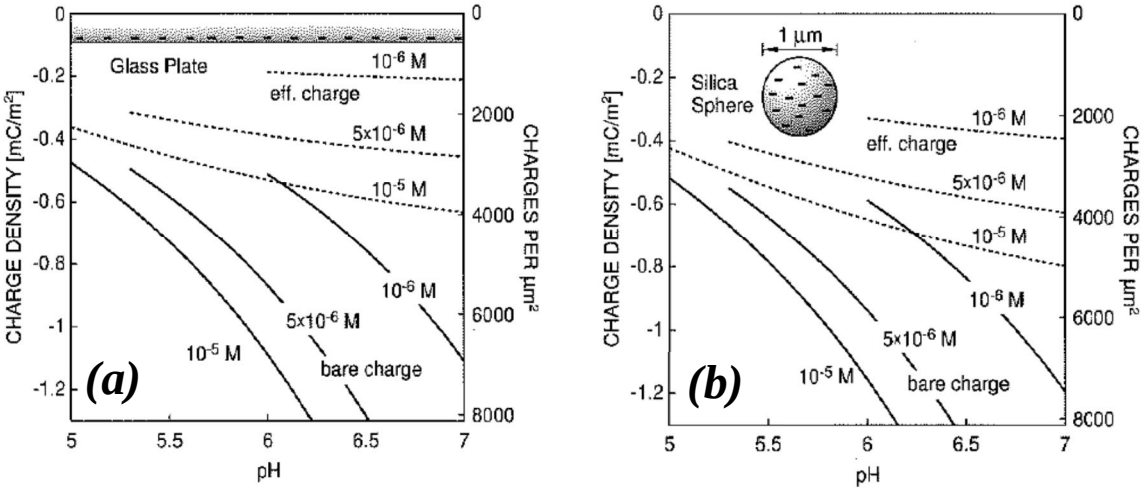

Figure 2: Bare and Effective charge densities calculated for a planar glass surface (a) and a 1 micron silica sphere (b), assuming a density of Γ=8nm^{-1} of chargeable sites, a pK value of 7.5 for silanol dissociation and a Stern capacity of 2.9 F/m^2. (Ref 5)

Conduction mechanisms and charge transfer in silica gel – water systems

The concepts outlined in the first several pages can be applied to the derivation of conduction mechanisms in a silica gel. Anderson et al. studied surface conduction mechanisms in silica gel, specifically how surface conductivity is affected by concentration of absorbed water and surface hydroxyl groups [6]. The authors conducted several experiments using commercially available silica gel, where resistivity and infrared absorption measurements were used to assess effects of surface chemistry and absorbed water on electrical conductivity. Figure 3 shows current-voltage characteristics for silica gel samples exposed to a variety of environmental pre-treatments. Measurements were made under ambient conditions (~19% RH – 25 degrees C). The results indicate that samples heated to temperatures of 250 degrees C or below approximately 12 hours prior to measurement experience a “spike” in generated current above 1.5V. This effect does not occur in the data generated from the 500 degree C sample.

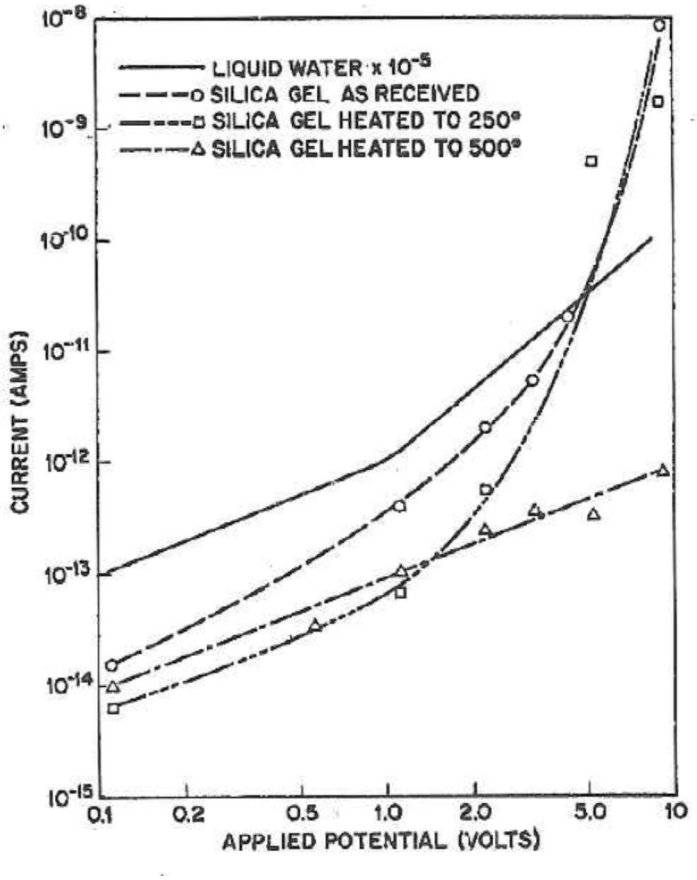

Figure 3: Current-voltage characteristics for silica gel samples subjected to different pre-heat cycles. (Ref 6)

The electrical data matches well with surface composition, where IR spectra has shown the samples heated to 500 degrees C prior to measurement have lower surface hydroxyl concentration and absorb less water than samples heated to lower temperatures (or not at all) [6,7].This effect was confirmed to be reversible after the sample had spent several days under normal atmospheric conditions, leading the authors to conclude that the rapid increase in conductivity seen in figure 2 results from a fully hydroxylated surface that is saturated with absorbed water (i.e. initiation of electrolysis) [6,7]. The authors conducted additional experiments to confirm the existence of ionic transport mechanisms on the silica surface. These experiments produced results suggesting that

the exchange behavior of the hydrated silica gel was very similar to that of aqueous electrolytes [6] (essentially the system discussed in part one of the present article).

Using these results, Anderson and his colleagues developed a qualitative model describing surface conductivity in silica gel as a function of absorbed water molecules, where protons serve as the predominant charge carriers and Si-OH groups are the primary donors. The surface's initial state is assumed to be covered by Si-OH groups which are H-bonded to water molecules [6,8,9]. Both hydroxyl groups as well as water can dissociate to provide mobile protonic charge carriers, where the extent of specific ionization is directly dependent on the amount of water present. The model can be described in 3 distinct transfer regimes, which are characterized by varying proton carrier states (Table 1).

Table 1: Model for Charge Transport in Silica Gel Surfaces in Terms of Protonic Species and Water Surface Coverage (Ref 6)

Table II

Fractional H_2O surface coverage	Favored state of protons	Transport mechanism
$\theta = 0$	H^+	H^+ hopping on SiOH surface
$0 < \theta < 1$	H_3O^+	H_3O^+ diffusion on SiOH surface and H^+ transfer between adjacent H_2O molecules in clusters
$\theta > 1$	$H_3O^+(aq)$	H^+ transfer between adjacent H_2O molecules within a continuous film of water

Conductivity, σ, for any of the three regimes summarized in table 1 can be expressed in terms of carrier concentration (n), mobility (μ) and charge (e) by the following equation [6].

$$\sigma = ne\mu \tag{5}$$

Protons are the dominant carriers in the model, so n is equivalent to the concentration of protons at the surface. Carriers are generated via dissociation of H_2O and/or Si-OH molecules, where these processes are characterized through the appropriate equilibrium constants [6], K_1 and K_2 respectively:

$$K_1 = \frac{(H^+)(OH^-)}{(H_2O)} = exp\left[\frac{-\Delta G_1}{RT}\right] \tag{6}$$

$$K_2 = \frac{(H^+)(SiO^-)}{(SiOH)} = exp\left[\frac{-\Delta G_2}{RT}\right] \tag{7}$$

Along with the charge neutrality requirement $(H^+) = (SiO^-)$ and considering the bounds summarized in table 1, equation 5 can be rewritten as

$$\sigma = e\mu\left[(SiOH)exp\left(\frac{-\Delta G_2}{RT}\right)\right]^{1/2} \tag{8}$$

This generalized equation predicts carrier concentration, as well as conductivity, of a silica gel surface varies directly with surface concentration of water molecules/hydroxyl groups and their ionization energies [6]. The derivation requires one last step involving the rewriting the free energy of dissociation (ΔG) in terms of work required to separate the charged species and energy not related to Coulombic attraction (U).

$$\Delta G = \frac{e^2}{\epsilon r} + U \tag{9}$$

The first term is comprised of electron charge (e), separation of charges in the neutral species (r), and the dielectric constant of the medium (ε). Equations 8 and 9 can be combined to give the final expression for conductivity of the silica gel-water system [6]:

$$\sigma = e\mu(SiOH)^{1/2}exp\left(\frac{-e^2}{2\epsilon rRT}\right)exp\left(\frac{-U}{2RT}\right) \tag{10}$$

Using published data [10] to aid in the calculation of the effective dielectric constant of the gel-water system, the model was validated by comparing measured resistance values of the system and the reciprocals of the calculated dielectric constants (figure 4). The data in figure 4 demonstrates this model to be as effective in describing the silica gel-water system's conduction mechanism as in other cases [11,12]. As glass bulk composition becomes more complex, so do the kinetics at the surface concerning potential carriers and their concentrations; however the basic processes that drive conduction in the simple silica-water system continue to apply.

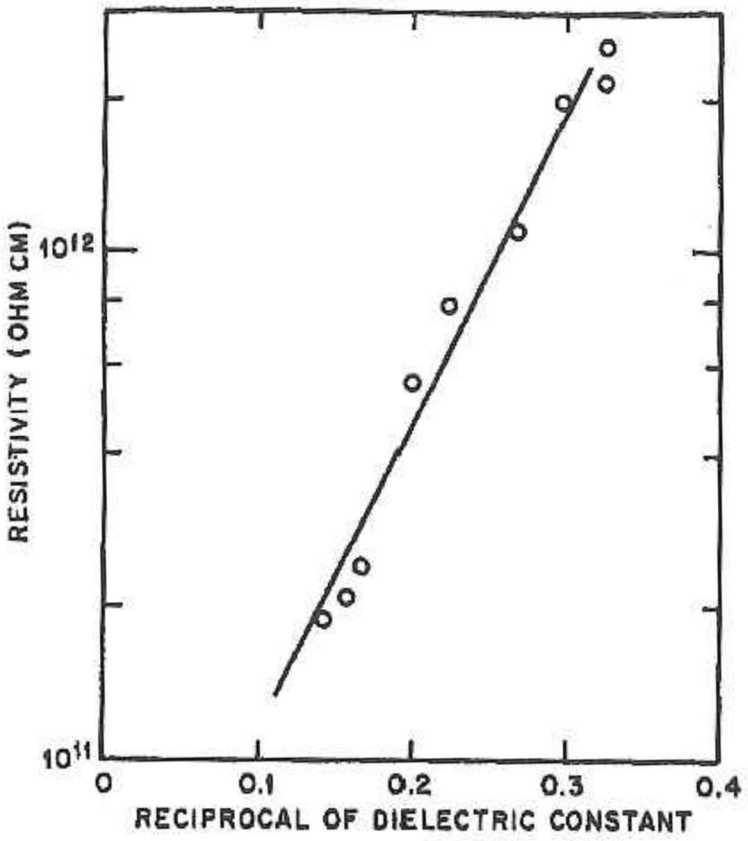

Figure 4: Resistivity of the silica gel system as a function of calculated dielectric constants using published data from ref. 10. (Ref 6)

PART II: CONTACT ELECTRIFICATION INVOLVING GLASS SURFACES – REAL WORLD ISSUES AND PROPOSED CHARGE TRANSFER MECHANISMS

When two unique surface systems (like those discussed in part I) are brought into contact with one another, many issues can and do arise. While the mechanism for charge transfer between two metals (or other conductors) is widely accepted to be electron transfer reflecting the different work functions of the materials [1,13,14], the mechanism(s) between insulators with low carrier mobilities are largely misunderstood [15]. Contact electrification phenomena in these types of systems can cause significant "real world" problems, which I will summarize briefly.

Examples of contact electrification involving glass surfaces

Explosion hazards

One consequence of materials "rubbing" up against each other repeatedly is the buildup of significant charge on the surface. In the presence of a flammable material the spark caused from the electrical discharge can cause an explosion and/or fire. This can be a major issue in granular systems, where fine particles are coupled with an oxygen rich environment that makes combustion a serious risk [15-17].

Dust Storms

Extensive contact electrification can occur during sand and/or dust storms when particulate is lifted by the wind. The amount of material ejected, and consequently the size and intensity of the storm, is directly influenced by the collision of the air born sand grains. These storms have a number of implications such as climate change, desertification and various forms of disease. [15,18-24]

Damage to electronic devices

Electric discharge events originating from contact charging can cause catastrophic failures in electronic devices. This has specific relevance for flat panel glass manufacturing, where the product must be engineered to prevent the buildup of charge during various customer processes. [15]

Proposed mechanisms for contact charge transfer involving glass surfaces

In general, it is believed that charge is transferred from one insulating material to another through one (or a combination) of three mechanisms: electron transfer, ion transfer and/or material transfer. These mechanisms should also dictate transport between glass and metal surfaces, which is the primary system we are interested in here.

Electron transfer mechanism

In general, the electronic structure of an insulator can be characterized by two bands of energy states: a valance band where the available states are all filled and an empty conduction band with energies much higher than the available thermal energy. In this simplified system, it seems impossible for electron transfer to occur. No valence states are available and the conduction band energies are much too high for any electron to transition into [15]. In reality, insulator systems are usually more complex. Defect states can exist at energies between the conduction and valence bands that non-equilibrated electrons can occupy. The existence of occupied trap states have been shown experimentally [25] and are the cause of a measurable conductivity in the material. They also could make contact electrification possible with recent experimental work coming out in support of the model [26-28]. In the specific case of flat panel glass, surfaces can be riddled with physical defects (such as pits/chips) and/or chemical discontinuities; any or all of which may lead to the creation of defect/trap states.

Ion Transfer Mechanism

Ion driven charge transfer upon contact is also plausible, especially for materials with surfaces dominated by a mixture of strongly bound ions and weakly bound mobile ions of opposite polarity. Upon contact, some fraction of the loosely bound ions from the original surface may be transferred to the contacting material leaving behind a net charge of the strongly bound species [15]. Water absorption on the material surface purportedly can play a significant role in the ion transfer mechanism, even in materials without a mobile ion concentration. A popular model incorporating the facilitation of ion transfer through native water layers involves the exchange of absorbed hydroxide ions upon contact of the two surfaces. Experimental support for this transfer mechanism is extensive with many recent reports in the literature [29-32].

Material transfer mechanism

The material transfer mechanism involves the physical transfer of portions of the material surface upon contact. The area of the material being transferred may range in size from a nanometer to micrometer scale. The likelihood of material transfer being the predominant driver of contact electrification is low [15], however it could play some role either directly or indirectly.

Schematic illustrations of the 3 proposed charge transfer mechanisms are shown in figures 5a-c. The most likely scenario is that contact electrification is caused by some combination of the 3 mechanisms; dependent on the different materials' condition, composition and environment.

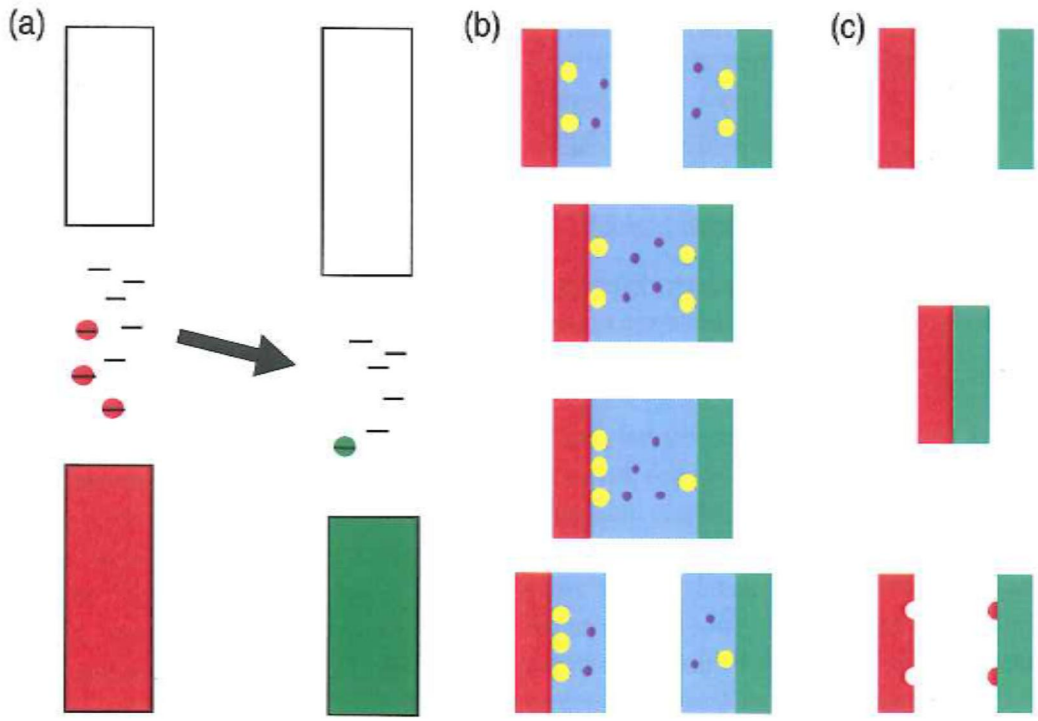

Figure 5: Possible charge transfer mechanisms responsible for contact electrification of insulating materials. (a) Electron transfer – charge is transferred by electrons transitioning from and to defect/trap states. (b) Ion Transfer – charge transfer due to charge redistribution upon contact of surface water layers. (c) Material transfer – charge is transferred by physical exchange of surface material. (Ref 15)

REFERENCES

[1]. L.S. McCarty, G.M. Whitesides, "Electrostatic charging due to separation of ions at interfaces: Contact electrification of ionic electrets," *Angew. Chemie - Int. Ed.*, **47** 2188–2207 (2008).

[2]. A.W. Adamson, *Physical Chemistry of Surfaces*, 6th ed., Wiley, New York, 1997.

[3]. J. Westall, H. Hohl, "A comparison of electrostatic models for the oxide/solution interface," *Adv. Colloid Interface Sci.*,, **12** 265–294 (1980).

[4]. R. K. Iler, *The Chemistry of Silica*, Wiley, New York, 1997.

[5]. S. H. Behrens, D. G. Grier, "The Charge of Glass and Silica Surfaces," *J. Chem. Phys.*, **115** 6716-6721 (2001).

[6]. J.H. Anderson, G.A. Parks, "The Electrical conductivity of Silica Gel in the Presence of Absorbed Water," *J. Chem. Phys.*, **72** [10] 1968.

[7]. J.H. Anderson, (to be published ref. 9 in paper cited as ref. 6 here).

[8]. W.A. Little, *Infrared Spectra of Absorbed Species* Academic Press, London, 1966.

[9]. J.H. Anderson, K.A. Wickersheim, "Near infrared characterization of water and hydroxyl groups on silica surfaces," *Surf. Sci.*, **2** 252–260 (1964).

[10]. J.M. Thorp, "The dielectric behaviour of vapours adsorbed on porous solids," *Trans. Faraday Soc.*, **55** 442–454 (1959).

[11]. R.E. Barker, C.R. Thomas, "Effects of Moisture and High Electric Fields on Conductivity in Alkali-Halide-Doped Cellulose Acetate," *J. Appl. Phys.*, **35,** (1964).

[12]. B. Rosenberg, *Physical Processes in Radiation Biology*, Academic Press Inc., New York, 1964.

[13]. W.R. Harper, *Contact and Frictional Electrification*, Laplacian Press, Morgan Hill, California, 1998.

[14]. J. Lowell, A.C. Rose-Innes, "Contact electrification," *Adv. Phys.*, **29** 947–1023 (1980).

[15]. D.J. Lacks, R. Mohan Sankaran, "Contact electrification of insulating materials," *J. Phys. D. Appl. Phys.* **44**, (2011).

[16]. M. Glor, "Hazards due to electrostatic charging of powders," *J. Electrostat.,* **16** 175–191(1985).

[17]. M. Nifuku, T. Ishikawa, T. Sasaki, "Static electrification phenomena in pneumatic transportation of coal," *J. Electrostat.,* **23** 45–54 (1989).

[18]. C.D. Stow, "Dust and storm electrification," *Weather*, **24**, (1969).

[19]. H.F. Eden, B. Vonnegut, "Electrical Breakdown Caused by Dust Motion in Low-Pressure Atmospheres: Considerations for Mars," *Science,* **180** 962–963 (1973).

[20]. A.A. Mills, "Dust clouds and frictional generation of glow discharges on Mars," *Nature,* **268** 614 (1977).

[21]. J.F. Kok, N.O. Renno, "Electrostatics in Wind-Blown Sand," *Phys. Rev. Lett.,* **100** 14501 (2008).

[22]. Y.J. Kaufman, D. Tanre, O. Boucher, "A satellite view of aerosols in the climate system," *Nature,* **419** 215–223 (2002).

[23]. E. Ganor, Z. Levin, D. Pardess, "Determining the acidity and chemical composition of fog, haze and cloud droplets in Israel," *Atmos. Environ. Part A. Gen. Top.*, **27** 1821–1832 (1993).

[24]. C.L. Bielders, J.-L. Rajot, M. Amadou, "Transport of soil and nutrients by wind in bush fallow land and traditionally managed cultivated fields in the Sahel," *Geoderma.*, **109** 19–39 (2002).

[25]. B. Sultan, K. Labadi, J.-F. Guegan, S. Janicot, "Climate drives the meningitis epidemics onset in west Africa," *PLoS Med.*, **2** (2005).

[26]. C. Liu, A.J. Bard, "Electrostatic electrochemistry at insulators," *Nat Mater.,* **7** 505–509 (2008).

[27]. C. Liu, A.J. Bard, "Chemical Redox Reactions Induced by Cryptoelectrons on a PMMA Surface," *J. Am. Chem. Soc.*, **131** 6397–6401 (2009).

[28]. C. Liu, A.J. Bard, "Electrons on dielectrics and contact electrification," *Chem. Phys. Lett.,* **480** 145–156 (2009).

[29]. T.R.D. Ducati, L.H. Simões, F. Galembeck, “Charge Partitioning at Gas−Solid Interfaces: Humidity Causes Electricity Buildup on Metals,” *Langmuir.*, **26** 13763–13766 (2010).

[30]. Hogue, C.R. Buhler, C.I. Calle, T. Matsuyama, W. Luo, E.E. Groop, “Insulator–insulator contact charging and its relationship to atmospheric pressure,” *J. Electrostat*,,. **61** 259–268 (2004).

[31]. M.D. Hogue, E.R. Mucciolo, C.I. Calle, C.R. Buhler, “Two-phase equilibrium model of insulator–insulator contact charging with electrostatic potential,” *J. Electrostat.*, **63** 179–188 (2005).

[32]. S. Friedle, S.W. Thomas, “Controlling Contact Electrification with Photochromic Polymers,” *Angew. Chemie Int. Ed.*, **49** 7968–7971 (2010).

CHAPTER II: TABLE OF CONTENTS

LIST OF FIGURES

LIST OF TABLES

INVESTIGATION OF CONTACT-INDUCED CHARGING KINETICS ON VARIABLY MODIFIED GLASS SURFACES

G. Agnello[a,b1], J. Hamilton[a], R. Manley[a], E. Streltsova[a], W. LaCourse[b] and A. Cormack[b]

a. Science and Technology Division, Corning Incorporated, Corning, NY 14831, USA
b. New York State College of Ceramics at Alfred University, Alfred, NY 14802, USA

ABSTRACT

The accumulation and dissipation of electrical charge on glass surfaces is of considerable academic and industrial interest. The purpose of the present article, is to report on the differences in charging kinetics of several flat alumina-borosilicate (low alkali content) glass surfaces via a rolling sphere test (RST) [1] that have been physically and/or chemically modified by different approaches and exposed to variable environmental conditions (*i.e.* relative humidity). Methods used for surface modification include chemical etching (HF based chemistries of variable molarity) and plasma processing/thin film deposition (CH_4 via Reactive Ion Etch (RIE) and/or Atmospheric Pressure Plasma Chemical Vapor Deposition (APPCVD)). Trends in glass surface charge rates, along with corresponding surface resistivity, energy and zeta potential measurements indicate that glass surface, and perhaps bulk, chemistry (specifically a surface' reactivity/affinity with/to water) play critical roles in charge dynamics. Based on the results, we propose an ion-based transfer model facilitated by surface-water molecular interactions as the primary mechanism responsible for contact electrification in glass-metal contact systems.

Keywords: Charge, contact, flat glass, electrification, surface

[1] Contact: agnellogp@corning.com

1. INTRODUCTION

1.1 Contact electrification in insulator-metal systems

Within the flat panel display industry, glass substrate charging via metal-glass triboelectrification can lead to highly localized surface potential differences which can adversely affect subsequent device fabrication, performance and ultimately yield. Surprisingly, a detailed understanding of the mechanisms responsible for the charging of flat, low-alkaline, display-type glass surfaces has remained elusive. Thorough experimental studies on the charging behavior of these types of systems are largely absent. While the mechanism for charge transfer between two metals (or other conductors) is widely accepted to be electron transfer reflecting the different work functions of the materials [2-4], the mechanism(s) involving insulators with low carrier mobilities are still largely misunderstood [5]. Several mechanisms for charge transfer in insulating material systems have been proposed in the literature, where wide arrays of both theoretical, as well as experimental hypotheses, are offered. The primary hypotheses involve electronic or ionic charge transfer between metals and insulators, of which many reports have focused on one or both. The classic review text from Lowell and Rose-Innes [4] addresses electron transfer between metals and insulating materials in some detail, citing a number of experiments that offer support for the mechanism based on the linear relationship between insulator charge density and metal work function post contact [9-16]. Generally, it was assumed that thermodynamic equilibrium could be reached between the metal and insulator surface via electronic transfer (*i.e.* electron tunneling [17-19]) bridging the metal Fermi level and "quasi" Fermi level of the insulator [4]. At the time of publication, electron transfer between metals and insulators was widely accepted as the dominant contact charging mechanism [20]; however, limited support for the ionic transfer process did exist. Harper attributed a large contact charge on quartz surfaces to hydroxyl groups at the surface, the concentration of which varied as a function of surface preparation [3,21,22]. Harper, as well as other authors [18,23-25], also had observed that charging was greatly influenced by the presence of water, presumably through an electrolytic process where ions moved through a physi-chemisorbed water layer. This was largely dismissed,

however, due to lack of supporting data. More recent studies have tended to focus more heavily on the prospect of a predominantly ion driven charge transfer. Lowell studied ion driven contact electrification in triglycine sulphate (TGS), a pyroelectric insulating material [26], and came to the conclusion that charge accumulation was unlikely to be driven by the transfer of compensating ions between the materials, even though it was directly related to the polarity and magnitude of mobile ions at the surface. The authors did postulate that ion concentration may alter the electric field at the insulator/metal interface and/or act as acceptors/donors for excess electrons at the surface suggesting the possibility of a dual mechanism being responsible. Charge dependence on surface ion polarity was observed some time later in a metal-polymer system [27], where a detailed ion driven model was proposed. This work agreed qualitatively with another detailed non-equilibrium two-step process involving both electronic and ionic transfer between metals and polymers derived by Lee [28] around the same time. Somewhat surprisingly, the most recent review publications by Lacks, et al. and McCarty et al. [5,29] provide additional references for experimental and/or theoretical studies offering support for one or both transfer mechanisms; however, deeper fundamental understanding of the physics behind these processes has yet to be realized, and many of the questions first posed decades ago still remain.

Contact electrification on multi-component flat glass surfaces, has not been studied as thoroughly as polymer based systems. Such surfaces are of particular importance for those working in the flat panel display industry, where bottom surface (*i.e.* the surface opposite the transistor containing side) charging can lead to device failure and subsequent yield loss [6-8]. It is assumed that the same types of charging mechanisms discussed previously are responsible, though to what degree and in what combination are not known. Lowell studied charge transfer across metal-SiO_2 interfaces [30] and in metal-sodium silicate systems (microscope slides) [31]. Electrification of the SiO_2 surface was observed to be highly dependent on the work function of the contacting metal while that of the soda glass was not. The dependence on metal work function had been previously reported by Davies [13], as well as others [9-16], and

attributed to the equalization of the electron chemical potentials in the two materials[2]. Between pure silica and soda glass, Lowell [31] attributed the differences to the presence of mobile alkali ions which implies that the ionic properties of the surface play a key role in the contact electrification of alkali containing glasses. Furthermore, charging of soda glass surfaces was determined to be highly dependent on exposure to water. This is presumably due to ion exchange or Na dissociation from the glass network. While it was clearly determined that ions played a crucial role in charge transfer, it could not be concluded from these results that the actual transfer of Na^+ ions from the glass to metal was the responsible mechanism due to the discrepancy in the resulting polarity of the glass surface being positive. The authors offered a dual mechanism explanation consisting of electrons and ions, which was a similar approach to most previous studies on non-glass insulators. In this model, the dissociation of NaO led to the formation of Na^+ and O^- ions where the O^- groups acted as electron donors to the contacting metal resulting in a positive glass surface charge. While this explained the sign of the transfer, it did not explain the magnitude, due to the existence of another limiting mechanism, the critical interfacial electric field. This was eventually explained in detail by Lowell [32]. A number of other studies considering metal-flat glass systems have offered similar hypotheses for surface charging behavior [33-38], though no more thoroughly definitive conclusions have been reported.

1.2 Measurement of glass surface charge kinetics

Of the several existing data gaps that exist within this fundamental space, two of the most intriguing are the lack of flat glass (as formed as well as modified) surface charging kinetics (*i.e.* rates of charge accumulation) and studies focusing on low alkali, display type compositional profiles. Some work on polymer [39,40], and polymer-modified glass surfaces [41] was carried out, though the focus was more closely related to magnitude and polarity differences, at constant RH, as opposed to rate variability. To our knowledge, no studies focusing on charge kinetics of variably altered low alkali containing glass surfaces across a range of RH values have been reported. The purpose

[2] Other dielectrics, not glass. Similar conclusions were reached in references 9-16.

of the current work is to study the kinetics of charge accumulation on several alumina borosilicate glass surfaces that have been subject to variable surface modifications. Measurements are conducted via a rolling sphere test (RST), with corresponding surface resistivity, zeta potential and surface energy measurements. Our results strongly suggest that glass surface charge rates are highly dependent on surface (and perhaps bulk) chemistry, modification type and environmental conditions, primarily due to variable surface-water interaction dynamics.

2. EXPERIMENTAL

2.1 Samples and treatments

Two commercially available low alkali glass surfaces, EAGLE XG® (EXG) and Corning Lotus™ XT (LXT), were chosen for the present investigation. Representative surfaces of each composition were washed with a commercially available alkaline detergent for 12 minutes (w/ ultrasonic agitation) at 70 °C, followed by a DI water rinse for 12 minutes at 70 °C before, as well as after, treatment[3]. Experimental matrices detailing the various surface-treatment combinations used for the present study are shown in Tables 1 and 2. Treatment #1 and #2 in Table 1 were chosen based on similar roughening profiles, though it was anticipated that the effects due to their alternate chemistries may be measurably different, from a charging prospective. Regarding the second portion of the study summarized in Table 2, treatments were chosen to represent a range of different thin film chemistry and fractional surface coverage. Methane (CH_4) plasma treated surfaces were processed using two separate methods. In the first case, EXG samples were exposed to CH_4 plasma at atmospheric pressure (AP), 200 W, 200 sccm in a custom-made AP plasma system. A mixture of Ar and He was used for precursor carrier gas, at flows of 18 slm and 2 slm, respectively. All flow rates were controlled via commercially available mass flow controllers. Plasma processing led to the formation of amorphous hydrocarbon polymer films consisting of variable length C_xH_y chains on the glass surface. Surface coverage was increased via repeated travel underneath the gas injection system at a speed of 25 mm/s. Three degrees of surface coverage were studied, corresponding to one, two and four passes through the deposition zone. The second set of CH_4 treated surfaces was processed in an Oxford System100 ICP380 reactor operated in Reactive Ion Etch (RIE) mode in controlled H_2/CH_4 plasma for 60 s. Chamber pressure and plasma power were held at 25 mTorr and 275 W, respectively. APPCVD and RIE processes resulted in C_xH_y films with identical chemistry, as confirmed via ToF-SIMS analysis. The RIE process was designated to target a comparable level of surface coverage/film thickness to the 1 pass

[3] Only table 1 surfaces were rewashed after treatment.

(1P) APPCVD process, with the intention of generating an additional sample with the same film but with modified/functionalized surface chemistry. This was accomplished by exposing the resultant RIE film to a N_2/O_2 plasma (10 mTorr, 300 W) for 5 s. The additional plasma exposure functionalized the outermost layer of the polymer by adding polar NH_2, as well as various carboxyl/carbonyl and hydroxyl, groups to the surface as the hydrocarbon oxidized and began to ablate [42]. The effects of specific plasma treatments on glass surface chemistry were studied extensively through XPS and ToF-SIMS analysis.

Table 2: Experimental Matrix for Wet Chemical Treatments on EXG and LXT Surfaces. *Charge Rate and Surface Resistivity Were Measured at Variable Relative Humidity

Table 3: Experimental Matrix for Plasma/Thin Film Treatments on EXG Surfaces. +Charge Rate Measured Only at Low (<10%) Relative Humidity

Table 1: wet chemical etchants

Surfaces	Treatments	Measurements
EAGLE XG®	Untreated	Charge rate (RST)* Surface resistivity Zeta potential Surface Energy
	Treatment #1 – HF based etchant with lower molarity	
	Treatment #2 - HF based etchant with higher molarity	
LOTUS™ XT	untreated	
	Treatment #1 - HF based etchant with lower molarity	
	Treatment #2 - HF based etchant with higher molarity	

Table 2: plasma/thin film treatments

Surfaces	Treatments	Measurements
EAGLE XG®	Untreated	Charge rate (RST)+ Zeta potential Surface energy
	CH_4 plasma (via APPCVD and RIE)	
	$CH_4 + N_2 + O_2$ plasma (RIE)	

2.2 Measurement techniques

2.2.1 Rolling Sphere Test (RST)

The experimental apparatus used for the measurement of surface charge kinetics was based on a method originally developed by Wiles *et al.* [1], where a small metal sphere, under the influence of a rotating magnetic field, is placed on a surface and allowed to accumulate charge via contact electrification. The magnetic field at the surface is generated by a bar magnet (field strength ~ 80G @ 5.5mm below sample surface as measured by a cylindrical gauss meter) mounted to a stepper motor (Lin engineering) used to provide magnet rotation. A special Teflon housing secures the magnet in a non-conducting contact environment (Fig. 1a). For sample mounting, a Teflon fixture was designed for use with 150 mm round samples consisting of a toroid-shaped base with three support posts mounted to the top surface (Fig. 1b). Glass placement on top of the support posts put the bottom glass surface approximately 2mm from the electrode support (bridging structure in figs. 1b and c) and 5.5 mm from the magnet, the surface of which fell slightly below the bottom of the electrode support (Fig 1c). Thin copper foil was used as the electrode material. The system was housed in an electrically shielded, grounded box.

Measurement of charge using the RST proceeded as follows. Magnet rotation induced the sphere (diameter of 3.2mm, 440C stainless steel) to follow the path of the rotating field by rolling across the glass surface in a circular orbit. As it rolled, the sphere and glass surface(s) accumulated positive and negative charges, respectively, via triboelectrification. The sphere's revolution was intersected periodically by the electrode, where it would detect the collective charge on both the sphere and glass (Q_{G+S}) via capacitive coupling. At points in the rotation where the sphere was not located above the electrode, it would only detect the charge specific to the glass surface (Q_G) resulting in a periodic waveform consisting of equally spaced peaks and valleys corresponding to sphere and glass charge (Q_{G+S}) and glass charge only (Q_G) as a function of time. Figure 2a shows sample RST data (magnet speed~1000 RPM, test time~30s) from an untreated EXG surface. Figure 2b shows only the data from 0-10s, with Q_{G+S} and Q_G labeled accordingly. Figure 2c shows the relationship between sphere

motion and the data. These parameters were used for all reported RST measurements. The periodic discontinuities every 5-15 s are due to dielectric breakdown (i.e. charge equalization) through air between the sphere and glass surface when the field at the sphere surface exceeds approximately 30 kV/cm [3, 41, and 43]. This was verified via simple calculations performed across several measurements. Further details regarding concept and operation of the RST can be found in refs. [1], [39-41] and [43].

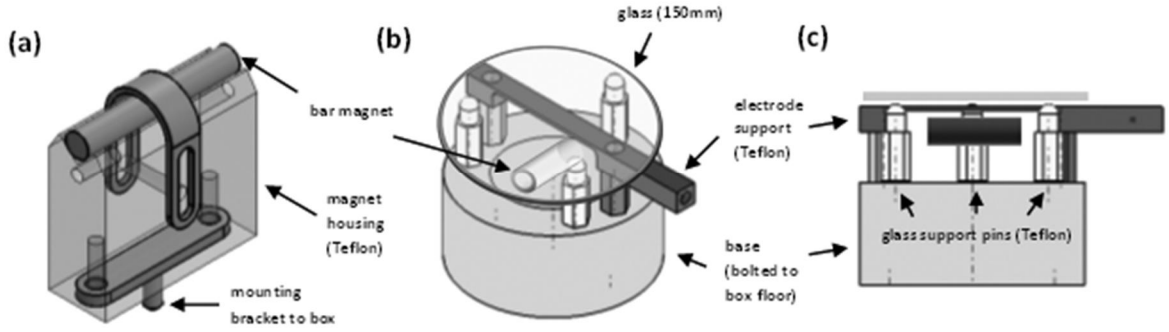

Figure 6: RST structural components (a) Magnet housing (b) Glass/electrode support (c) cross sectional view of support.

Glass charge rates were calculated via linear fitting of the minima (Q_G) prior to initial dielectric breakdown. Fits from three identically prepared surfaces were concatenated for statistical assessment of the data, where calculated standard deviation values are representative of surface variability, as well as method precision. A Keithley model 6514 electrometer operated in medium rate data collection mode (nC scaling) was used for the detection of charge. All RST measurements were made in a humidity and temperature controlled class 10000 cleanroom, fully equipped with source air molecular filtration.

2.2.2 Surface resistivity

Techniques used for the measurement of surface resistivity were based on ASTM standard D-257 and an alternating polarity method developed by Keithley instruments. A Keithley 6517 electrometer was used to detect and measure current, as well as supply an alternate polarity voltage to the sample surface, which was patterned with circular metal electrodes for contacting purposes. The measurement environment

was controlled using an Electro-Tech Systems Model 518 humidity and temperature chamber.

2.2.3 Surface Energy

Surface energy was calculated by fitting contact angle measurements (Kruss-model DSA expert) of three liquids to a theoretical model. The liquids chosen for the contact angle measurements were water, diiodomethane and hexadecane [44]. According to Young's model, the surface energy of a solid can be expressed as a function of the liquid (γ_L), surface-liquid (γ_{SL}) interfacial energies and contact angle (θ) by:

$$\gamma_S = \gamma_L cos\theta + \gamma_{SL} \quad (1)$$

where γ_S and γ_L actually represent thermodynamic energies between the solid/liquid phases and the gaseous phase, respectively. The contact angle, θ, allows for the system to be in thermodynamic equilibrium.

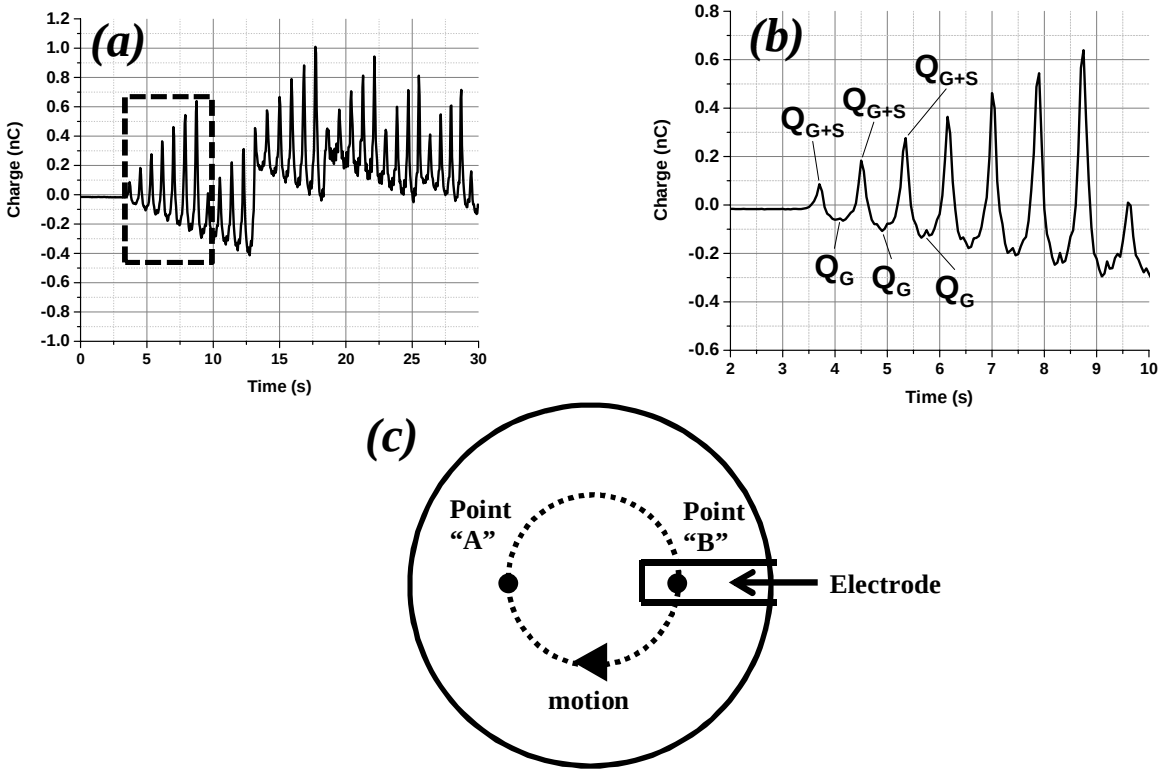

Figure 7: (a) RST data from an untreated EXG surface. (b) Insert in (a) with Q_S and Q_{G+S} labeled accordingly. (c) "Top-down" view of sphere motion. When sphere is at point "B", the electrode detects Q_{G+S} whereas if it is located elsewhere (point "A" for example) the electrode detects Q_G.

The only term in equation 1 that is not measurable experimentally is γ_{SL}, which is why a model fit is required. To estimate the surface-liquid interfacial energy, Wu's model was chosen (equation 2) where the indices D and P refer to the dispersive (London interaction) and polar (Keesom interaction) components of the surface energy, respectively [45].

$$\gamma_{SL} = \gamma_L + \gamma_S - 4\left(\frac{\gamma_S^D \gamma_L^D}{\gamma_S^D + \gamma_L^D} + \frac{\gamma_S^P \gamma_L^P}{\gamma_S^P + \gamma_L^P}\right) \quad (2)$$

By substituting equation 2 into equation 1 and measuring the test liquid contact angles, the polar and dispersive components of the solid surface energy can be calculated. The addition of the two components equals the total surface energy.

2.2.4 Zeta Potential

Zeta potential measurements were made using an Anton Paar SurPASS electrokinetic analyzer. A pH of 5.6 was chosen to emulate normal atmospheric conditions and was achieved using a 1 mM KCl titration maintained at 24.7 °C and 500 mbar.

3. RESULTS

Charge rates at ~8.8% relative humidity for washed, but untreated LXT and EXG surfaces, along with those exposed to treatment #1 and treatment #2 (Table 1), are shown in figure 3. As mentioned previously, charge rates were calculated by measuring three identically prepared surfaces and performing a linear concatenated fit of initial glass charge minima. Error bars represent surface variability confounded with RST precision, so it is reasonable to conclude that treatment #2 had little effect on glass surface charge rates at low humidity, as opposed to treatment #1 which clearly shows a reduction. Charge rates vs. relative humidity for EXG exposed to treatment #1 and treatment #2 as compared to the untreated control data are shown in figures 4a and 4b, respectively. The points at 8.8% are representative of the data plotted in figure 3.

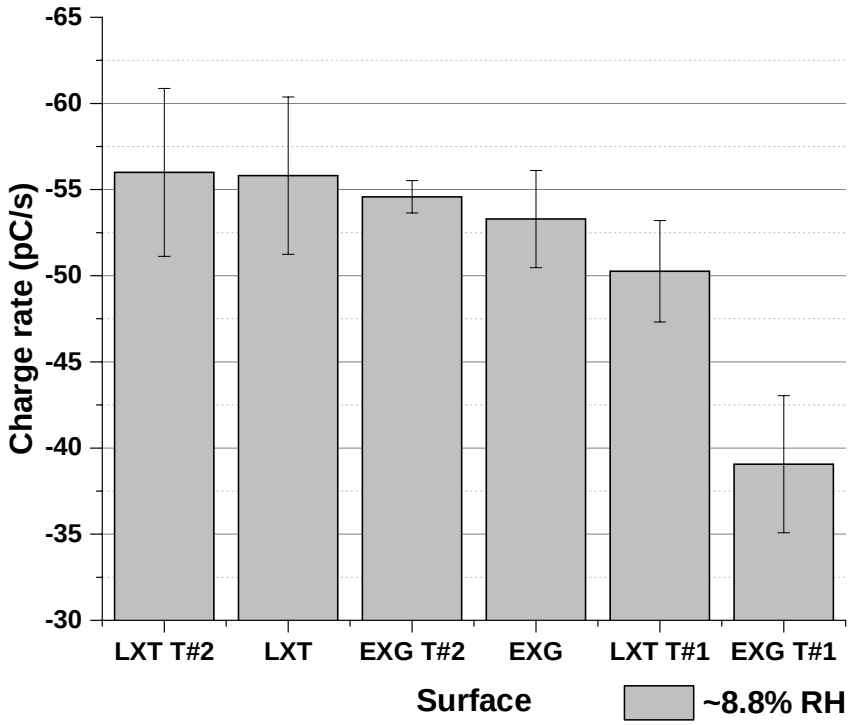

Figure 8: Low relative humidity charge rates of native and chemically treated EXG and LXT surfaces.

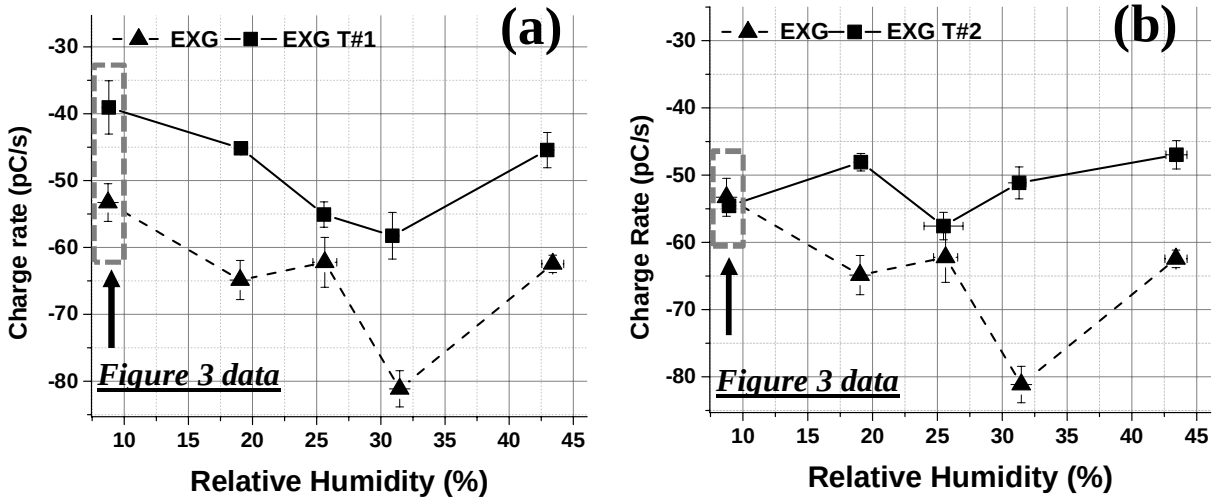

Figure 9: Charge rates vs. RH% for untreated EXG surfaces compared with those exposed to (a) treatment #1 and (b) treatment #2.

Charge rates for untreated EXG surfaces appear to increase initially as relative humidity was increased from approximately 8.8% to 30%, followed by a decrease at higher values. Surfaces that were exposed to treatment #1 exhibited a global decrease in charge rate relative to the untreated surface across the entire measured range of RH, while following the same overall trend of initial increase followed by a >30% RH decrease. Treatment #2 is observed to have a different effect on EXG surface charge rate, displaying a lower overall variability with respect to changing humidity levels. With the exception of the data collected at ~18% RH[4], LXT surfaces (both treated and untreated) exhibited similar charge rate dependence on variable humidity, though the rate increases observed in the 8.8%-30% regime were significantly less pronounced relative to those seen in EXG surface data (figures 5a and b). LXT surfaces exposed to treatment #1 showed a small but measureable increase in charge rate (again, with the exception of the measurement at ~18%) relative to the untreated control in the <30%

[4] It is possible that this observation could correspond to the low to medium humidity (<10-15%) transition seen in surface resistivity data, though RST data does not have high enough fidelity to make a more definitive statement.

RH regime; as was the case with EXG, both samples rates decreased sharply above ~30% RH. Charge rates for LXT treated with formulation #2 were stable in the <30% RH regime, similar to those observed for EXG surfaces but to an even higher degree.

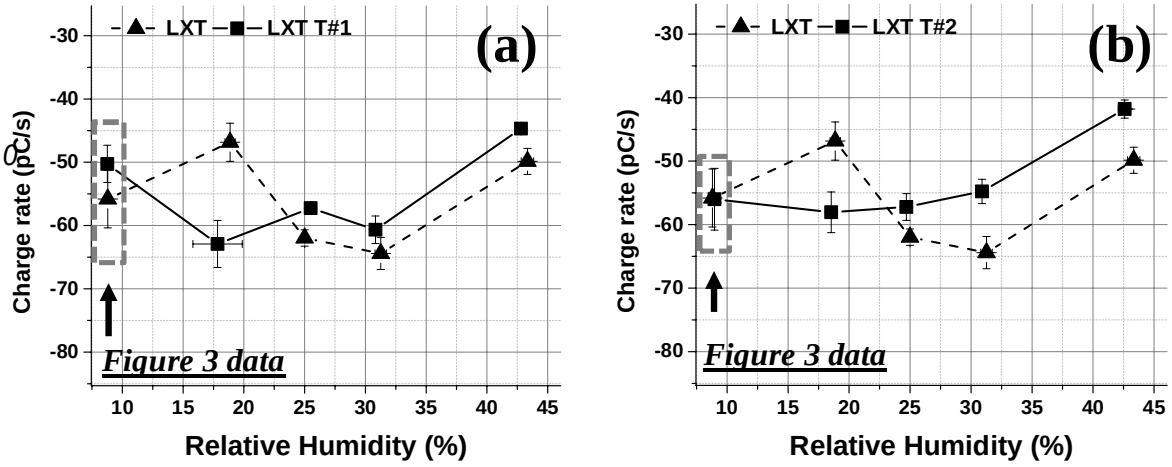

Figure 10: Charge rates vs. RH% for untreated LXT surfaces compared with those exposed to (a) treatment #1 and (b) treatment #2.

As with all other measured samples, both untreated as well as treated (#2) LXT surfaces exhibited a decreased affinity for charge accumulation >30% RH. Surface resistivity measurements made at variable relative humidity on table 1 EXG and LXT surfaces are shown in figure 6a and 6b, respectively.

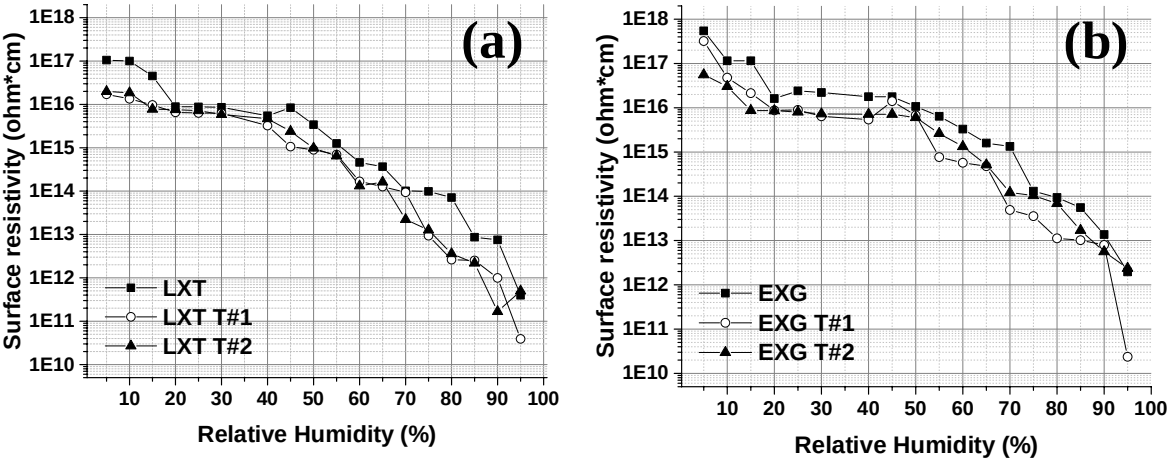

Figure 11: Surface resistivity vs. relative humidity for chemically treated and untreated (a) EXG and (b) LXT surfaces.

The data correlates reasonably well with RST results, though instead of two we observed three distinct electrical regimes corresponding to low (0-15%) and medium (15-40%) and high (>40%) relative humidity values. RST data was not incrementally collected below ~15% with enough resolution for us to detect systematic changes in rate, so we were not able to observe this third low humidity regime, however this will be considered in future experimentation. Nonetheless, it can be reasonably concluded from these results that observed decreases in charge rates at relative humidity values >30% correspond to increases in surface conductivity (though observed at slightly higher values in figures 6a and 6b).

To this point, the data strongly suggests that dynamic interactions between atmospheric moisture and different glass surfaces play crucial roles in the accumulation and transfer of free charge. Charge rate measurements made on the plasma/thin film modified EXG surfaces shown in Table 2 strongly support this hypothesis, even at low relative humidity values. C_xH_y polymer films with variable degrees of fractional surface coverage were deposited onto EXG surfaces using either vacuum based RIE or atmospheric pressure plasma processing. Samples that had been functionalized through additional O_2/N_2 plasma exposure were also tested. Charge rates acquired from these surfaces at ~8.8% RH, along with appropriate label identifiers, are shown in figure 7. From the data in figure 7, we conclude the following:

1. As hydrocarbon surface coverage increases, the charge rate sharply decreases. This effect can be attributed to drastically increasing hydrophobicity as the native glass surface is progressively covered with non-polar C_xH_y groups.
2. The surface's affinity for charge accumulation can be effectively reversed by functionalizing the top-most layer of the polymer through alteration of the surface chemistry.

Surface energy measurements made on Table 2 surfaces that support these conclusions along with simple illustrations depicting the effects of plasma processing on surface chemistry are presented in figures 8a-c, respectively.

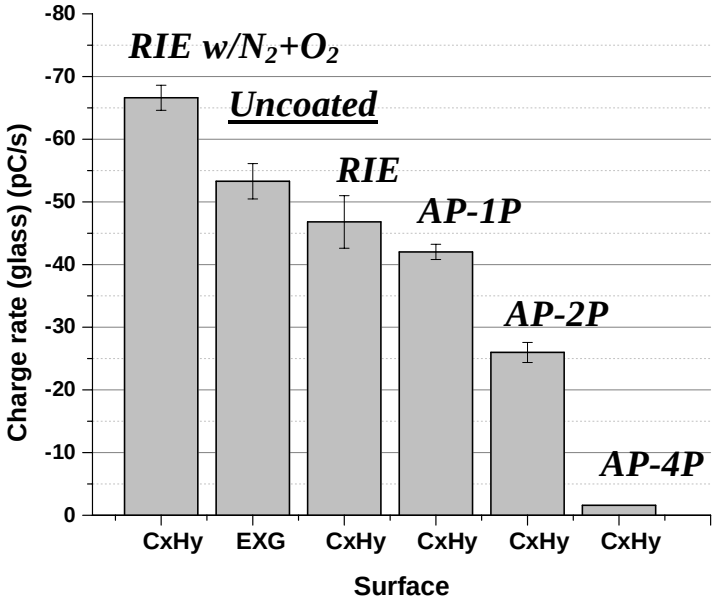

Figure 12: Charge rates for EXG surfaces with variable coverage C_xH_y films. Labels are defined as follows: RIE w/N_2O_2 – Reactive Ion Etch mode CH_4 plasma deposition with 5s N_2+O_2 final step; RIE – CH_4 plasma deposition with no N_2+O_2 step; AP-1P – Atmospheric Pressure Plasma Chemical Vapor Deposition CH_4 (1 pass under injection system); AP-2P – Atmospheric Pressure Plasma Chemical Vapor Deposition CH_4 (2 pass under injection system); AP-4P – Atmospheric Pressure Plasma Chemical Vapor Deposition CH_4 (4 pass under injection system).

The schematics shown in figure 8 are based directly on extensive XPS and TOF-SIMS analysis of the treated surfaces. These results agree qualitatively with previous reports where measured charge rates on polyethylene [39] and polystyrene [40] surfaces decreased in the absence of oxygen containing groups and increased with water absorption due to the reactionary formation of polar groups to minimize the water-polymer interfacial energy [46, 47]. While the O^- containing group based polarization of the current C_xH_y surface was accomplished through intentional means, the ultimate effect on the surface's ability to transfer charge should be the same.

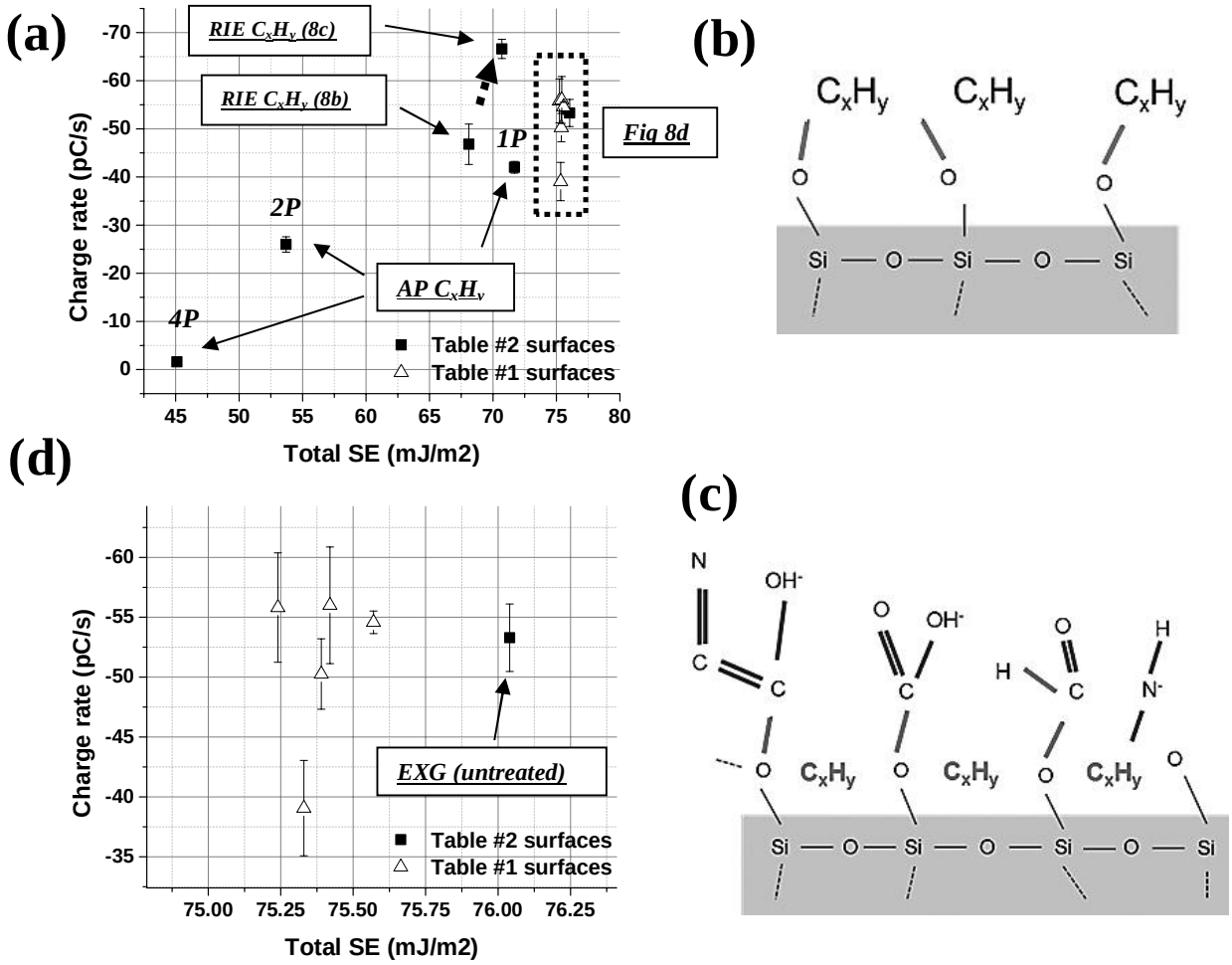

Figure 13: (a) Surface charge rate vs. surface energy for C_xH_y surfaces (table 1 surfaces are open data series). (b) Illustration of non-functionalized polymer surface. (c) Illustration of functionalized polymer surface with polar chemical groups (carbonyl, carboxyl, hydroxyl, amino, etc.) (d) Insert in figure 8a.

The surface energy vs. charge rate relationship is not nearly as strong for the Table #1 surfaces, as the highly clustered data in figure 8a shows; however, the observation that untreated EXG has a slightly higher SE value relative to the other surfaces is particularly curious (detailed view in fig. 8d).

While RST results suggest that EXG and LXT surfaces respond differently to wet chemical based surface modification as well as to changes in measurement environment, there are a few noticeable, and ostensibly important, similarities that were touched on earlier. Charge rates for both untreated surfaces can be characterized by an initial increase at low relative humidity (<30%) followed by an abrupt decrease. The surfaces also exhibit relatively similar reactions to treatment 1 and 2 exposure, where treatment #1 results in an overall decrease in charge rate and treatment #2 (while also slightly decreasing the rate overall) produces a much more stable response with respect to variable humidity. The main difference between EXG and LXT surfaces' response to change (either to their integrity and/or surroundings) is the relative severity of the response (*i.e.* EXG appears to be more sensitive to variable humidity/surface modification relative to LXT). Perhaps the relatively high surface energy of untreated EXG provides a clue. In a further attempt to understand these differences, zeta potential measurements were made on the samples at a neutral, atmospheric-like pH of approximately 5.6. Zeta potential values as functions of charge rate are shown for Tables 1 and 2 surfaces in figure 9 (same labeling scheme as in figs. 8a, 8d)[5]. For Table 2 surfaces, charge rate increases correspond with more negative zeta potential values. Once again, this relationship is an intuitive one and correlates well with previous reports. As the fractional surface coverage of C_xH_y polymer chains increases, oxygen containing groups with negative effective charges are blanketed with non-polar groups and the EXG surface's affinity for charge accumulation via contact electrification decreases. This is logically accompanied by a decrease (*i.e.* less negative) in zeta potential, which is an indication of the net charge at the Stern layer surface. Functionalization of the polymer should result in a zeta potential increase, an increase in surface energy and a corresponding increase in charge rate, which is precisely what the data in figure 9 indicates.

[5] Data was not collected for EXG-T#2, LXT-T#1 or AP-C_xH_y 1P surfaces

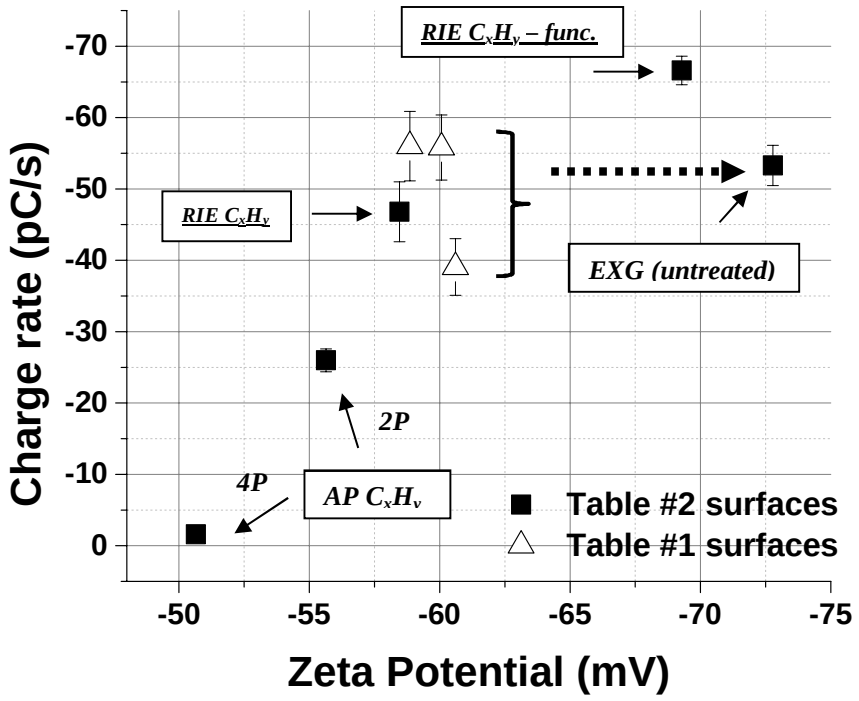

Figure 14: Charge rate vs. zeta potential for table 1 and table 2 surfaces.

The data also suggests a similar discrepancy to that observed for surface energy between zeta potential values of untreated EXG and the rest of Table 1 surfaces. Bar plots showing surface energy and zeta potential values for Table 1 samples are shown in figure 10, where the differences between native EXG and the other studied surfaces are shown. A logical conclusion is that the higher relative surface electronegativity coupled with higher surface energy/polarity of the untreated EXG surface may be directly related with increased sensitivity to surface modification and/or measurement environment relative to LXT. Variation in bulk chemistry of EXG and LXT (i.e. significantly different network modifier/former concentrations) likely impacts respective surface sensitivity to modification and/or environment, so current experimental/theoretical efforts are largely focused in this area.

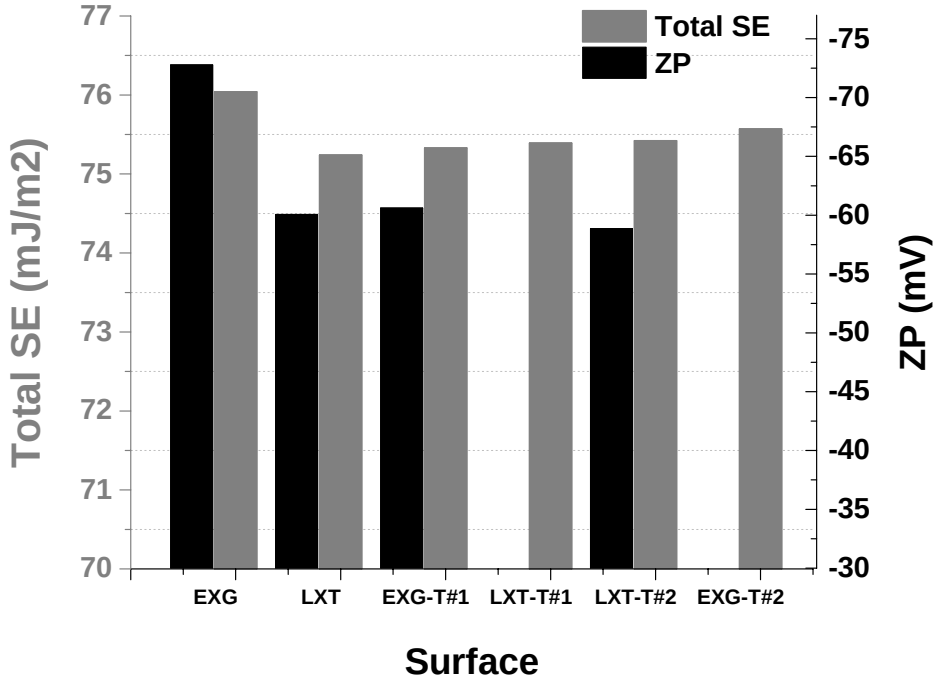

Figure 15: Zeta potential and surface energy for table 1 surfaces. Untreated EXG (far left most bar plots) show significantly lower surface energy and higher zeta potential relative to other surfaces.

Considering this, it is hypothesized that bulk glass chemistry can play a significant role in how glass surfaces charge via triboelectrification. These effects manifest themselves much more keenly in systems where change due to surface modification is more subtle (table 1) as opposed to more drastic (table 2). The hypotheses concerning charge accumulation and/or transfer in glass surface systems are presented in more detail on the following pages.

4. DISCUSSION

One of the main conclusions drawn from our experiments is that glass surface interaction with atmospheric moisture plays a critical role in how a particular surface accumulates charge. Due to a lack of suitable experimental methods, the most commonly utilized tools to study molecular interactions between water and surface systems are classical and/or quantum molecular dynamics simulations. Interactions between water and simple surface compositions (as well as a few more complicated multi-component ones) have been widely studied in the literature, where common chemisorption processes involving the dissociation of molecular water at specific surface sites have been identified. Studies by Du and Cormack [48] and later by Garofalini et al [49,50] examined molecular water interactions with silica surfaces, where the dissociation of molecular water (and associated formation of silanol groups) in close proximity with under-coordinated silicon and/or non-bridging oxygen (NBO) sites was commonly observed. Another observed silanol formation process involved the breaking of strained siloxane bonds at the surface and the formation of an over-coordinated silicon intermediary, offering additional support for the hypothesis that glass surface defect chemistry may play a crucial role in its interaction with atmospheric moisture [49]. Additional reports in the literature have provided evidence that silica [51-54] and sodium silicate [55] surface reactivity with water is directly tied to defect chemistry, specifically concentrations of 3 and 2-fold coordinated Si and non-bridging oxygen (NBO) at the surface. Other groups have made similar calculations on glass surfaces with variable network former and/or modifier concentrations present such as Ca, Al, B, Na, P, ect. [56-60]. They have commonly observed that the amounts of these species present at the surface directly affect defect chemistry in terms of coordination level and NBO concentration amongst others; which, in turn, help to determine a surface's reactivity with water. As a consequence of the increased silanol formation at defect sites, ionic conduction has also been observed to increase via proton hopping from silanol sites to and from adjacent water molecules [49,50], which offers a potentially direct connection to the observed charging behavior in EXG and LXT surface systems. We contend that the variable bulk chemistry inherent to these types of glasses leads directly to different defect concentrations at the surface. These differences would ultimately lead to variable

reactivity with water and ultimately different charging behavior (and consequently variable net surface charge and/or energy values) under similar environmental conditions and/or surface modification states.

As such, an explanation for the presented data (particularly that gathered from surfaces in table 1) is offered based primarily on an ionic based charge transfer mechanism, largely facilitated by surface dependent chemisorption of water.

4.1 Glass surface dynamics under variable relative humidity

First, we consider a three phased system based on the fractional surface coverage model proposed originally by Anderson [61] adapted for an arbitrary alumina-borosilicate glass surface. This model seems particularly appropriate considering the distinct regimes observed in the surface resistivity measurements on Table 1 surfaces (figs. 6a and b). Figure 11a shows a simple illustration of the surface under low relative humidity (i.e. fractional water coverage – $\rho \sim 0$).

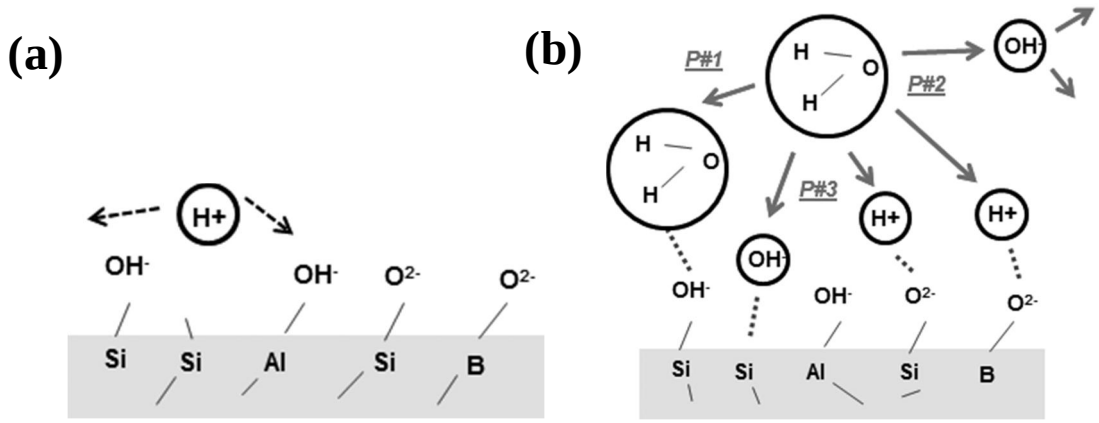

Figure 16: Alumina-borosilicate glass surface at (a) low relative humidity and low fractional water coverage ($\rho \sim 0$) and (b) high humidity and moderate fractional surface coverage ($0 < \rho < 1$).

Under these conditions, ionic conductivity is primarily a result of proton migration to and from available NBO sites that form via dissociation of hydroxylated network formers such as silanol; where the extent to which these processes take place is likely related to glass chemistry. As the relative humidity is increased, molecular water

will increasingly come into contact with the surface (fractional water coverage - $0< \rho <1$). Under these conditions, several types of interactions can occur between close proximity water molecules and the glass surface, where some of which effectively increase the overall surface conductivity more than others. One possibility is that molecular water physisorbs with the OH^- surface via hydrogen bonding (P #1 in fig. 11b), or another stable absorption site such as Ca [58]. The more directly relevant process regarding surface conductivity is the dissociation of water at highly reactive surface sites, such as NBOs and/or under coordinated network formers (P #2, 3 in fig. 11b). Dissociation directly causes increased hydroxylation of the glass surface through donation of a proton to an NBO (i.e. rise in OH^- concentration in the water layer) (P#2) or OH^- passivation of an under-coordinated network former, where the excess proton will bond with the nearest available NBO (P#3). All dissociative processes will effectively increase conductivity via proton facilitated OH^-/H_3O^+ migration in the water layer or by surface based proton hopping. The higher the surface reactivity with close proximity water, the more likely it becomes for water dissociative processes to occur, leading directly to an increase in proton based conductivity. As the relative humidity increases to the point of surface saturation ($\rho \sim 1$), mobile ionic species migrate through a layer of liquid water, causing the surface conductivity to increase uniformly. This regime corresponds to the range of relative humidity >30% in our experiments, where we expect any native surface defect chemistry and/or modification effects to be overshadowed by this more prevalent mechanism. To summarize, it is expected that all glass surfaces will behave similarly at high humidity, regardless of bulk composition or surface treatment. The above interactions are likely, at least in part, to be responsible for EXG surfaces' higher electronegativity/surface energy relative to LXT surfaces as well as its more severe response to modification processes, though without more detailed surface analysis, this hypothesis has yet to be proven.

4.2 Glass surface in contact with metal

When the surfaces shown in figures 11a and 11b are put into contact with a metal surface (in this case the RST metal sphere), there will be a statistical probability that protons in various molecular configurations from the glass surface will transfer to the

metal surface. The proton transfer model we apply here was originally proposed by McCarty *et al*. using similar contact dynamics [29, 43]. Consider the system depicted in figure 12. When the glass and metal surfaces come into close contact, the variably bound protons experience what is effectively a single potential well (pictured above the interfacial region in figure 12), within which protons can move between the two surfaces.

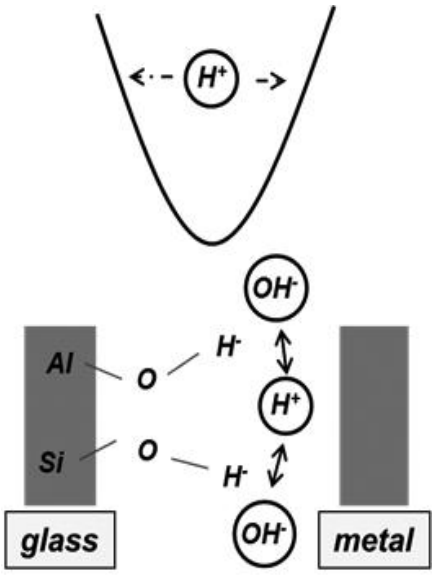

Figure 17: Glass and metal surfaces in Vander Waals type contact. The shape of the potential experienced by protons on the glass surface is shown above the interface.

As these surfaces are pulled apart, the potential well splits into 2 minima where protons will have some statistical probability of existing on one of the two surfaces, depending on the specific bonding state (fig. 13a). At around 2-4nm separation [43, 19], the protons can no longer tunnel and the barrier is too high for thermionic escape (in the absence of external thermal energy) so the protons are trapped on the glass or the metal (fig. 13b).

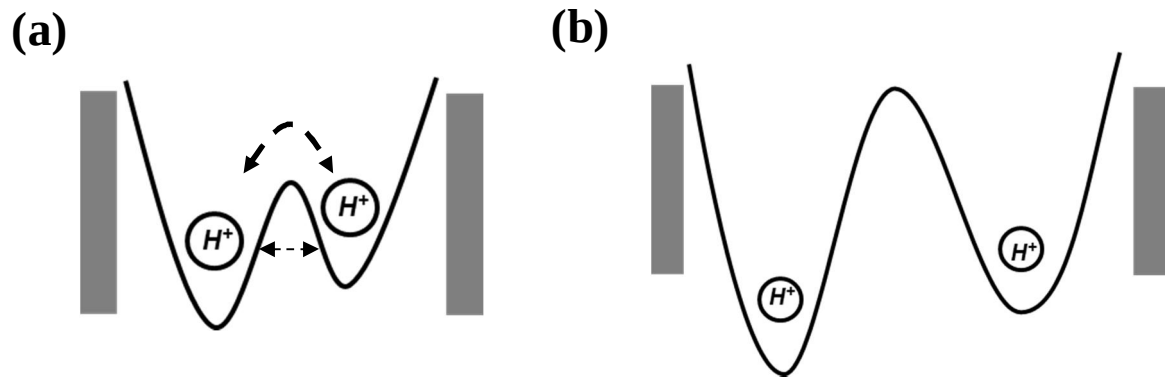

Figure 18: Potential experienced by interfacial protons as surfaces are pulled apart. (a) Initial stages where protons can still transfer to and from metal and glass. (b) Protons trapped on one of the surfaces.

It should logically follow from the previous discussion that as the glass surface becomes more dynamically active via proton migration mechanisms, contact induced charge transfer between surfaces should also increase. With regard to the specific surfaces studied in our experiments, it is believed that the concentration of protons available for transfer is directly impacted by bulk glass chemistry, and subsequent surface defect chemistry. If the glass surface possesses more highly reactive sites to promote water dissociation, then it will inevitably have more protons available for transfer when it comes into contact with a metal surface. As humidity increases, surface-water interaction dynamics will increase and subsequent charge transfer (i.e. charge rate) will increase up to the critical regime above ~30~40% RH where all surfaces' conductivity increases (i.e. decreasing charge rate) due to aqueous surface water saturation. Considering this, it is reasonable to conclude that EXG surfaces have a higher affinity for water chemisorption than do LXT surfaces, causing charge rates to increase more sharply in the <30% RH regime relative to LXT. T#1 has the similar effect of decreasing charge rate on both glass surfaces in the lower humidity regime (though to a more significant extent on EXG) likely due to a decrease in surface reactivity to water through possibly some form of site passivation, though the exact mechanism has not yet been identified. T#2 causes the surfaces of both glass compositions to be more resistant to relative humidity as exhibited by their more stable charge rate in comparison to the untreated glass surfaces. This

particular etching chemistry includes HCL as a component, which is known to preferentially extract mobile cations from the glass surface in exchange for hydronium ions (i.e., leaching) to some finite depth beneath the surface, thereby increasing the effective hydroxyl and/or molecular water content [62]. The increased water content within the glass surface may cause it to become less sensitive to changes in charge behavior as a function of relative humidity.

There are several points that will require clarity in the future for our model to be fully vetted. First off, while the main hypothesis deals strictly with proton transfer stemming from surface interaction with close proximity water in these systems, we cannot rule out other (i.e. electron) transfer mechanisms similar to those proposed by others, especially given recent experimental reports that offer compelling evidence for their existence in metal-Teflon/Lucite polymer contact systems [63]. We actually believe it to be probable that charge transfer in glass-metal contact systems is due to more than one mechanism; though to what extent and how it may depend on surface/bulk chemistry remain unknown. Secondly, the multi-component chemistries of EXG and LXT introduce additional unknown complexities to surface charging phenomena such as: variable (Si, Al, B, etc.) under-coordinated network former reactivity at the surface with moisture; potential for different aliovalent surface impurities to act as redox centers; chemical effects on the extent of reactive site passivation; as well as many others. Because of this, much of our ongoing work focuses on “simpler” calcium-aluminosilicate compositions lying on the tectosilicate (Al2O3/CaO = 1) join (variable SiO2 content along with pure SiO2). Using MD simulations, we hope to explain how variable bulk/surface chemistry (including but not limited to defect concentrations), effect surface charging through a careful comparison of these calculated systems to experimental measurement. By removing several glass elements that are present in EXG and LXT, we hope to further explain the observed behavior in the present study.

5. CONCLUSIONS

We have reported the results of charge rate experiments on controllably modified glass surfaces using a rolling sphere test (RST) along with corresponding zeta potential, surface energy and surface resistivity measurements. The data has shown that surface charge kinetics are variable with respect to surface chemistry, modification process and measurement environment (*i.e.* relative humidity). For C_xH_y polymer coated surfaces, charge rates decrease with increasing film coverage due to O^- containing surface groups being blanketed by non-polar polymer chains. This effect can be reversed by polarizing the top most layers with nitrogen and oxygen containing functional groups via additional plasma processing steps. RST measurements show two distinct charging regimes for EXG and LXT glass surfaces corresponding to low-medium (<30%) and high (>30%) relative humidity. This data correlates well with surface resistivity measurements made on identically prepared samples, though a third observed regime (<10-15% RH) was not explored with RST. The two glasses show similar responses to different treatments, though response magnitude appears to be greater for EXG. A proton transfer model, largely based on surface reactivity with water, has been suggested to explain observed differences in EXG and LXT surface (both modified and non-modified) charging behavior, electronegativity and surface energy. Future work will focus on gathering supporting data for our proposed model through detailed analysis of glass surface chemistry as well as conducting various experiments to assess the extent to which electron transfer plays a role in the charging of glass surfaces.

6. ACKNOWLEDGEMENTS

The authors would like to thank the Corning Display Technologies (CDT) development and fundamental research organizations for funding this work. We would also like to thank Istvan Szabo and Michael Heckman for providing valuable laboratory and/or measurement support.

7. REFERENCES

[1]. J. A. Wiles, B. A. Grzybowski, A. Winkleman, G.M. Whitesides, "A tool for studying contact electrification in systems comprising metals and insulating polymers," *Anal. Chem.,* **75** 4859–4867 (2003).

[2]. L.S. McCarty, G.M. Whitesides," Electrostatic charging due to separation of ions at interfaces: Contact electrification of ionic electrets," *Angew. Chemie - Int. Ed.*, **47** 2188–2207 (2008).

[3]. W.R. Harper, *Contact and Frictional Electrification*, Clarendon Press, Oxford, 1967.

[4]. J. Lowell, A.C. Rose-Innes," Contact electrification," *Adv. Phys.*, **29** 947–1023 (1980).

[5]. D.J. Lacks, R. Mohan Sankaran, "Contact electrification of insulating materials," *J. Phys. D. Appl. Phys.*, **44** 453001 (2011).

[6]. A. Howling, L. Sansonnens, C. Hollenstein, A. Belinger, J. Perrin, "Measurement of substrate charging after plasma processing," Frontiers in Low Temperature Plasma Diagnostics {IV} Proceedings, 2001.

[7]. Electrical Overstress/Electrostatic Discharge Symposium Proceedings, Institute of Electrical and Electronics Engineers, Orlando, Florida, 2009.

[8]. B. Denson, "An electrostatic discharge model for thin-film transistor fabrication," *J. Soc. Inf. Disp.,* **23** 91–96 (2015).

[9]. Hersh, D.J. Montgomery, "Static Electrification of Filaments: Experimental Techniques and Results," *Text. Res. J.*, **25** 279–295 (1955).

[10]. P.E. Shaw, "Experiments on Tribo-Electricity. I. The Tribo-Electric Series," *Proc. R. Soc. London A Math. Phys. Eng. Sci.,* **94** 16–33 (1917).

[11]. A. Wåhlin, G. Bäckström, "Sliding electrification of Teflon by metals," *J. Appl. Phys.* **45** 2058–2064 (1974).

[12]. D.K. Davies, "The examination of the electrical properties of insulators by surface charge measurement," *J. Sci. Instrum.* **44** 521–524 (1967).

[13]. D.K. Davies, "Charge generation on dielectric surfaces," *J. Phys. D,* **2** 1533-1537 (1969).

[14]. I.I. Inculet, “Symposium on Friction and Static Electricity in Solid/Fluid and Solid/Solid Systems: Influence of electric fields on friction electrification between metals and borosilicate glass,” *J. Colloid Interface Sci.,* **32** 395–400 (1970).

[15]. F. Nordhage, “Short Communication Oscillating probe for charge density measurements,” *J. Electrostat.,* **2** 91–95 (1976).

[16]. R.G.C. Arridge, “The static electrification of nylon 66,” *Br. J. Appl. Phys.*, **18** 1311–1316 (1967).

[17]. J. Lowell, “The electrification of polymers by metals,” *J. Phys. D. Appl. Phys.*, **9** 1571 (1976).

[18]. T.J. Fabish, H.M. Saltsburg, M.L. Hair, “Charge transfer in metal/atactic polystyrene contacts,” *J. Appl. Phys.* **47** 930–939 (1976).

[19]. J. Lowell, “Tunnelling between metals and insulators and its role in contact electrification,” *J. Phys. D. Appl. Phys.,* **12** 1541 (1979).

[20]. C.F. Gallo, S.K. Ahuja,” Electrification by Contact Charge Exchange: A Literature Survey of Microscopic Models,” *IEEE Trans. Ind. Appl.*, IA-13 (1977).

[21]. W.R. Harper, “The Volta Effect as a Cause of Static Electrification,” *Proc. R. Soc. London A Math. Phys. Eng. Sci.,* **205** 83–103 (1951).

[22]. H. Rickert, *Contact and frictional electrification*, Von W. R. Harper. Aus der Reihe: Monographs on the physics and chemistry of materials, Oxford at the Clarendon Press (Oxford Univ. Press), London, 1967.

[23]. R.F. Feldman, P.J. Sereda, “Sorption of water on compacts of bottle-hydrated cement. II. Thermodynamic considerations and theory of volume change,” *J. Appl. Chem.,* **14** 93–104 (1964).

[24]. J.A. Medley, “Fractional Electrification of Polar Polymers,” *Nature*, **171** 1077 (1953).

[25]. F.R. Ruckdeschel, L.P. Hunter, “Contact electrification between insulators: Phenomenological aspects,” *J. Appl. Phys.* **46** 4416 (1975).

[26]. E.S. Robins, J. Lowell, A.C. Rose-Innes, "The role of surface ions in the contact electrification of insulators," *J. Electrostat.*, **8** 153-160 (1980).

[27]. A.F. Diaz, D.F. Alexander, "An Ion Transfer Model for Contact Charging," *Langmuir* **9** 1009-1015 (1993).

[28]. L.-H. Lee, "Dual mechanism for metal-polymer contact electrification," *J. Electrostat.*, **32** 1–29 (1994).

[29]. L.S. McCarty, G.M. Whitesides, "Electrostatic charging due to separation of ions at interfaces: Contact electrification of ionic electrets," *Angew. Chemie - Int. Ed.*, **47** 2188–2207 (2008).

[30]. A.F. Labadz, J. Lowell, "Charge transfer across metal-silica interfaces," *J. Appl. Phys. D*, **24** 1416-1421 (1991).

[31]. J. Lowell, "Contact electrification of silica and soda glass," *J. Phys. D. Appl. Phys.*, **23** 1082 (1990).

[32]. J. Lowell, "Mechanisms of contact charging and charge accumulation: experiments on soda glass," *J. Phys. D. Appl. Phys.*, **24** 375 (1991).

[33]. S.H. Behrens, D.G. Grier, "The charge of glass and silica surfaces," *J. Chem. Phys.*, **6716** (2001).

[34]. M. Shimbo, "Surface Charge Studies on Lead Borosilicate Glass Containing Trace Sodium," *J. Electrochem. Soc.*, **134** 156 (1987).

[35]. M. Shimbo, K. Furukawa, K. Tanzawa, T. Higuchi, "Surface-Charge Properties of Fluorine-Doped Lead Borosilicate Glass," *IEEE Trans. Electron Devices.*, **35** 124–128 (1988).

[36]. S.W.A. Szarska, "Surface charge induced on ion exchange glasses," *Ceramics: Polish Ceramic Bulletin*, **49** (1996).

[37]. I.I. Inculet, W.D. Greason, "Effect of electric fields and temperature on electrification of metals in contact with glass and quartz," pp. 23-32, Static Electrification: Proceedings of IOP conference series #11, 1971.

[38]. H. Morita, T. Yokosuka, a. Hatanaka, R. Takeuchi, Y. Dan, M. Doi, "Electrostatic potential distribution characteristics of glass surfaces in vacuums," *23rd Int. Symp. Discharges Electr. Insul. Vac.*, **1** 4–7 (2008).

[39]. J. A. Wiles, M. Fialkowski, M.R. Radowski, G.M. Whitesides, B. A. Grzybowski, "Effects of Surface Modification and Moisture on the Rates of Charge Transfer between Metals and Organic Materials," *J. Phys. Chem. B.*, **108** 20296–20302 (2004).

[40]. B. A. Grzybowski, M. Fialkowski, J. A. Wiles, "Kinetics of contact electrification between metals and polymers," *J. Phys. Chem. B.*, **109** 20511–20515 (2005).

[41]. S.W. Thomas, S.J. Vella, G.K. Kaufman, G.M. Whitesides, "Patterns of electrostatic charge and discharge in contact electrification," *Angew. Chemie - Int. Ed.*, **47** 6654–6656 (2008).

[42]. R.A. Bellman, K. Adib, P. Mazumder, R. Manley, K.L. Simonton, "RIE Mode Fluorine Free ALoT for Willow on Carrier," Restricted Technical Report (RTR) #115067, Corning Incorporated, Corning, NY, 2013.

[43]. L.S. McCarty, A. Winkleman, G.M. Whitesides, "Ionic electrets: Electrostatic charging of surfaces by transferring mobile ions upon contact," *J. Am. Chem. Soc.*, **129** 4075–4088 (2007).

[44]. R.A. Bellman, K. Adib, P. Mazumder, R. Manley, K.L. Simonton, "ICP Mode Fluorine Free ALoT for Willow on Carrier," Restricted Technical Report (RTR) #115066, Corning Incorporated, Corning, NY, 2013.

[45]. S. Wu, "Calculation of interfacial tension in polymer systems," *J. Polym. Sci. Part C Polym. Symp.*, **34** 19–30 (1971).

[46]. C. Dupont-Gillain, B. Nysten, V. Hlady, P. Rouxhet, "Atomic Force Microscopy and Wettability Study of Oxidized Patterns at the Surface of Polystyrene," *J. Colloid Interface Sci.*, **220** 163–169 (1999).

[47]. T. Murakami, S. Kuroda, Z. Osawa, "Dynamics of Polymeric Solid Surfaces Treated with Oxygen Plasma: Effect of Aging Media after Plasma Treatment," *J. Colloid Interface Sci.*, **202** 37–44 (1998).

[48]. J. Du, A.N. Cormack, "Molecular dynamics simulation of the structure and hydroxylation of silica glass surfaces," *J. Am. Ceram. Soc.*, **88** 2532–2539 (2005).

[49]. G.K. Lockwood, S.H. Garofalini, “Bridging oxygen as a site for proton adsorption on the vitreous silica surface,” *J. Chem. Phys.* **131**, (2009).

[50]. G.K. Lockwood, S.H. Garofalini, “Proton Dynamics at the Water − Silica Interface via Dissociative Molecular Dynamics,” *J. Chem. Phys. C*, **118** 29750-29759 (2014).

[51]. E. A. Leed, J.O. Sofo, C.G. Pantano, “Electronic structure calculations of physisorption and chemisorption on oxide glass surfaces,” *Phys. Rev. B - Condens. Matter Mater. Phys.*, **72** 1–11 (2005).

[52]. Y. Ma, A. S. Foster, R.M. Nieminen, “Reactions and clustering of water with silica surface,” *J. Chem. Phys.*, **122**, (2005).

[53]. M. Wilson, T.R. Walsh, “Hydrolysis of the amorphous silica surface. I. Structure and dynamics of the dry surface,” *J. Chem. Phys.*, **113** 9180–9190 (2000).

[54]. T.R. Walsh, M. Wilson, A.P. Sutton, “Hydrolysis of the amorphous silica surface. II. Calculation of activation barriers and mechanisms,” *J. Chem. Phys.*, **113** 9191–9201 (2000).

[55]. E. A. Leed, C.G. Pantano, “Computer modeling of water adsorption on silica and silicate glass fracture surfaces,” *J. Non. Cryst. Solids.*, **325** 48–60 (2003).

[56]. A. Abbas, J.-M. Delaye, D. Ghaleb, G. Calas, “Molecular dynamics study of the structure and dynamic behavior at the surface of a silicate glass,” *J. Non. Cryst. Solids.*, **315** 187–196 (2003).

[57]. A. Tilocca, A.N. Cormack, “Modeling the water-bioglass interface by ab initio molecular dynamics simulations,” *ACS Appl. Mater. Interfaces.*, **1** 1324–1333 (2009).

[58]. A. Tilocca, A.N. Cormack, “The initial stages of bioglass dissolution: a Car-Parrinello molecular-dynamics study of the glass-water interface,” *Proc. R. Soc. A*, (2011).

[59]. A. Tilocca, A.N. Cormack, “Exploring the Surface of Bioactive Glasses : Water Adsorption and Reactivity,” *J. Chem. Phys. C*, **112** 11936–11945 (2008).

[60]. P. Ganster, M. Benoit, J.M. Delaye, W. Kob, “Surface of a calcium aluminosilicate glass by classical and ab initio molecular dynamics simulations,” *Surf. Sci.*, **602** 114–125 (2008).

[61]. J.H. Anderson, G.A. Parks, “The Electrical conductivity of Silica Gel in the Presence of Absorbed Water,” *J. Chem. Phys.*, **72** [10] 1968.

[62]. R.H. Do Remus, Y. Mehrotra, W. a. Lanford, C. Burman, “Reaction of water with glass: influence of a transformed surface layer,” *J. Mater. Sci.*, **18** 612–622 (1983).

[63]. C.Y. Liu, A.J. Bard, “Electrons on dielectrics and contact electrification,” *Chem. Phys. Lett.*, **480** 145–156 (2009).

CHAPTER III: TABLE OF CONTENTS

LIST OF FIGURES

LIST OF TABLES

COORDINATION STATE AND DEFECT EVOLUTION IN SiO_2 STRUCTURES FORMED USING MOLECULAR DYNAMICS (MD) UNDER VARIABLE COOLING CONDITIONS

Gabriel Agnello[a,b6], and Alastair N. Cormack[b]

c. Science and Technology Division, Corning Incorporated, Corning, NY 14831, USA
d. New York State College of Ceramics at Alfred University, Alfred, NY 14802, USA

ABSTRACT

Under ideal circumstances, the structures formed in MD simulations of relatively simple glassy systems, such as stoichiometric amorphous SiO2, should be fully coordinated and free of intrinsic type defects (NBO, O_{3C}, Si_{3C}, etc). This has been shown to not always be the case for a variety of reasons, one of which being the use of non-optimized cooling rates/conditions. In order for MD simulations to accurately portray reality, critical effects due to variable cooling cycle parameters must be well understood. This is especially true if the bulk structures' ultimate intended use is for surface generation and subsequent structural analysis and/or reactionary dynamics interaction with the surrounding environment. Here, we report the results of MD simulations using modified Teter interatomic potentials on amorphous SiO_2 glass systems under variable cooling cycles/conditions. Analysis of Si and O coordination states as functions of temperature and cooling condition show a strong non-linear dependence, suggesting that defect (NBO, O_{3C}, Si_{3C}, etc.) concentrations do not necessarily decrease with longer trajectory times. Analyses of defect clusters found in the structures at low temperatures (<1200K) show variable levels of dynamic activity, highlighted by the formation and subsequent annihilation of certain defect pairs (i.e. O_{C3} – Si_{C3} and NBO-Si_{C5}). The results suggest that the types of reactions as well as the extent to which they occur are heavily dependent on thermal history/cooling rate.

[6] Contact: agnellogp@corning.com

1. INTRODUCTION

MD simulations have been commonly used to study atomic scale interactions in solids for decades, due to the vast array of structural and chemical information to be gained that can be otherwise difficult to obtain experimentally. An area of current extensive study is the molecular interaction of atmospheric water with glass surfaces, both in SiO_2 [1-3] as well as more complicated multi-component systems [4-8]. A key conclusion from this body of work is that the extent to which close proximity water molecules physisorb (molecular absorption) or chemisorb (water dissociation and corresponding surface hydroxylation) is critically dependent on defects at the surface, such as non-bridging oxygen and/or under-coordinated network formers. Recent experimental work has suggested that contact-induced glass surface charging behavior is closely related to these reactions and the resultant increase in proton based conduction mechanisms [9]. One of the most appropriate ways to test this hypothesis is through a careful comparison between MD simulations and experimental electrical measurement(s) of targeted glass surface composition(s). In order for any comparison to be valid, it is crucial that the simulated surfaces to be as close to "real" as possible; this is directly tied to the quality of the initial bulk structures.

Many reports exist in the literature that focus on Si and O coordination state in bulk SiO_2, some experimental and some theoretical via MD simulation. X-ray Diffraction (XRD) data reported by Mozzi and Warren [10] suggested 100% 4-fold and 2-fold coordination for Si and O atoms respectively in vitreous silica, as expected. Studies using X-ray and neutron diffraction methods have reported similar results [11-14], where Si and O are all fully coordinated and incorporated into a three dimensional network comprised of SiO_4^{+4} structural units. Historically, MD simulations have not always shown this type of perfect structure/topology . Horbach and Kob [15] used BKS potentials on an 8016 atom SiO_2 system and found only >99% full coordination at the still relatively high temperature of 2750K. Using BKS potentials, Vollmayr-Lee and Zippelius [16] observed 99.9% fully coordinated Si and O at 2500K, though notably in a much smaller system (338 atoms). Conversely, Hoang [17] used 3 term Morse potentials and observed as many as 2.7% of Si atoms in a 3000 ion system to be under-coordinated (i.e. only surrounded by three O atoms) at temperatures as low as 700K. Others [18,19]

have reported relative defect concentrations as high as 24.7% in simulated bulk silica, indicating that a fully coordinated system is not a forgone conclusion. Cooling rate/thermal history has been shown to have a significant impact on the generated structure in MD, and as such it is critical for us to understand the associated effects. Microscopic properties of simulated glasses, including but not limited to coordination state(s), have been shown to be dependent (on the order of a few percent) on the cooling rates with which the glass was formed [20]. Vollmayr et. al. showed via radial distribution analysis of an arbitrary binary mix of particles, A and B, that the local order of the system became more pronounced as the cooling rate was decreased [20]. This conclusion was reached by observing a ~2% increase in nearest neighbor peak height at the lowest studied rate. Later, the authors extended the work in [20] to a SiO_2 system using BKS potentials [21] where they observed 4.5% (5% to 0.5%) and 2.5% (3% to 0.5%) decreases in non-four and non-two coordinated Si and O, respectively at 0K as the cooling rate was reduced from approximately 10^{15} to 10^{12} K/s[7]. Min Lee et. al. [19] reported an even more significant 7.6% decrease in combined relative defect concentration (24.7% to 17.1%) across a lower range of simulated cooling rates (10^{13}-10^{11} K/s). Similar results were reported for smaller 100-200 atom systems where those quenched at a rates of ~10^{12} K/s were void of any coordination defects as opposed to those quenched at higher rates (~10^{14}) that contained variable amounts of under or over-coordinated Si and/or O atoms [22-25].

In the present article, we report on new efforts to minimize coordination defects in SiO_2 systems formed via MD simulation by varying the cooling rate/trajectory time (i.e. simulation thermal history). To the authors' knowledge, the range of rates explored ~$5x10^{10}$ – $2x10^{9}$ K/s in the current study represents the lowest of its type reported. The results suggest that coordination defect concentrations do not necessarily continue to decrease with longer equilibration times. We will also present data showing that system

[7] Results from ref [21] and [16] are from the same authors, using the same potentials on the same material system and appear upon first glance to be contradictory. Potential reasons for the discrepancy include: the use of different Si-O cutoff radii used in the two references: Ref [16] (2.4Å) vs. Ref [21] (2.2Å); different referenced temperatures for coordination state: Ref [16] (2500K) vs. Ref [21] (0K); and significantly different system sizes: Ref [16] (338 atoms) vs. Ref [21] (1002 atoms).[11] "Defect cluster" is defined as the atoms surrounding a coordination defect, such as a non-bridging oxygen, contained within a specified radius. Cluster radius for analysis presented in this work is ~4.5Å-6Å.

dynamics (i.e. bond length stability, defect formation/evolution) at temperatures well below T_F (<1200K) are highly dependent on the cooling rate used to form the glass.

2. CALCULATION APPROACH

2.1 Simulation Details

All SiO_2 structures were generated with the GROMACS [26,27] molecular dynamics simulation package using a Macpro Quad core Intel Xeon workstation (total of 24 nodes; 12 per trajectory) where total computing time ranged from ~73 to 1820 CPU hours depending on the cooling rate being used. Simulations were run under NPT conditions, where temperature and pressure were controlled through directly implemented Berendsen thermo/barostats, respectively. Periodic boundary conditions were used to avoid any related finite system size effects and Coulomb interactions were accounted for via Ewald summation with a cutoff value of 10Å. An analytical form for the Buckingham [28] potential was used to calculate the interatomic forces between atoms i and j (equation 1).

$$\boldsymbol{\Phi_{ij}(r) = A_{ij} e^{-\left(\frac{r}{\rho_{ij}}\right)} - \frac{C_{ij}}{r^6} + \frac{q_i q_j}{4\pi\varepsilon_0 r}} \qquad \textbf{(1)}$$

The first two terms represent short range attractive and repulsive forces and the third term accounts for long range Coulombic (electric) potential interaction. The potential parameters used in this work were developed by Teter [29], with a modification to the O-O pair terms (q_e=0.6*e*) by Cormack and Du [30] (Table 2). The Si-Si pair short range interactions were neglected.

Table 4: Interatomic Potential Parameters

Interaction (ij)	A_{ij} (eV)	P_{ij} (Å)	C_{ij} (eV/Å^6)
Si-O	13702.905	0.193817	54.681
O-O	2029.2195	0.343645	192.58

2.2 Structure Generation

~88nm^3 boxes were generated with 6000 randomly positioned, stoichiometric Si (N=2000) and O (N=4000) atoms and allowed to equilibrate at 3000K for a total of 67ps (320,000 time steps at 2fs/step) to simulate a melted glass. At 300K, the box volume reduces slightly to ~86nm^3 corresponding to a density of ~2.3g/cm^3 which is close to the commonly published value of ~2.20 g/cm^3 [31,32]. Structure densities are approximately equal regardless of thermal history. The systems were then cooled to room temperature (300K) in increments of 20K at different rates, which are detailed in Table 1. At the conclusion of each 20K temperature step (400ps, 2000ps or 10000ps depending on cooling cycle) in 100K increments (2500K, 2400K, 2300K…..300K) the final frame of the structure was analyzed for Si and O coordination states. A fixed value of R_{Si-O}=2.1Å was chosen for bonding cutoff radius corresponding to the approximate position of the minima following the nearest neighbor peak in $g_{ij}(r)$. Several defect clusters[11] were examined more closely at specific temperatures to better understand the relationship between different types of defect formation/evolution and thermal cycle. Radial Distribution Functions, RDF - $g_{ij}(r)$, were also calculated at three temperatures along the cooling curves to assess system order as a function of rate.

Table 5: Thermal Cycle Parameters. Cooling Cycles 1-3 Will Often be Referred to as Fast, Medium and Slow, Respectively

Cooling cycle	Time step (ps)	# of steps	Total cooling time (ps)	Cooling rate (K/ps)	Cooling rate (K/s)
1	0.002	200000	54000	0.05	5E10^{10}
2	0.002	1000000	270000	0.01	1E10^{10}
3	0.002	5000000	1350000	0.002	2E10^{9}

[11] "Defect cluster" is defined as the atoms surrounding a coordination defect, such as a non-bridging oxygen, contained within a specified radius. Cluster radius for analysis presented in this work is ~4.5Å-6Å.

3. RESULTS AND DISCUSSION

3.1 Radial distribution function – $g_{ij}(r)$

Radial distribution functions (RDF - $g_{ij}(r)$) were calculated by integrating relative distances over 100 separate frames within an individual 20K trajectory. Figures 1a-c show partial Si-O pair RDFs for each cooling rate at 2480K, 1500K and 300K, respectively. The data show little or no difference between peak heights and/or positions as cooling rate is varied. The stability of first and second order peak positions suggests that the relative size of the tetrahedral structural units is generally, as expected, independent of thermal history [19]. The increase in nearest neighbor peak height and corresponding decrease in peak width are consistent with the system becoming more ordered as temperature decreases. First and second peak position values of approximately 1.61Å and 4.12Å, respectively, correlate well with published experimental [10,33] as well as other theoretical[19,21,34] data; however we do not observe peak height increases with decreasing cooling rates as mentioned in other reports [19-21]. This is probably because the effect that a reduction in cooling rate has on local order in these systems is not linear, where systems cooled at rates in the 10^{11}-10^{13} range exhibit significant differences while our systems cooled with thermal cycles several orders of magnitude slower do not.

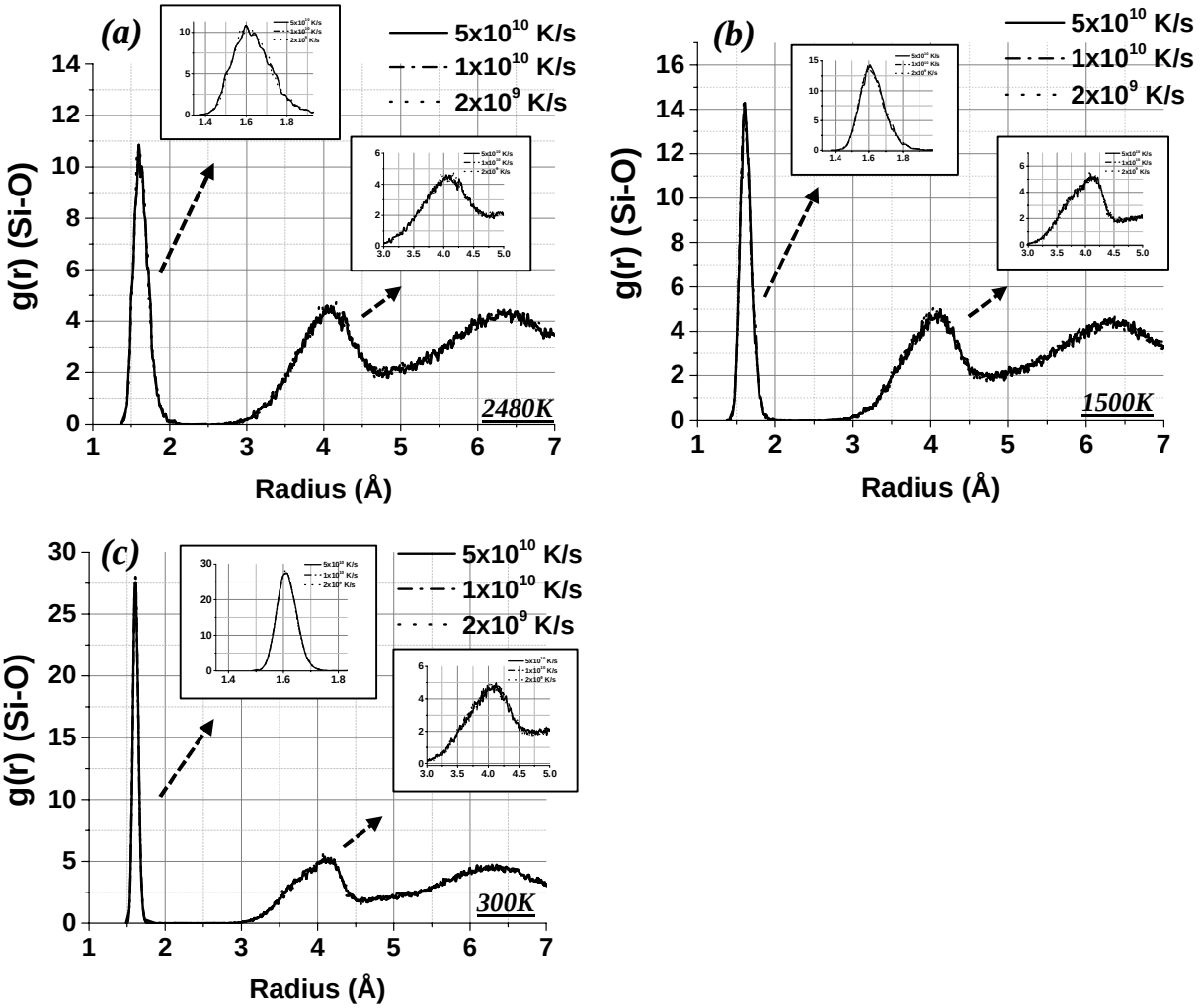

Figure 19: $g_{Si\text{-}O}(r)$ for variable cooling rate at (a) 2480K (b) 1500K and (c) 300K.

3.2 Coordination states

Figures 2a-b show concentration/number of bridging O (BO) and fully coordinated Si (Si_{C4}), respectively, as functions of temperature for each cooling rate. Transition temperatures, as estimated by observing the leveling off of defect concentrations, are somewhat higher (~1750K) than those generally observed in experiments. These differences are often times attributed to the more rapid cooling processes utilized in MD simulations, however the validity of such assertions are actively debated. Interestingly, the $1x10^{10}$ K/s rate resulted in the structure nearest to full coordination (≥99.95%) having only one non-bridging oxygen (NBO) and one under-coordinated silicon (Si_{C3}) at 300K.These defects were stable at temperatures

below the transition temperature. The $5x10^{10}$ K/s and $2x10^{9}$ K/s rates resulted in higher defect concentrations as well as more dynamic defect states at temperatures below the transition temperature, as indicated by the continuous fluctuation in BO and/or Si_{C4} concentrations.

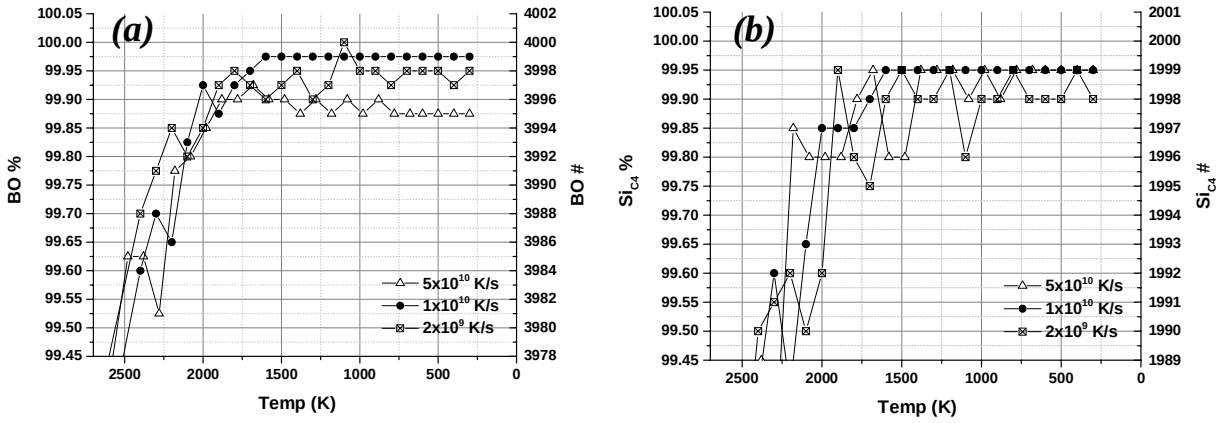

Figure 20: Concentrations/numbers of (a) BO and (b) Si_{4c} as functions of temperature for each cooling cycle.

^{10} K/s and $2x10^{9}$ K/s cooled structures included NBO and Si_{C3} as well as over-coordinated oxygen (O_{C3}) and/or silicon (Si_{C5}). The types, and their concentration, of defects that formed in these structures were highly dependent on cooling rate; this can be visualized using the surface with XY projection plots presented in figures 3a-d. Data shown in figures 3a-d are restricted to temperatures from 2000K to 300K, so as to allow a higher color scale fidelity. The results show several notable differences in defect concentrations that suggest strong dependence on cooling cycle. Tri-clustered oxygen formation increased in both the $5x10^{10}$ K/s and $2x10^{9}$ K/s cooled structures relative to the $1x10^{10}$ K/s cooled glass, where no O_{C3} was observed at temperatures below T_F (Fig. 3a). NBO concentration, on the other hand, followed the changes in cooling rate, where fewer NBO formed during the slow rate and more was observed during the fast rate (Fig. 3b).

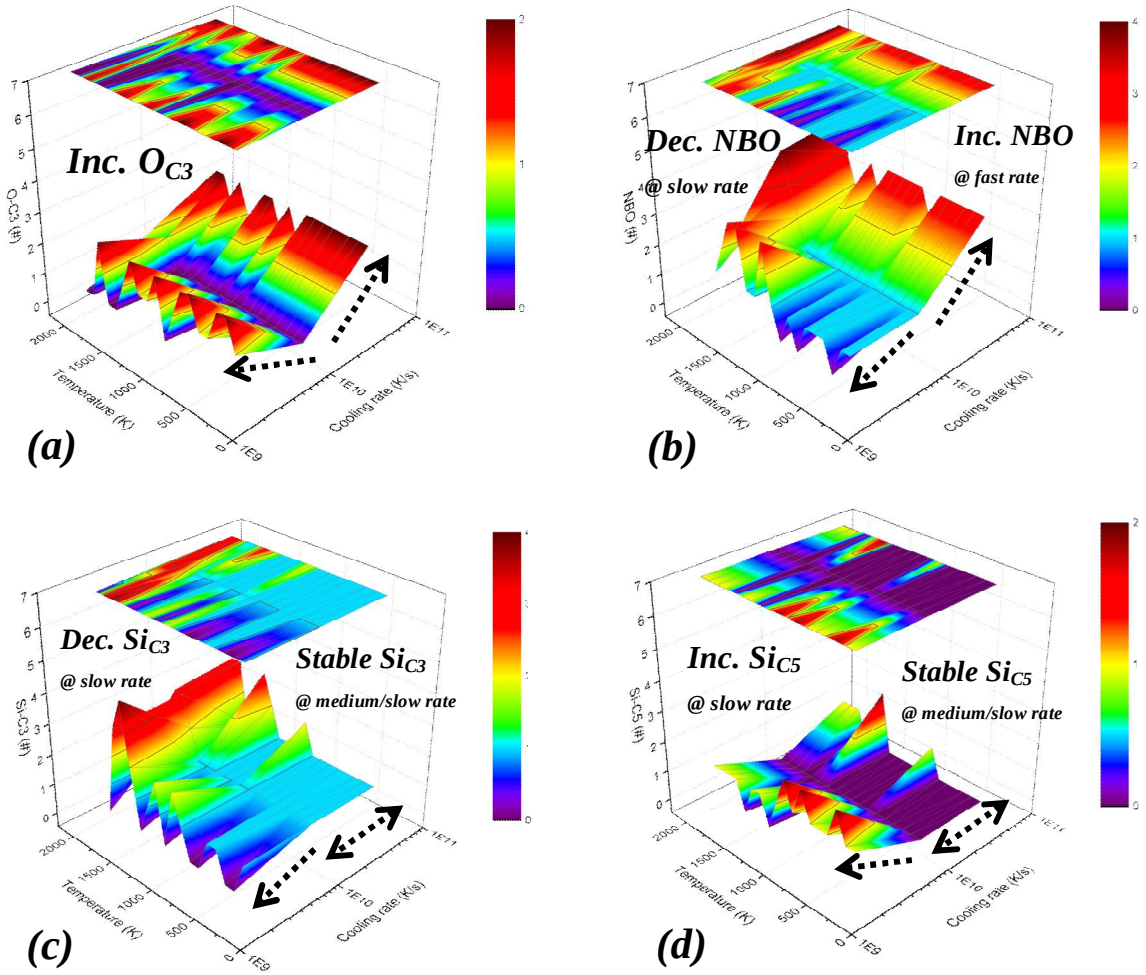

Figure 21: Surface, with XY projection, plots depicting structural defect concentrations as functions of temperature (~2000-300K). (a) O_{C3} (b) NBO (c) Si_{C3} (d) Si_{C5}.

A main goal of the present study was to eliminate the small amount of under-coordinated Si formation that occurred during the two fastest cooling rates. Slowing the rate down to $2x10^9$ K/s apparently had a beneficial impact on Si_{C3} concentration (Fig. 3c); however, it appears to come at the cost of increased over-coordinated Si (Si_{C5}) relative to the medium and fast rate structures (Fig. 3d).

In general, the data suggest that increasing the cooling rate from $2x10^9$ K/s to $5x10^{10}$K/s effectively altered the preferred defect configuration in the structures from Si_{C5} to NBO. O_{C3} formation experienced a minimum at $2x10^{10}$ K/s, which was a rather unexpected result.

3.3 Defect evolution

The apparent correlation between NBO, O_{C3}, Si_{C5} and Si_{C5} concentrations suggests that dynamic behavior involving the related creation and/or annihilation of these defects may be of some critical importance. These types of structural reconfigurations in SiO_2 glasses have been reported previously [16], though at temperatures greater than 2500K. To assess defect evolution, we used Crystal Maker® (version 9.4.1) to visualize defect clusters at targeted points along each cooling cycle, where each cluster contained all atoms within a 4.5Å radius from the defect. Each structure shown in this section represents a system "snapshot" taken at the conclusion of one 20K increment of a specific cooling cycle. While these data do not provide insight into fs scale system dynamics, it does show the overall motion of the atoms at temperatures well below the transition region, where one would expect the system to be "frozen", where the term "frozen" encompasses any long range motion not related to low temperature thermal vibration (i.e. phonon generation) which takes place in any/all solid(s).

3.3.1 Tri-clustered oxygen (O_{C3}) and under-coordinated silicon (Si_{C3})

Figure 4a shows a 2D representation of O_{C3} concentration, corresponding to the data shown in figure 3a. O_{C3} defects that formed during the slow (Fig. 4b-d) and fast (Fig. 4e-g) cooling cycles were examined at temperatures of 1200K, 1100K and 1000K, as indicated by the dashed box in Fig. 4a. At 1200K (Fig. 4b), an O_{C3} connects three SiO_4 tetrahedral units at their corners. The three silicon atoms bonded to the O_{C3} are labeled Si(1), Si(2) and Si(3), accordingly. After the 1100K trajectory, the Si(3)-O pair had moved apart sufficiently for the two to no longer be bonded, effectively destroying the O_{C3} defect center and creating a Si_{C3} defect (Fig 4c). As the system's temperature was further reduced to 1000K (Fig. 4d), the original O_{C3} configuration was re-established with all Si-O pair distances falling back within the 2.1Å cutoff. The same relationship between Si_{C3} and O_{C3} defects was observed during the fast cooling rate (Fig 4e-g). Table 3 lists Si-O pair distances as shown in figure 4 for all three temperatures. For comparison, Si-O(1,2,3) pair distances were calculated for the single Si_{C3} defect found in the $1x10^{10}$ K/s cooled structure at 1200K,1100K and 1000K.

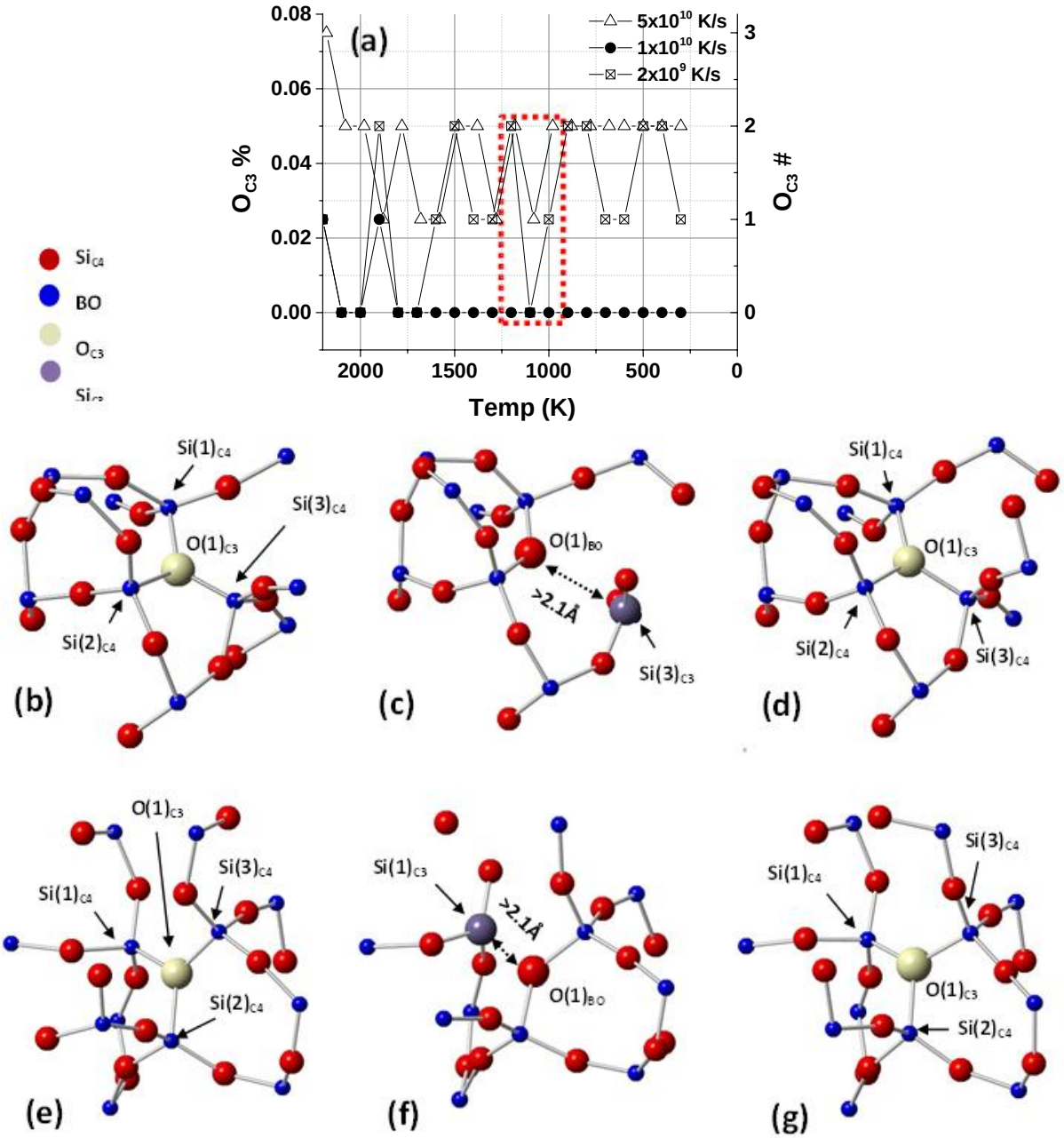

Figure 22: (a) 2D representation of O_{C3} defect concentration as a function of cooling temperature for each cooling rate. Defect cluster visualization for O_{C3}: (b) Cooling cycle 3 – 1200K (c) Cooling cycle 3 – 1100K (d) Cooling cycle 3 – 1000K (e) Cooling cycle 1 – 1180K (f) Cooling cycle 1 – 1080K (g) Cooling cycle 1 – 980K.

The data in table 3 suggests that the structure cooled at $1x10^{10}$ K/s was less dynamically active at these temperatures relative to the structures cooled at faster and/or slower

rates. Reality may be less straightforward, as this set of analyses was not sensitive to fs time scale dynamics. Nonetheless, the fact that the defect state of the $1x10^{10}$ K/s cooled structure remained unchanged after each examined 20K/2ns trajectory lends itself nicely to this hypothesis.

Table 6: O-Si (Si-O for Cooling Rate 2) Pair Distances (Figures 4b-g) Across Several Temperatures for Each Cooling Rate. The Analysis for the $5x10^{10}$ K/S Cooled Structure was Actually Done at 1180K, 1080K And 980K as Opposed to 1200K, 1100K And 1000K, However the Comparison Should Still be Valid.

Cooling cycle	Pair	1200K (Å)	1100K (Å)	1000K (Å)	Deviation (+/- Å)
$5x10^{10}$ K/s (Fig. 4e-g)	O-Si(1)	1.69	2.27	1.66	0.34
	O-Si(2)	1.78	1.73	1.83	0.05
	O-Si(3)	1.66	1.71	1.76	0.05
$1x10^{10}$ K/s	Si-O(1)	1.46	1.51	1.54	0.04
	Si-O(2)	1.48	1.54	1.57	0.05
	Si-O(3)	1.62	1.48	1.49	0.08
$2x10^{9}$ K/s (Fig. 4b-d)	O-Si(1)	1.69	1.68	1.78	0.06
	O-Si(2)	2.00	1.58	1.73	0.21
	O-Si(3)	1.58	2.9	1.79	0.71

3.3.2 Non-bridging oxygen (NBO) and over-coordinated silicon (Si_{C5})

Figure 5a shows a 2D representation of NBO concentration as a function of temperature for each cooling rate. This data corresponds to that presented in figure 3b. The approach used to visualize O_{C3} defect centers in section 3.3.1 was repeated here for NBO in structures cooled via fast and slow rates at temperatures of 1000K, 900K and 800K. The points at which the structures were analyzed are again highlighted by a dashed box in Fig. 5a. The NBO-Si_{C5} specific processes in the slowly cooled structure appear to be more complicated (at least in this particular case) than those observed for O_{C3} (Fig 4b-d), where the tri-clustered oxygen defect disappeared at 1100K and then reappeared at a lower temperature centered on the *same* atom. In figures 5b-d, NBO migration via formation, and subsequent annihilation, of an intermediary Si_{C5} was observed. At 1000K, O(1) was in a non-bonding state and O(2)

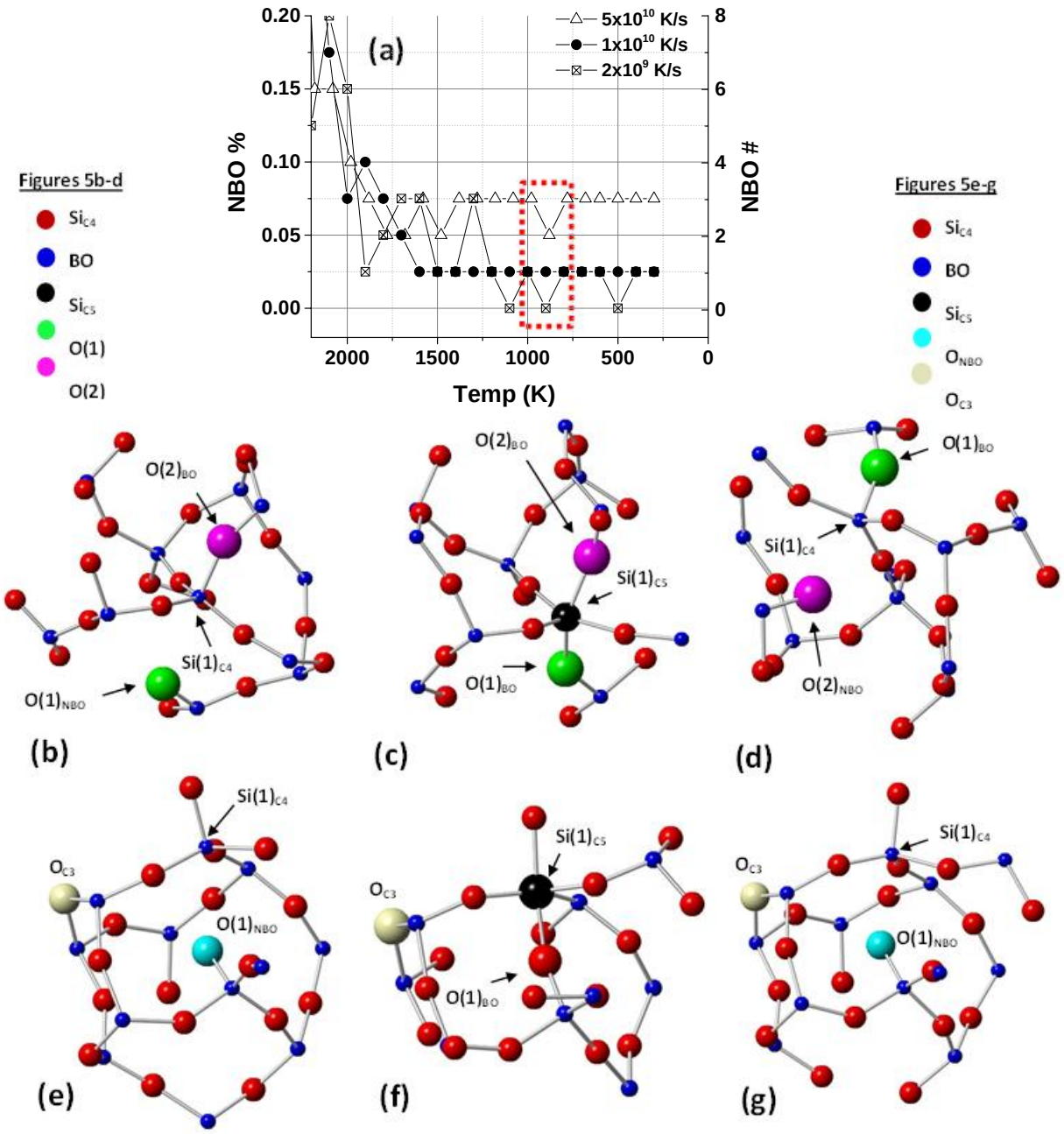

Figure 23: (a) 2D representation of NBO defect concentration as a function of cooling temperature for each cooling rate. Defect cluster visualization for NBO: (b) Cooling cycle 3 – 1000K (c) Cooling cycle 3 – 900K (d) Cooling cycle 3 – 800K (e) Cooling cycle 1 – 980K (f) Cooling cycle 1 – 880K (g) Cooling cycle 1 – 780K.

was in a bridging state with Si(1). The Si(1)-O(1) pair distance was approximately 2.95Å, putting it well over the bonding cutoff radius. At 900K, the Si(1)-O(1) pair distance reduced to ~1.85Å, effectively changing O(1) into BO and Si(1) into Si_{C5}. As the temperature was further reduced to 800K, O(1) remained in a bridging state with Si(1) however the Si(1)-O(2) pair distance now exceeded the cutoff radius (2.42Å); transitioning O(2) into a non-bridging state and reverting Si(1) back into Si_{C4}. Figures 5e-g show NBO-Si_{C5} related process dynamics for the structure cooled at the fast rate similar to those observed in figures 4b-g, where NBO disappears only to reappear at a lower temperature centered on the same atom. Also of note, there is an O_{C3} in the defect cluster (labeled accordingly) that does not take part in the NBO-Si_{5C} exchange process. Table 4 lists Si-O pair distances as shown in figure 5. The Si-O pair distance for the single NBO in the $1x10^{10}$ K/s cooled structure was calculated at the same temperatures for comparative purposes.

Table 7: Si-O Pair Distances (Figures 5b-g) Across Several Temperatures for Each Cooling Rate. As Was the Case in Section 3.3.1 The Analysis for the $5x10^{10}$ K/S Cooled Structure was Actually Done at 1180K, 1080K And 980K as Opposed to 1200K, 1100K and 1000K, However the Comparison Should Still be Valid

Cooling cycle	Pair	1000K (Å)	900K (Å)	800K (Å)	Deviation (+/- Å)
$5x10^{10}$ K/s (Fig. 5e-g)	O(1)-Si(1)	2.83	1.72	2.56	0.58
$1x10^{10}$ K/s	O-Si	1.65	1.53	1.56	0.06
$2x10^{9}$ K/s (Fig. 5b-d)	O(1)-Si(1)	2.95	1.85	1.72	0.68
	O(2)-Si(1)	1.79	1.87	2.42	0.34

The data in table 4 again suggests that the structure cooled at a rate of $1x10^{10}$ K/s was less active than the alternately cooled systems at the examined temperatures. Currently, we do not have an in depth explanation for the seemingly non-linear effects of variable cooling rate on the coordination state and defect evolution in these systems. Nonetheless, it can be reasonably concluded from the data that utilizing a cooling rate of $1x10^{10}$ K/s (within the investigated range) will result in an SiO_2 structure with relatively lower defect concentration(s), while also exhibiting lower levels of dynamic activity at temperatures well below the transition temperature. Future work will focus

on adjustment of additional simulation parameters, including but not limited to alternate interatomic potentials, in an attempt to understand the effects of thermal cycle on low temperature structural defect states.

4. CONCLUSIONS

The effects of variable cooling rate on coordination state and low temperature defect evolution in SiO_2 glass systems have been reported. To the authors' knowledge, the targeted range of $5x10^{10} – 2x10^{9}$ K/s is the lowest of its type reported in the literature. The data shows that cooling rate directly impacts the type(s) and concentration(s) of structural defects (primarily under and over-coordinated Si and O) that form in these systems. We do not observe a continuous decrease in defect formation with the reduction of cooling rate; to the contrary, the data suggests a somewhat more complex relationship between formation and subsequent annihilation of structural defects, where the extent to which these processes occur depends on thermal history. Structures cooled via the $1x10^{10}$ K/s (medium speed) rate resulted in the lowest defect concentration and highest structural stability at low (<1200K) temperatures.

5. ACKNOWLEDGEMENTS

The authors would like to thank the Corning Display Technologies (CDT) development and fundamental research organizations for funding this work.

REFERENCES

[1]. J. Du, A.N. Cormack, "Molecular dynamics simulation of the structure and hydroxylation of silica glass surfaces," *J. Am. Ceram. Soc.*, **88** 2532–2539 (2005).

[2]. G.K. Lockwood, S.H. Garofalini, "Bridging oxygen as a site for proton adsorption on the vitreous silica surface," *J. Chem. Phys.*, **131,** (2009).

[3]. G.K. Lockwood, S.H. Garofalini, "Proton Dynamics at the Water − Silica Interface via Dissociative Molecular Dynamics," *J. Chem. Phys. C*, **118** 29750-29759 (2014).

[4]. A. Abbas, J.-M. Delaye, D. Ghaleb, G. Calas, "Molecular dynamics study of the structure and dynamic behavior at the surface of a silicate glass," *J. Non. Cryst. Solids.*, **315** 187–196 (2003).

[5]. A. Tilocca, A.N. Cormack, "Modeling the water-bioglass interface by ab initio molecular dynamics simulations," *ACS Appl. Mater. Interfaces.*, **1** 1324–1333 (2009).

[6]. A. Tilocca, A.N. Cormack, "The initial stages of bioglass dissolution: a Car-Parrinello molecular-dynamics study of the glass-water interface," *Proc. R. Soc. A*, (2011).

[7]. A. Tilocca, A.N. Cormack, "Exploring the Surface of Bioactive Glasses : Water Adsorption and Reactivity," *J. Chem. Phys. C*, **112** 11936–11945 (2008).

[8]. P. Ganster, M. Benoit, J.M. Delaye, W. Kob, "Surface of a calcium aluminosilicate glass by classical and ab initio molecular dynamics simulations," *Surf. Sci.* **602** 114–125 (2008).

[9]. G. Agnello, J. Hamilton, R. Manley, E. Streltsova, W. LaCourse, A. Cormack, "Investigation of contact-induced charging kinetics on variably modified glass surfaces," *Appl. Surf. Sci.*, **356** 1189–1199 (2015).

[10]. R.L. Mozzi, B.E. Warren, "The structure of vitreous silica," *J. Appl. Crystallogr.*, **2** 164–172 (1969).

[11]. L.I. Tatarinova, "The structure of solid amorphous and liquid substances," From: Moscow, Nauka, 1983:619097 CAN99:219097 CAPLUS, 1983.

[12]. P.A. V Johnson, A.C. Wright, R.N. Sinclair, “Neutron scattering from vitreous silica II. Twin-axis diffraction experiments,” *J. Non. Cryst. Solids.*, **58** 109–130 (1983).

[13]. R.N. Sinclair, A.C. Wright, “Neutron scattering from vitreous silica I. The total cross-section,” *J. Non. Cryst. Solids*, **57** 447–464 (1983).

[14]. A.C. Wright, “Neutron and X-ray amorphography,” *J. Non. Cryst. Solids*, **106** 1–16 (1988).

[15]. J. Horbach, W. Kob, “Static and dynamic properties of a viscous silica melt,” *Phys. Rev. B.*, **60** 3169–3181 (1999).

[16]. K. Vollmayr-Lee, A. Zippelius, “Temperature-dependent defect dynamics in the network glass SiO2,” *Phys. Rev. E.*, **88** 52145 (2013).

[17]. V. V. Hoang, “Static and Dynamic Heterogeneities in Supercooled SiO2,” pp. 77-94, Defect and Diffusion Forum, Vols. 242-244, Sept. 2005.

[18]. B. M. Lee, S. Munetoh, T. Motooka, Y. W. Yun, K. M. Lee, “Molecular-Dynamics Analysis of the Structural Properties of Silica during Cooling,” pp. 101-106, *Solid State Phenomena*, vol. 139, Apr. 2008.

[19]. B.M. Lee, H.K. Baik, B.S. Seong, S. Munetoh, T. Motooka, “Generation of glass SiO2 structures by various cooling rates: A molecular-dynamics study,” *Comput. Mater. Sci.*, **37** 203–208 (2006).

[20]. K. Vollmayr, W. Kob, K. Binder, “How do the properties of a glass depend on the cooling rate? A computer simulation study of a Lennard-Jones system,” *J. Chem. Phys.*, **105** 4714 (1996).

[21]. K. Vollmayr, W. Kob, K. Binder, “Cooling-rate effects in amorphous silica: A computer-simulation study,” *Phys. Rev. B.*, **54** 15808–15827 (1996).

[22]. L. Martin-Samos, Y. Limoge, G. Roma, “Defects in amorphous SiO 2 : Valence alternation pair model,” *Phys. Rev. B.*, **76** 104203 (2007).

[23]. L. Martin-Samos, Ph.D. thesis, Cergy-Pontoise University, France, 2004.

[24]. L. Martin-Samos, Y. Limoge, J.-P. Crocombette, G. Roma, N. Richard, E. Anglada, “Neutral self-defects in a silica model: A first-principles study,” *Phys. Rev. B.*, **71** 14116 (2005).

[25]. L. Martin-Samos, Y. Limoge, N. Richard, J.-P. Crocombette, G. Roma, , E. Anglada, E. Artacho, "Oxygen neutral defects in silica: Origin of the distribution of the formation energies," *Europhys. Lett.*, **66** 680-686 (2004).

[26]. D. Van Der Spoel, E. Lindahl, B. Hess, G. Groenhof, A.E. Mark, H.J.C. Berendsen, "GROMACS: Fast, flexible, and free," *J. Comput. Chem.*, **26** 1701–1718 (2005).

[27]. B. Hess, C. Kutzner, D. Van Der Spoel, E. Lindahl, "GROMACS 4 : Algorithms for Highly Efficient , Load-Balanced , and Scalable Molecular Simulation," *J. Chem. Theory Comput.*, **4** [3] 435-447 (2008).

[28]. R.A. Buckingham, "The Classical Equation of State of Gaseous Helium, Neon and Argon," *Proc. R. Soc. Lond. A. Math. Phys. Sci.*, **168** 264–283 (1938).

[29]. A.J. Lamphere, "A Structural Study Of A Multicomponent E-Cr Glass Via Molecular Dynamics Simulation," M.S. Thesis, Alfred University, Alfred, NY, 2015.

[30]. A.N. Cormack, J. Du, T.R. Zeitler, "Sodium ion migration mechanisms in silicate glasses probed by molecular dynamics simulations," *J. Non. Cryst. Solids.*, **323** 147–154 (2003).

[31]. CRC Handbook of Chemistry and Physics, 92nd ed., p. 4.88, CRC Press, Boca Raton, FL, 2011.

[32]. R. Brückner, "Properties and structure of vitreous silica," *J. Non. Cryst. Solids.* **5** 123–175 (1970).

[33]. D.I. Grimley, A.C. Wright, R.N. Sinclair, "Neutron scattering from vitreous silica IV. Time-of-flight diffraction," *J. Non. Cryst. Solids.*, **119** 49–64 (1990).

[34]. L. Adkins, A. Cormack, "Large-scale simulations of sodium silicate glasses," *J. Non. Cryst. Solids.*, **357** 2538–2541 (2011).

CHAPTER IV: TABLE OF CONTENTS

LIST OF FIGURES

LIST OF TABLES

BULK AND SURFACE STRUCTURE OF SILICA RICH CALCIUM ALUMINOSILICATE (CAS) GLASSES ALONG THE MOLAR $CAO/AL_2O_3 = 1$ JOIN VIA MOLECULAR DYNAMICS (MD) SIMULATION

Gabriel Agnello[a,b12], Randy Youngman[a], Lisa Lamberson[a], Nicholas Smith[a], William LaCourse[b] and Alastair Cormack[b]

e. Science and Technology Division, Corning Incorporated, Corning, NY 14831, USA
f. New York State College of Ceramics at Alfred University, Alfred, NY 14802, USA

ABSTRACT

Recent experimental work has suggested that bulk and/or surface chemistry (specifically coordination-type structural defect state(s)) plays a critical role in how glass surfaces accumulate charge [1]. One of the best ways to test this hypothesis is through molecular dynamics (MD) simulation of surfaces with specific target compositions, and comparing the results with experimental measurements of surface conductivity/charge, chemistry and/or environmental interaction dynamics. Any conclusions stemming such a comparison can only be considered valid if the simulated material is as close to "real" as possible. As such, full characterization of MD bulk and resulting surface structures along with the corroboration of published experimental/theoretical data is essential. In the present article, we report on bulk and surface characterizations of calcium aluminosilicate (CAS) glass structures in the high silica-tectosilicate composition space ($CaO/Al_2O_3 = 1$) generated via classical MD simulations using modified Teter interatomic potentials. The results show that bulk systems generated using optimized quench/cooling conditions [2] exhibit macroscopic structural properties (i.e. interatomic spacings, angular distributions, coordination defect concentrations, etc.) that correlate well with published experimental and/or theoretical data. Defect densities calculated for subsequently generated surfaces show trending similar to the bulk structures with respect to composition.

[12] Contact: agnellogp@corning.com

Keywords: Molecular dynamics, calcium aluminosilicate, defects

2. INTRODUCTION

Glass charging behavior has been tied to a surfaces' ability to cause the dissociation of close proximity water molecules, resulting in highly active hydroxylated top layer(s) that are prone to contact electrification [1]. As suggested previously in several studies, this ability or potential may be related to structural defect state(s) at the surface such as under-coordinated network formers and/or modifiers [3-5]. To explore this hypothesis in greater detail, a ternary composition series of calcium aluminosilicates (CAS) has been targeted for ongoing simulation and experiment, and represents a more unambiguous compositional and structural analog to the more complicated multi-component flat panel display type compositions that were previously studied. The term "simple" is used loosely here, as the dynamics of the CAS system are by no means fully understood; nonetheless, a system with three components will inevitably be less complicated to understand than one with a significantly higher number. Furthermore, the CAS system has been extensively studied in the past using both experimental as well as theoretical methods to form a broad assessment of structural/chemical characteristics across a wide swath of compositional space.

The tectosilicate join represents the series of compositions wherein the molar ratio $CaO/Al_2O_3=1$, and is one of the most widely studied (at least experimentally) and subsequently well-characterized series' in the CAS system. The charge of the modifier cations (Ca^{2+}) equals the number of aluminum atoms in compositions along this particular join [6]. As a consequence, these glasses should be entirely charge-compensated and—in principle—devoid of any intrinsic defects such as non-bridging oxygens (NBO) [7,8], however several groups have observed otherwise. Stebbins et al has extensively characterized structural defect states in CAS glasses, using primarily Nuclear Magnetic Resonance (NMR) techniques. Published ^{17}O NMR data has reported NBO concentrations of up to 5% (NBO/O_{total}) in otherwise stoichiometrically neutral CAS glasses [6,9-11]. In unrelated work, Toplis has explained observed deviations in viscosity data from ideal predicted values in charge-compensated sodium and/or calcium aluminosilicate glasses through the presence of excess NBO [12, 13]. Stebbins group went on to explain that, in order to compensate excess charge in these systems, additional

structural defects form, such as low levels of tri-clustered oxygen (O_{C3}) [11,14][13] and/or up to 2-3% 5,6-coordinated aluminum ($Al_{C5,C6}$) [10, 14]. Even higher concentrations (up to 8%) of over-coordinated aluminum associated with NBO formation have been reported by Neuville et al in CAS glasses [15-16] and crystals of similar composition [17] using a combination of NMR and Raman/X-ray Absorption Near-Edge (XANES) spectroscopies[14].

Molecular Dynamics (MD) simulations have also been used to explore the structural/chemical properties of CAS glasses, though—somewhat surprisingly— few studies have dealt specifically with compositions lying on the $CaO/Al_2O_3 = 1$ join. The majority of relevant MD studies on CAS glasses have been reported by Neuville's group. Cormier et al. used Born-Mayer-Huggins (BMH) potentials in classical MD simulations of charge compensated silica-rich (~76%) and silica-poor (~12%) CAS glasses [18] where Al_{C5}, O_{C3} and NBO concentrations of 0-0.4%, 3-11% and 7-13% were reported, respectively. The authors studied the same compositions experimentally in ref. 15 as well as through XANES measurement [19], though in the latter case oxygen speciation was not discussed and the detection limits of the technique prevented any quantification of Al_{C5} concentrations. Additional work from the same group by Jakse et al. compared neutron diffraction data with *ab initio* Density Functional Theory (DFT) calculations on low silica (12%-19%) compositions along the $CaO/Al_2O_3 = 1$ join [20]. Jakse' data for coordination defect concentrations were consistent with the classical MD results reported in [18], with the exception of a small but noticeable discrepancy in Al_{C5} concentration (0.38% vs. 2.4%). Considering the significant difference in calculated structure size (5184 atoms in [18] vs. 256 atoms in [20]) the degree to which the two studies coincide is quite impressive. With the exception of additional classical MD studies by Zheng et al. [21] and Tandia et al. [50], CAS data within this particular composition space is not well documented. Experimental techniques that possess adequate resolution to study surface properties on this scale are extremely limited. As such, the small amount of available data

[13] Authors of ref. 12-13 also discuss oxygen tri-clusters in tectosilicate glasses at length in connection with the presence of excess NBO.

[14] Authors of refs. 17,18 also discuss impacts on viscosity/fragility stemming from the presence of structural defects similar to discussions contained in Toplis' publications [12,13].

is comprised almost entirely of MD simulations. To the authors' knowledge, the only studies to deal specifically with MD simulations of CAS surfaces were conducted by Ganster et al. [22,23], though their composition of interest (21%CaO–12%Al_2O_3–67%SiO_2) is not immediately relevant to our current work.

The purpose of the present article is twofold. First, we report on the structural characteristics of simulated bulk/surface CAS structures along the tectosilicate join generated via classical molecular dynamics using modified Teter interatomic potentials and optimized cooling parameters [2]. Secondly, we seek to provide a valuable contribution to the overall field of MD simulations of multi-component glass systems. As indicated by the literature review, very few theoretical studies (bulk- or surface-based) have been conducted on CAS systems along the $CaO/Al_2O_3 = 1$ join, and even fewer yet have focused on the high silica (>50%) portion of the space. As such, we provide one of the first known detailed bodies of MD data on silica-rich charge-compensated CAS glasses.

3. SIMULATION DETAILS AND APPROACH

The Gromacs molecular dynamics simulation package [24,25] was used for glass structure generation under NPT conditions, where pressure and temperature were controlled via Berendsen baro/thermostats. Volume was allowed to vary with temperature in order to compensate for fluctuations in system internal energy. Periodic boundary conditions were imposed to alleviate finite size effects. A three term Buckingham potential [26] was used to calculate interatomic forces between adjacent atoms i and j:

$$\boldsymbol{\Phi_{ij}(r) = A_{ij} e^{-\left(\frac{r}{\rho_{ij}}\right)} - \frac{C_{ij}}{r^6} + \frac{q_i q_j}{4\pi\varepsilon_0 r}} \quad (1)$$

Potential parameters A_{ij}, ρ_{ij} and C_{ij}, which were developed by Teter [27] and adapted by Cormack [28] are detailed in table 1. Cationic pair interactions were neglected in the simulations.

Table 8: Interatomic Potential Parameters Used for MD Simulations

Interaction (ij)	A_{ij} (eV)	P_{ij} (Å)	C_{ij} (eV/Å^6)
Si-O	13702.905	0.193817	54.681
Al-O	12201.417	0.195628	31.997
Ca-O	7747.1834	0.252623	93.109
O-O	2029.2195	0.343645	192.58

Four CAS glasses with variable silica composition were chosen for the present study: 25%CaO-25%Al_2O_3-50%SiO_2, 20%CaO-20%Al_2O_3-60%SiO_2, 15%CaO-15%Al_2O_3-70%SiO_2 and 10%CaO-10%Al_2O_3-80%SiO_2. The convention $CAS_{x,y,z}$ where x, y and z

refer to CaO, Al_2O_3 and SiO_2 content, respectively, will be used for the remainder of the article. Bulk glasses were generated by filling ~64nm^3 boxes with ~6000 randomly distributed atoms corresponding to the desired stoichiometry, and running a 67ps (320,000 time steps at 2fs/step) equilibration trajectory at 3000K followed by quench and subsequent cooling steps. Coordination defect concentrations (Al_{C5}/Al_{total}, O_{C3}/O_{total} and NBO/O_{total}) were evaluated every 300K from 3000K to 300K. Radial and angular distribution functions ($g_{ij}(r)$ and $g_{ij}(\theta)$) were also calculated for each composition at 2500K, 1000K and 300K to assess structural evolution vs. temperature. Details regarding the cooling cycle parameters and/or analytical approaches can be found in our previous work on MD simulations of SiO_2 [2].

"Fracture"-type CAS surfaces were generated from the bulk structures using a vacuum gap method based on work by Garofalini [30,31][15] and Du [29]. The original structures were duplicated, and stacked on top of each other creating new simulation boxes of the same x (l_x) and y (l_y) dimensions, but double the z (l_z) dimension. This process effectively created new expanded structures, where the x and y coordinates of the atoms contained within the top half were identical to those in the bottom half but the z coordinates were exactly $+l_z$ greater. The atoms in the bottom half of the box were then frozen (kinetic energy = 0) in order to simulate the bulk region of the glass, and the atoms in the top half were left unconstrained so as to mimic surface states left to equilibrate under set conditions. A vacuum gap of ~40Å was then inserted on top of the stack to complete the basis' for vacuum fracture surface generation. Periodic boundary conditions were maintained for the expanded system trajectories, where the 40Å gap was large enough to ensure that the opposite surfaces did not interact with one another. The setup process for an arbitrary structure is shown in figure 1 for visual reference.

[15] Same method as used in [27] and similar to one of two techniques reported in Ganster's work on CAS compositions[22]

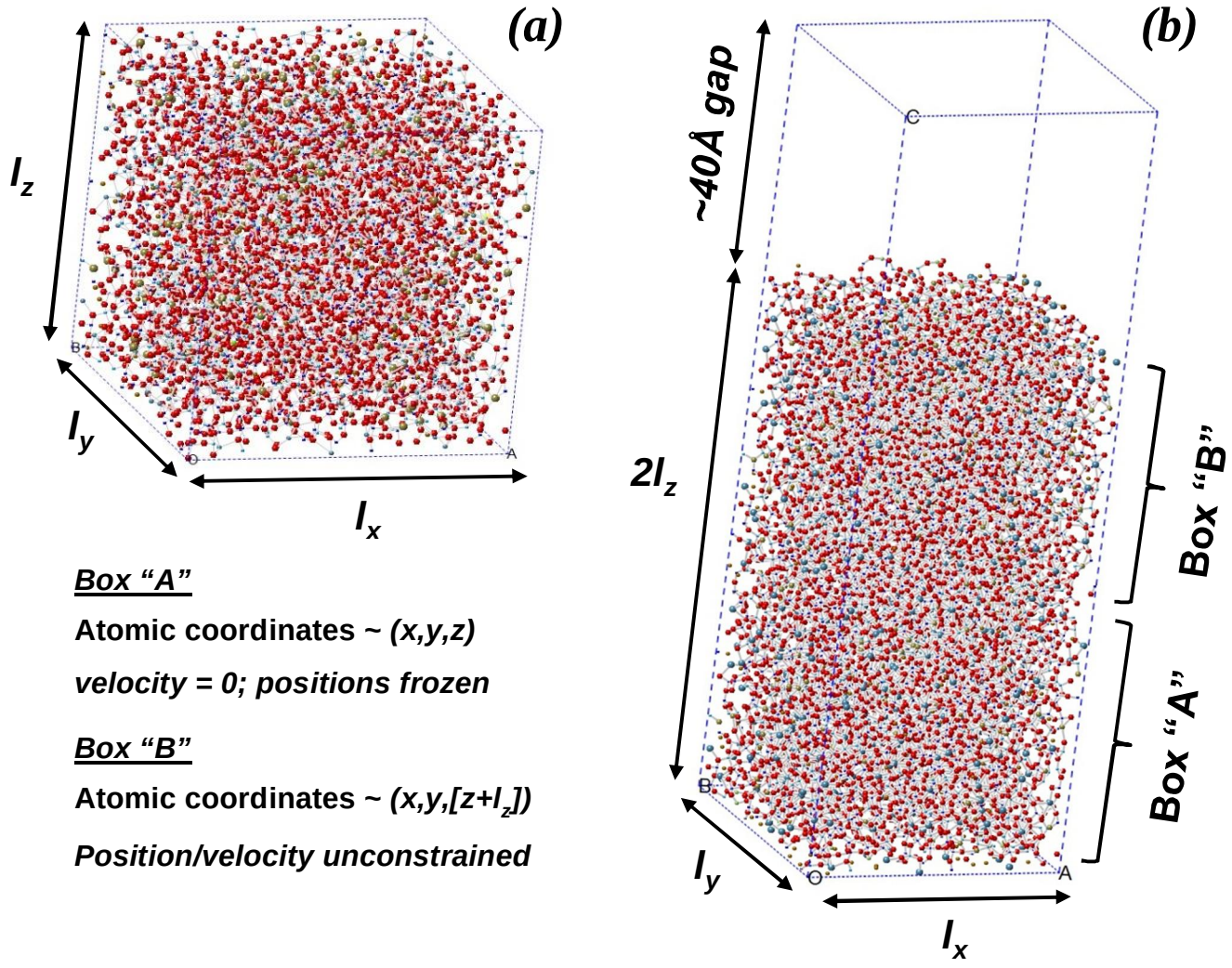

Figure 24: (a) Visualization of simulation box for bulk CAS glass (b) Visualization of "vacuum gap" CAS structure for surface generation.

MD simulations were run on the newly formed "vacuum gap" glasses in the following order (final frame of trajectory was used as the input for the following run):

1. 5ps (0.5fs time step – 10,000 steps) 300K equilibration
2. 5ps (0.5fs time step – 10,000 steps) 700K equilibration
3. 5ps (0.5fs time step – 10,000 steps) 1050K equilibration
4. 100ps (0.5fs time step – 200,000 steps) 1400K equilibration
5. Standard cooling cycle from 1400K – 300K [2]

The final surfaces were analyzed for defect densities (defects/$Å^3$) in the near surface region (top 5Å). To put these calculations in context with previous electrification experiments [1], defect densities were also converted into total expected defect populations under calculated contact area between a small metal sphere and a flat glass surface.

4. RESULTS AND DISCUSSION

4.1 Bulk CAS analysis

4.1.1 Radial Distribution Functions $g_{ij}(r)$

All $g_{ij}(r)$ data was calculated by integrating appropriate bond lengths over 100 separate frames (i.e. time steps) within an individual 20K trajectory; specifically those run during the cooling cycle at 2500K, 1000K and 300K. Figures 2a-d show $g_{Si\text{-}O}(r)$ for the simulated CAS compositions at variable temperatures centered on nearest neighbor peaks. The nearest neighbor peak positions (~1.61Å) (as well as second order peaks not shown in the figures (~4.12Å)) remained consistent across all temperatures. Similar behavior has been reported for pure SiO_2 at variable temperatures and/or cooling conditions[16] [2, 32-34], indicative of Si-O tetrahedral network stability independent of thermal history. Peak broadening with decreases in magnitude have also been reported, indicating enhanced order in cooled structures [2]. Bond lengths for Ca-O and Al-O were also stable with respect to temperature and exhibited similar dependence in terms of magnitude and/or peak width as the Si-O pair. A closer look at the first order peak of $g_{Si\text{-}O}(r)$ at 300K for each composition revealed a slight broadening with decreasing SiO_2 content (Fig. 3a) that was not immediately visible in figures 2a-d. Broadening was most pronounced on the lower radius side of the peak around 1.57-1.59Å, as indicated in Fig. 3a. Broadening of the second order peak was also observed with decreasing SiO_2 concentration, though in this case higher intensity was observed over a broader range of 4.25-4.5Å on the higher end side of the peak.

[16] Authors in [32-34] primarily focused on higher temperature analysis than the present study

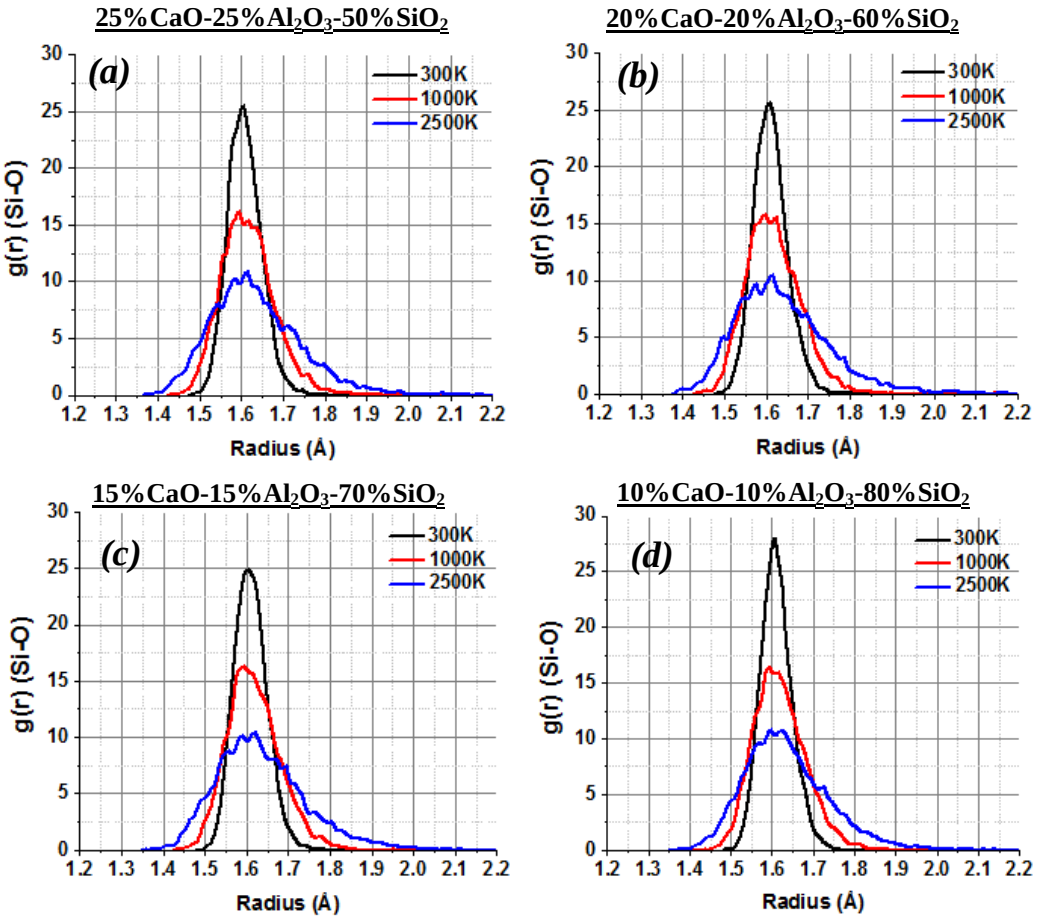

Figure 25: $g_{Si\text{-}O}(r)$ for simulated CAS structures calculated at 2500K, 1000K and 300K for (a) 50% SiO_2 (b) 60% SiO_2 (c) 70% SiO_2 (d) 80% SiO_2.

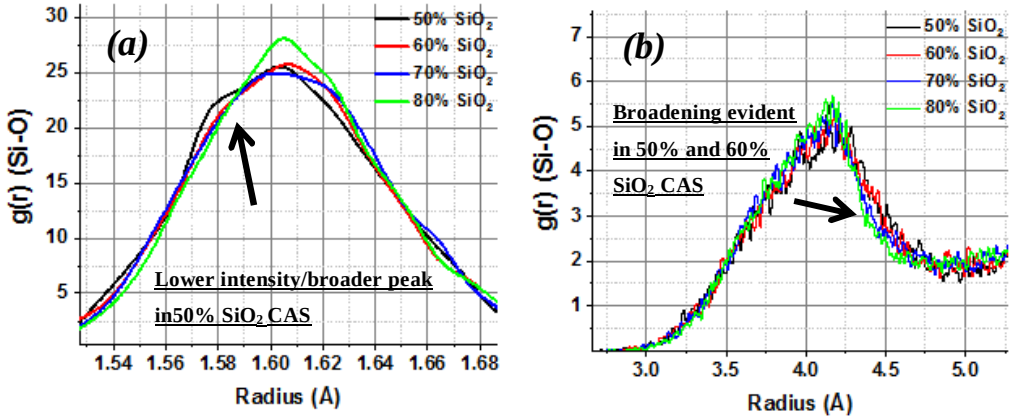

Figure 26: (a) $g_{Si\text{-}O}(r)$ @ 300K focused on nearest neighbor peak for all four CAS compositions. (b) $g_{Si\text{-}O}(r)$ @ 300K focused on second order peak for all four CAS compositions.

Si-O radial distributions in simulated CAS compositions lying on [18,21] as well as off [18,23,35] of the tectosilicate join have exhibited similar behavior, along with those from related studies on sodium silicates and aluminosilicates [36,37]. This has been attributed to increased NBO in CAS glasses as SiO_2 content is decreased, where $g_{Si\text{-}NBO}(r)$ nearest neighbor peak values may be as much as 0.8Å lower than those observed for $g_{Si\text{-}BO}(r)$ (1.52 to 1.60Å) [23]. NBO content does increase with decreasing in SiO_2 in our simulations, which will be discussed in following sections. Interestingly, no comments were made in referenced works regarding second-order peak broadening, though its occurrence can probably be reasonably assumed (however its position on the high side of the peak may not be). We did not observe similar broadening of the $g_{Al\text{-}O}(r)$ and/or $g_{Ca\text{-}O}(r)$ nearest neighbor peaks (figures 4a and 4b, respectively). This, along with the subtlety of the peak broadening in $g_{Si\text{-}O}(r)$, may be due to the high silica content (50-80%) of our CAS compositions as opposed to the lower silica content compositions (12%-40%) reported in the literature, which may produce more obvious differences.

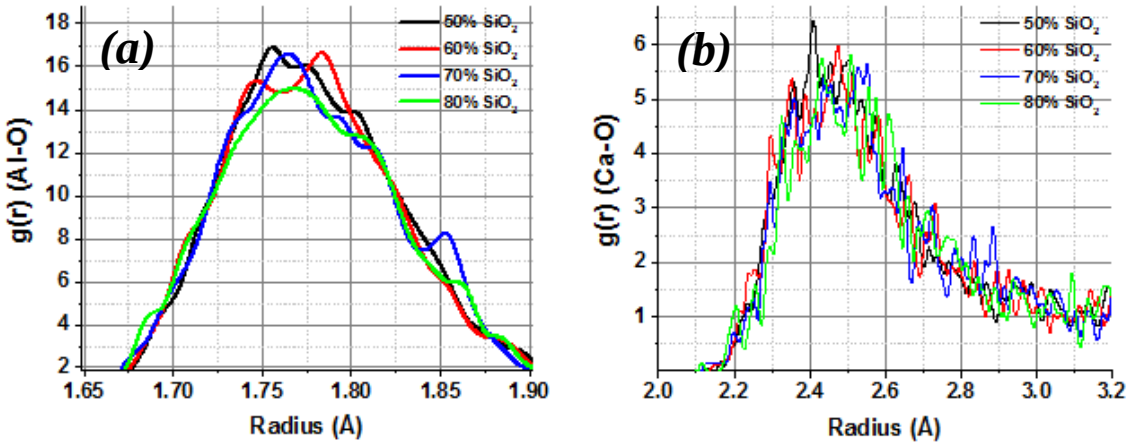

Figure 27: (a) $g_{Al\text{-}O}(r)$ and (b) $g_{Ca\text{-}O}(r)$ for all simulated CAS compositions.

Table 2 lists average nearest-neighbor peak values for $g_{Si\text{-}O}(r)$, $g_{Al\text{-}O}(r)$and $g_{Ca\text{-}O}(r)$ (corresponding to Si-O, Al-O and Ca-O pair interatomic distances, respectively) for our simulations, alongside experimental data reported in the literature for relevant CAS

compositions. Peak values were calculated using Gaussian fits. Data for glasses along the tectosilicate join, as well as for those lying in other compositional spaces, are included. The data reported here, for the most part, agrees well with that published previously, indicating that the observed short range order in the simulations is reasonable. Ca-O values are slightly higher than most previous reports. The authors of ref 9 suggest that, based on comparisons between XANES spectra of several CAS glasses and crystalline anorthite, the local Ca environments the two systems are likely quite similar. The reported average Ca-O distance of ~2.49Å corresponds to a wide range of values (2.29-2.83Å), so suggests our data is within reasonable bounds.

Table 9: Si-O, Al-O And Ca-O Interatomic Distances. (1) Authors Report Separate Si-BO And Si-NBO Data. Values Reported Here Reflect an Average. (2) Authors Present Data Using 3 Separate Potentials. Values Reported Here Represent an Average of the 3 Resultant Figures

		Interatomic distance (Å)			
Composition	Data type	Si-O	Al-O	Ca-O	Ref
$CAS_{61,39,0}$			1.765	2.36	
$CAS_{55,35,10}$	X-Ray/Neutron Diffraction	1.62	1.76	2.35	38
$CAS_{49,31,20}$		1.62	1.76	2.35	
$CAS_{21,12,67}$	Classical/ *ab initio MD*	1.61	1.725	2.33	35 (1)
$CAS_{30,10,60}$	Classical MD	1.62	1.76	2.39	39 (2)
$CAS_{21,12,67}$	Classical MD	1.6	1.76	2.5	23
$CAS_{30,30,40}$	Classical MD	1.6	1.77	2.4	21
$CAS_{44,44,12}$		1.63	1.79	2.34	
$CAS_{41,40,19}$	ab initio DFT	1.63	1.79	2.34	20
$CAS_{44,44,12}$	Neutron	1.66	1.75	2.3	
$CAS_{41,40,19}$	diffraction	1.66	1.75	2.32	
$CAS_{17,17,66}$	Energy-	1.632	1.773		
$CAS_{25,25,50}$	Dispersive	1.647	1.772		40
$CAS_{33,33,33}$	XRD	1.63	1.762		
$CAS_{12.5,12.5,75}$		1.6	1.75	2.32	
$CAS_{25,25,50}$	High-Energy	1.6	1.75	2.36	41
$CAS_{33,33,33}$	XRD	1.6	1.75	2.34	
$CAS_{25,25,50}$		1.605	1.774	2.46	
$CAS_{20,20,60}$	Classical MD	1.606	1.773	2.46	Present
$CAS_{15,15,70}$		1.607	1.774	2.46	work
$CAS_{10,10,80}$		1.608	1.774	2.46	

4.1.2 Bond angle distribution (BAD) functions ($g_{jji}(\theta)$)

Intra- (O-Si-O and O-Al-O) and inter-tetrahedral (Si-O-Si and Al-O-Al) bond angles were evaluated at various points during the cooling cycle to assess any short-medium range systematic structural changes during transition from molten to cooled glassy states. Temperature dependence of the calcium environment (O-Ca-O) was also assessed. Figures 5a and b show $g_{O\text{-}Si\text{-}O}(\theta)$ and $g_{O\text{-}Al\text{-}O}(\theta)$, respectively for the simulated $CAS_{25,25,50}$ structure at 2500K, 1000K and 300K. The data presented here was obtained from the same simulations as the data in figs. 2a.

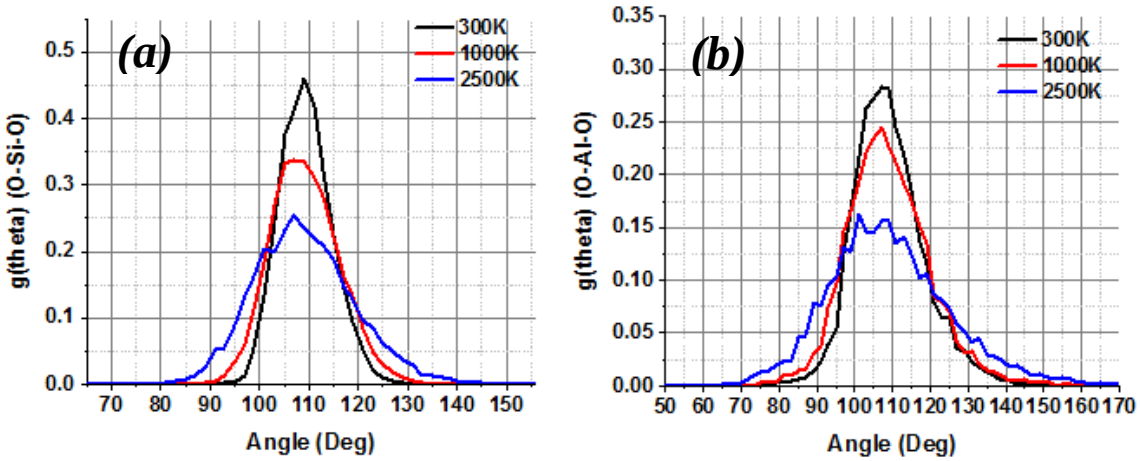

Figure 28: BAD functions for $CAS_{25,25,50}$ at 2500K, 1000K and 300K. (a) $g_{O\text{-}Si\text{-}O}(\theta)$ (b) $g_{O\text{-}Al\text{-}O}(\theta)$.

Bond angle data show similar trending to interatomic spacing data with respect to variations in temperature. Peak positions of ~108.9° and ~107.7° for $g_{O\text{-}Si\text{-}O}(\theta)$ and $g_{O\text{-}Al\text{-}O}(\theta)$, respectively remain stable across the calculated temperature range, with perhaps a ~0.5-0.7° shift to lower angles at 2500K for both tetrahedral units, though this is difference is close to the fit error. These values approach the ideal tetrahedral angle of 109.5°, which represents perfect system symmetry [21], and also agree closely with NMR measurements on amorphous silicates [42]. Increases in peak magnitude along with corresponding decreases in peak width are consistent with increased system order below the glass transition. The shift to slightly lower angles in O-Al-O tetrahedra relative to O-

Si-O has been observed previously in several experimental [42] as well as simulation-based [21,23,39] studies, and has been attributed to the greater rigidity of Si tetrahedra as compared with similar Al structural units [39]. The authors not only observed shifts to lower angles, they also commonly found that O-Al-O distributions were broader relative to those observed for O-Si-O. Our simulation data agree well with these findings, where FWHM of 19.1° and 12.3° were calculated for O-Al-O and O-Si-O, respectively, at 300K. Intra-tetrahedral BAD trending (i.e. stable position, increase in magnitude, decrease in FWHM) with respect to decreases in temperature were consistent across all investigated compositions. O-Ca-O bond angles for $CAS_{25,25,50}$ at variable temperatures are shown in figure 6.

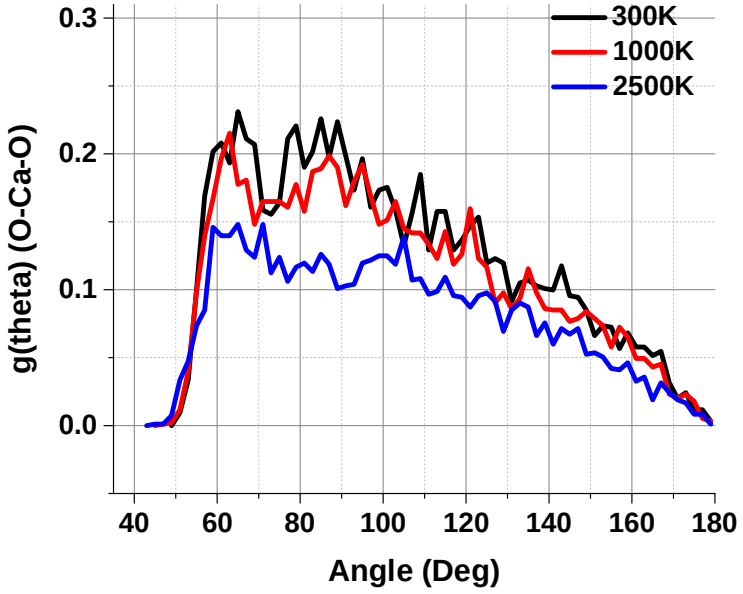

Figure 29: BAD ($g_{O\text{-}Ca\text{-}O}(\theta)$) function for $CAS_{25,25,50}$ at 2500K, 1000K and 300K.

The data show broad overall angular ranges, with small primary peaks at approximately 65°, followed by wide distributions from ~80°-180°. Similar results have been reported for relevant simulated CAS compositions, where the authors claimed that these types of distributions were consistent with the superposition of cubic and octahedral symmetries with specific angles, and indicative of complex coordination environments [20]. Peak positions/widths were not particularly affected by decreases in system temperature,

though the magnitude did increase from 2500K to 1000K. This behavior was again consistent across all compositions.

Figures 7a-b show inter-tetrahedral BAD functions ($g_{Si\text{-}O\text{-}Si}(\theta)$ and $g_{Al\text{-}O\text{-}Al}(\theta)$) for the simulated $CAS_{25,25,50}$ structure at 2500K, 1000K and 300K.

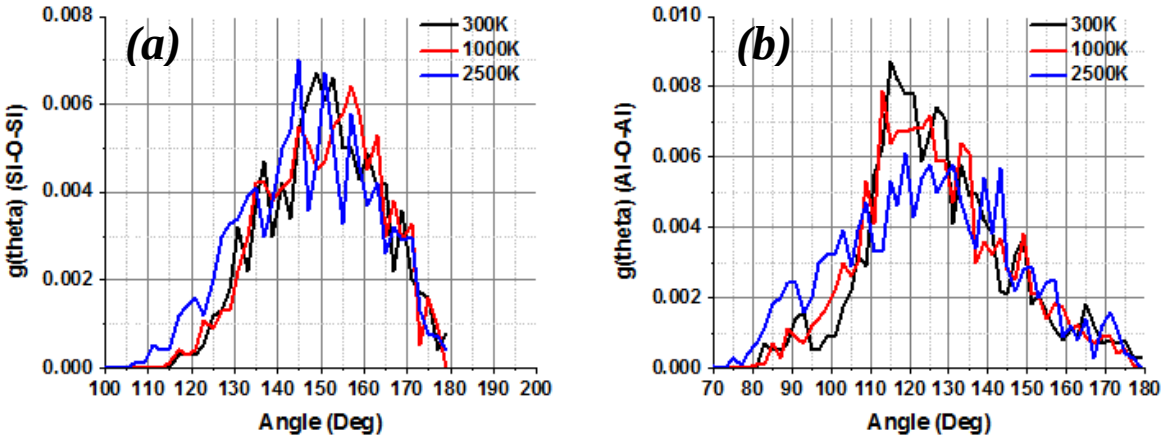

Figure 30: BAD functions for $CAS_{25,25,50}$ at 2500K, 1000K and 300K. (a) $g_{Si\text{-}O\text{-}Si}(\theta)$ (b) $g_{Al\text{-}O\text{-}Al}(\theta)$.

Contrary to intra-tetrahedral bond angle data, peak magnitudes for Si-O-Si and Al-O-Al did not noticeably increase as system temperature was lowered. A slight broadening at lower angles may be noticeable in the data at 2500K for both linkages, though not nearly to the degree observed in figures 5a and 5b. This is likely due to medium range order (more closely reflected in inter-tetrahedral bonds) being established in these structures at higher temperatures than shorter range order, which is reflected more closely in the measurement of intra-tetrahedral angles. As was the case with O-Si-O, O-Al-O and O-Ca-O distributions, the Si-O-Si and Al-O-Al peak positions/temperature dependences shown in figures 6a and 6b were consistent across all compositions. The data in figure 7b appear to suggest that our simulations violate Loewenstein's aluminum avoidance principle, which states that Al-O-Al linkages are less energetically favorable than those of the Si-O-Al type [43], and therefore should not be found in low Al% CAS compositions [35]. The Al avoidance principle has been shown experimentally to be

violated in some Ca containing glasses/melts [9,44-45]. The authors of ref. 9 focused specifically on CAS compositions along the tectosilicate join, where they found as much as 20% Al-O-Al linkage in the low silica glass. Small amounts of Al-O-Al linkages have also been observed in simulated CAS systems [18, 23,35,39] and attributed to a high concentration of electrostatic charge around the divalent Ca^{2+} ions forcing Al atoms closer together and promoting the formation of Al-O-Al bonds [18] . Comparisons of O-Si-O, O-Al-O and O-Ca-O BAD functions at variable silica content show little to no detectable differences at 300K, as shown in figures 8a-8c, respectively. The data suggest that in the high silica-low alumina regime, compositional changes along the Al_2O_3/CaO = 1 join do not significantly affect the network structure.

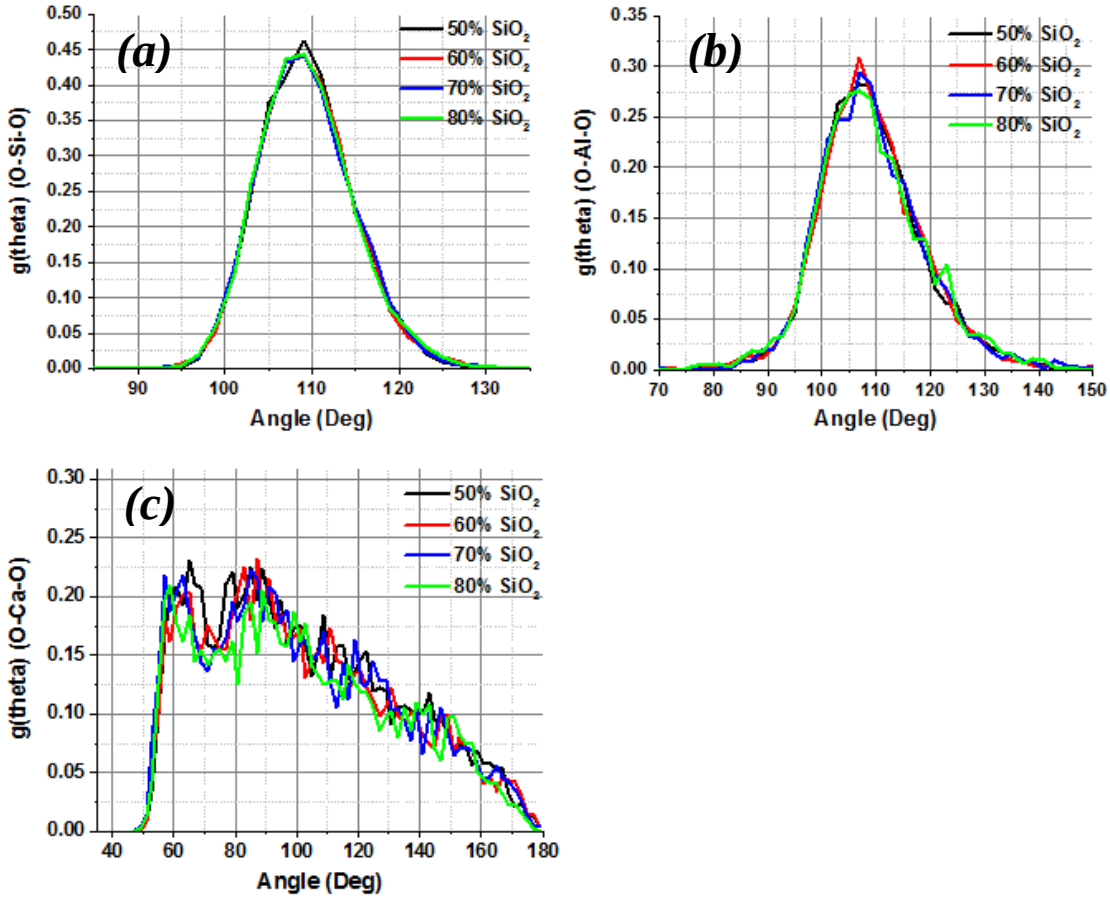

Figure 31: (a) O-Si-O (b) O-Al-O and (c) O-Ca-O BAD functions for CAS structures with variable silica content at 300K.

Published simulation data for intra-tetrahedral BADs (as well as O-Ca-O) spanning a wide range of CAS compositions, both on and off of the charge-compensated join, report similar values and/or chemical-dependent stability [20,21,23,35,39]. The authors of ref. 20 observed a small extension/broadening of the O-Al-O distribution on the high angle side between approximately 140° and 160° for low silica (12%-19%) CAS structures, which they attributed to the presence of five-coordinated aluminum (Al_{C5}). We observe no such broadening in our data, though the relative concentrations of Al_{C5} detected within the high silica compositions here (~0-2%) are quite low comparatively (~10% in ref 10). This will be discussed in more detail later. Inter-tetrahedral BADs show some variability as functions of composition, as the data in figures 9a-b show, where corresponding decreases/increases in Si-O-Si/ Al-O-Al BAD magnitudes, respectively, were observed as Al was substituted into the network structure.

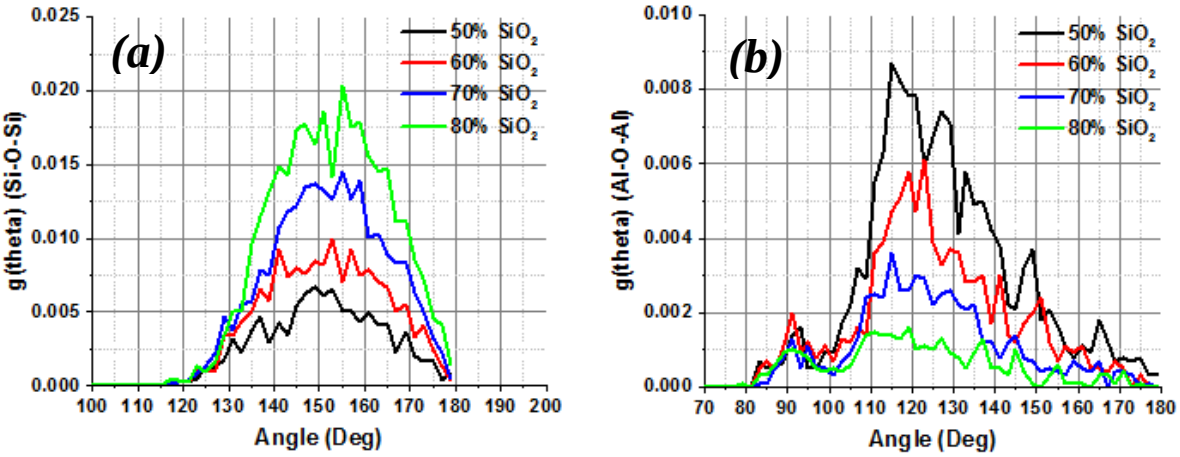

Figure 32: (a) Si-O-Si (b) Al-O-Al and BAD functions for CAS structures with variable silica content at 300K.

Average peak values of ~152° and ~116.5° for Si-O-Si and Al-O-Al, respectively, were stable across the compositional space, though the small amounts of Al-O-Al linkages present in these structures do not provide sufficient data to draw reliable statistical conclusions. The observation of larger Si-O-Si peak values relative to Al-O-Al is consistent with previous simulation data [18, 21, 39, 46], where inter-tetrahedral BAD

were shown to be directly correlated with differences in Si-O and/or Al-O bond length [46]. Another interesting feature of the data in figure 9b is the presence of two distinct peaks: the main distribution centered at ~116.5° and a small secondary peak located at ~90°. Similar behavior was observed in Al-O-Al BAD data for simulated CAS structures with high silica content (52-60% - ref. 21, 60% - ref. 39), though the authors did not discuss it. We will continue to investigate this feature as part of future study. Table 3 lists average CAS bond angles and associated peak widths for our simulated structures, along with published data for comparison. Values were obtained once again via Gaussian fits, with the exception of the Al-O-Al values, which were obtained using a bi-Gaussian fit on the primary peak and adding the resultant width values. Compositions along the tectosilicate join, as well as those off of it, are included. The data agree well with published figures, though the calculated Al-O-Al values for our simulations are somewhat lower, comparatively. As mentioned earlier, the very low levels of Al-O-Al linkages in high silica CAS compositions result in poor overall statistics. The non-symmetric fitting functions used to calculate peak values also likely contribute to the discrepancy. Lastly, worth noting is that there is only one reported Al-O-Al data point for a high-silica tectosilicate type composition shown in table 3 ($CAS_{13,11,76}$ – ref. 18). A concentration of ~20% under-coordinated Al (Al_{C3}) was reported for this structure, which was unrealistic (by admission from the authors) and may have presented difficulties in data interpretation.

Table 10: Current and Published Values for Inter-Tetrahedral (Si-O-Si, Al-O-Al) and Intra-Tetrahedral (O-Si-O, O-Al-O) Bond Angles. Data for O-Ca-O is Also Included

		Bond Angles (°) - peak +/- FWHM					
Composition	Data type	Si-O-Si	Al-O-Al	O-Si-O	O-Al-O	O-Ca-O	Ref
$CA_{61,39,0}$	Classical MD and reverse Monte Carlo Calc.		131.31				18
$CAS_{55,35,10}$		144.96	133.48				
$CAS_{49,31,20}$		145.16	132.59				
$CAS_{44,44,12}$		156.89	128.91				
$CAS_{13,11,76}$		154.32	127.11				
$CAS_{21,12,67}$	Classical/ *ab initio MD*	~125		108.8	107.6		35
$CAS_{30,10,60}$	Classical MD	~145-160		108	107		39
$CAS_{21,12,67}$	Classical MD	157		108	107		23
$CAS_{30,30,40}$	Classical MD	152	129	109.3	108.8		21
$CAS_{44,44,12}$	ab initio DFT				~108	~65-180	20
$CAS_{41,40,19}$					~108	~65-180	
$CAS_{50,50,0}$					~108	~65-180	
various silicate glasses	NMR	142-151					42,47
$CAS_{25,25,50}$	Classical MD	151 +/- 33.4	116.3 +/- 26.7	108.9 +/- 12.3	107.7 +/- 19.1	~65-180	Present work
$CAS_{20,20,60}$		151.6 +/- 34.9	116.7 +/- 24.3	108.9 +/- 12.5	108 +/- 19.3	~65-180	
$CAS_{15,15,70}$		152.4 +/- 32.4	115.6 +/- 25.8	108.9 +/- 12.8	107.8 +/- 19.8	~65-180	
$CAS_{10,10,80}$		152.9 +/- 33.1	~117.3	108.8 +/- 12.4	107.7 +/- 20.1	~65-180	

4.1.3 Coordination states

4.1.3.1 Al environment and speciation

Aluminum coordination states were calculated using a cutoff value of 2.4Å, corresponding to the approximate minimum following the nearest neighbor peak in the Al-O RDF (fig. 4a). The data were acquired at 300K increments during the course of cooling using the same procedure as in previous work [2], and plotted as 3D surfaces

with 2D projections in the XY plane. Figures 10a-c show 3D surface plots for Al_{C3}, Al_{C4} and Al_{C5}, respectively, as functions of temperature and silica composition.

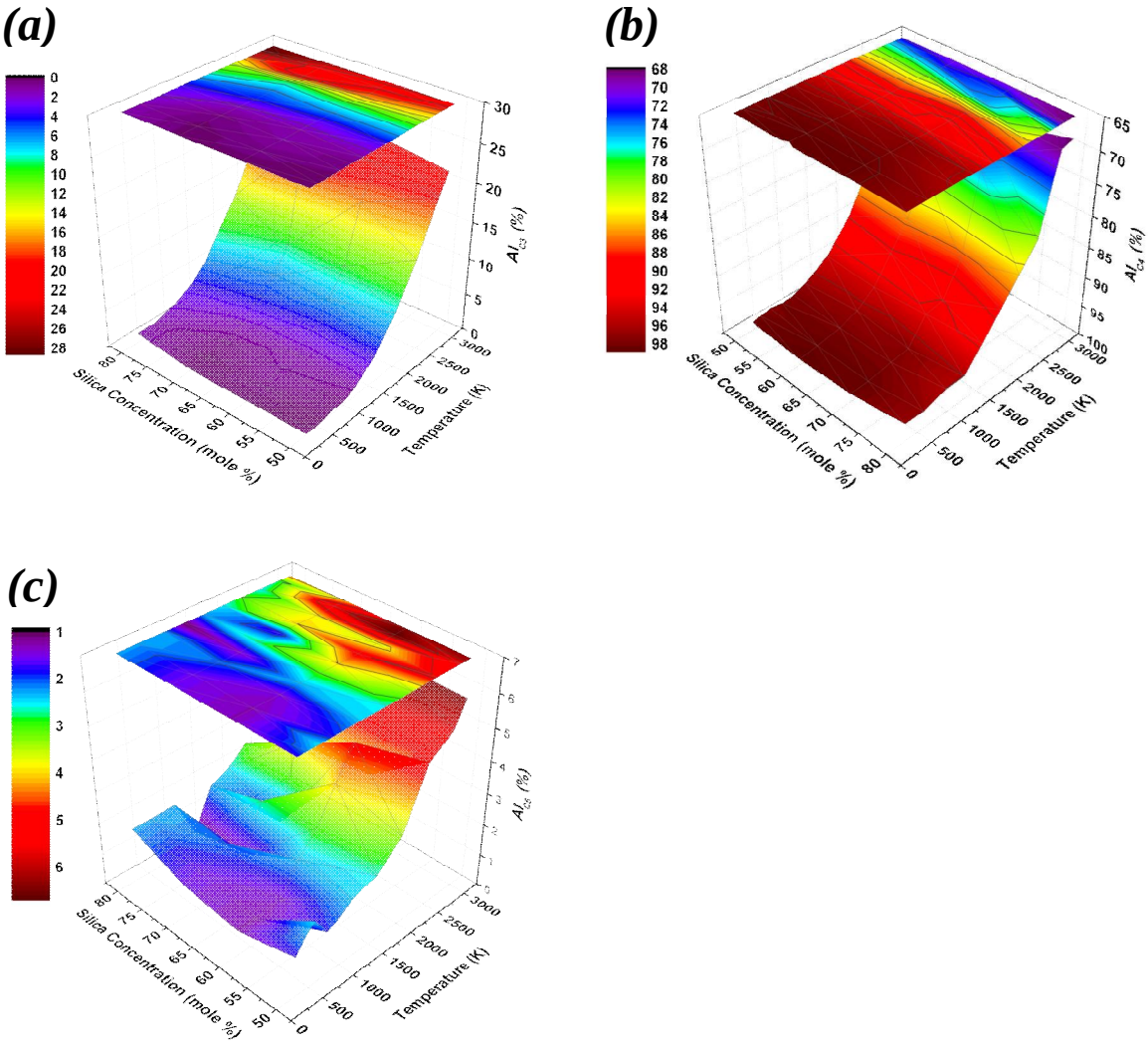

Figure 33: Relative Al coordination states for all simulated CAS structures as functions of temperature and silica concentration (a) Under-coordinated (Al_{C3}) (b) Fully coordinated (Al_{C4}) (note Z-axis reversal) and (c) Over-coordinated (Al_{C5}). No Al_{C6} was detected in any of the structures at room temperature.

As expected, the data suggest that the majority of Al in the simulated structures reach 4-fold coordination at room temperature, with negligible concentrations of under-coordinated Al (totals of 0-1.25% or 0-5 atoms variable with silica content). Al_{C5}

concentrations vary at room temperature across the CAS composition range from 0.8-1.75%, again dependent on silica concentration, where a minimum is observed at 60% silica. As was previously stated in the introduction, the observation of over-coordinated Al in CAS glasses (many times in conjunction with the presence of oxygen triclusters (O_{C3}) which will be covered in later sections) has been commonly reported in the literature. It has been speculated that structural disorder of this type may occur, at least in part, due to the presence of Al-O-Al linkages in Ca containing glasses (which we have observed in our structures) that promote the concentration/formation of negative charge in the form of excess NBO [6]. Over-coordinated formers, such as Al_{C5} and/or Al_{C6} may subsequently form to balance the excess charge within the network due to a deficiency of available charge compensating Ca^{2+} cations [10]. These processes/reactions have frequently been invoked to explain observed features in NMR [6,9,10,11,15,16] as well as XAS/Raman [16,17] spectra, and have also been predicted based on variations in aluminosilicate melt viscosities [12,13]. Furthermore, nearly all referenced studies on simulated CAS systems have reported some detectable concentration(s) of over-coordinated Al, which is consistent with our data, noting however the previously-mentioned scarcity of published information on the silica-rich portion of the tectosilicate join. Al_{C5} concentrations as functions of silica content from published experimental data and/or simulated systems are shown in figure 11. MD data presented in the current study, as well as internally acquired ^{27}Al NMR data on the same CAS compositions, have been included for comparison. Other than our own ^{27}Al NMR study, data published by Neuville et al. [15,16] represent the most complete set of experimentally-measured Al_{C5} concentrations in tectosilicate CAS glasses, though only 3 compositions >50% silica were included. Stebbins published data for $CAS_{25,25,50}$ on three separate occasions [10,11,48], where significantly different relative values for Al_{C5} concentration were reported; however, the authors state in the most recent article [11] that previously calculated Al_{C5} content was likely underestimated due to lower resolution data analysis approaches.

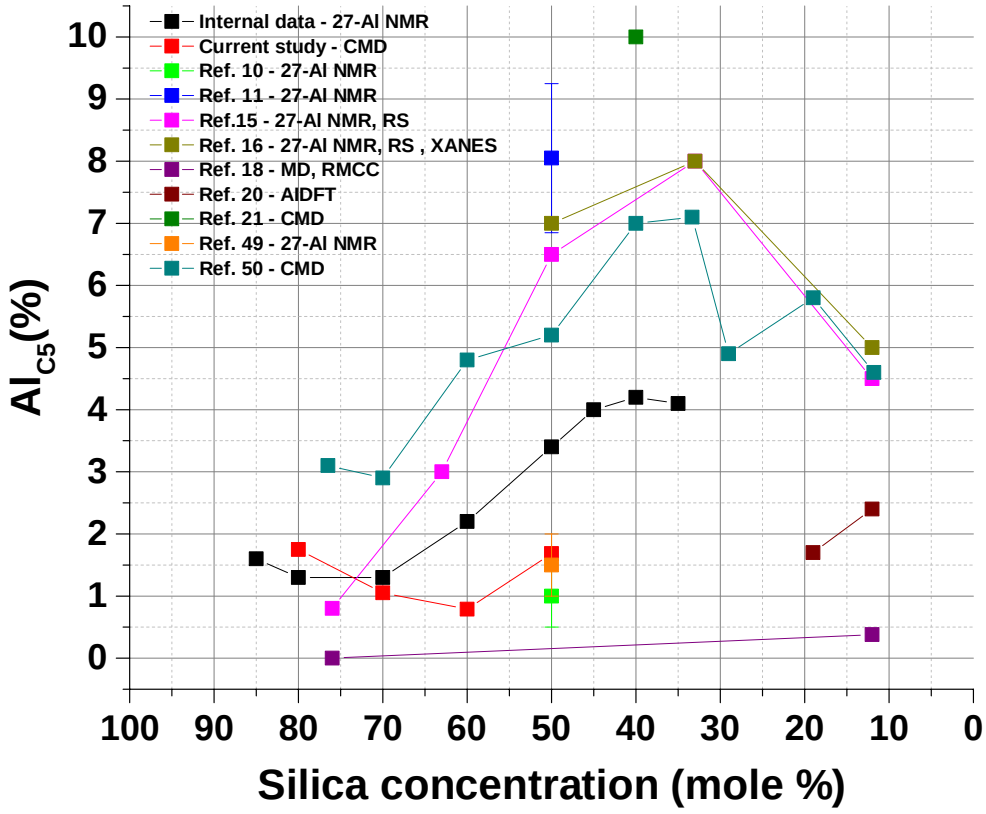

Figure 34: Al_{C5} concentrations from internal/published studies on tectosilicate CAS compositions. Simulation and experimental data are included. Abbreviations: (NMR) - Nuclear Magnetic Resonance, (CMD) – Classical Molecular Dynamics, (RS) – Raman Spectroscopy, (XANES) – X-Ray Near Edge Absorption Spectroscopy, (RMMC) – Reverse Monte Carlo Calculations, (AIDFT) – Ab Initio Density Functional Theory.

This is curious considering that Stebbins' previous estimates of 1-2% Al_{C5} were in better agreement with both our experimental (~3.5%) as well as simulation (~1.7%) results. Our data correlate well with Neuville's data in the 60-80% silica range, exhibiting Al_{C5} concentrations of approximately 1-3%. Features observed in both our MD and ^{27}Al NMR data, are the minima in Al_{C5} concentration at ~60% and 75%, respectively. Due to the lack of published experimental data in the high-silica regime, no reasonable comparisons can be made regarding these minima, though the features likely indicate a significant shift in network structure that occurs over this portion of the compositional space. Comparison of our work with published MD results is also difficult due to a lack of published data. In the one highly relevant study, Tandia et al. calculated Al_{C5} concentrations across most of

the CAS tectosilicate join via classical MD with Matsui interatomic potentials [50]. In the high-silica regime, Tandia's data suggests a somewhat higher Al_{C5} content (~3-5%) than our simulations (~1-2%). A comparison of these results to the referenced experimental data, notably that of Neuville [15,16], suggests good agreement in the 50-60% silica range, but higher deviation in compositions >60%. Our simulations seem to correlate with Neuville's data more closely above 60%, though with only three published data points, this statement is tentative at best. Our own ^{27}NMR dataset is much more complete across this range. For CAS compositions with 50%-60% silica content, internal ^{27}Al NMR values for Al_{C5} content are positioned between our simulation data (~1-1.5%) and that from Tandia et al. (~5%). For compositions >60% silica, our MD and ^{27}Al NMR data converge with Neuville. The data from ref. 50 may also display a similar Al_{C5} minima to that observed in our calculations/NMR results located around the ~70% silica structure, though given the variation across their entire simulation range it is difficult to state this conclusively. One last observation concerning the MD data presented in figure 11 is that the Al_{C5} concentrations calculated for structures in the present work, along with those published by Cormier[18] and Jakse [20] and Tandia [50], are all accompanied by significant proportions of tri-clustered oxygen (O_{C3}) (~3-13%). Perhaps this apparent relationship should come as no surprise, considering these defects' similar roles in excess NBO charge compensation, which will be discussed in greater detail in the following section.

4.1.3.2 Non-Bridging and Tri-Clustered Oxygen (NBO and O_{C3})

Figures 12a-b show calculated concentrations of NBO and O_{C3}, respectively, for all simulated CAS structures as functions of silica content and temperature, expressed in the same manner as the data for Al_{5c} in figures 10a-c. Bond length cutoffs for Si-O bonding were set to 2.1Å, corresponding to the approximate minima following the nearest neighbor peaks in figures 2a-d.

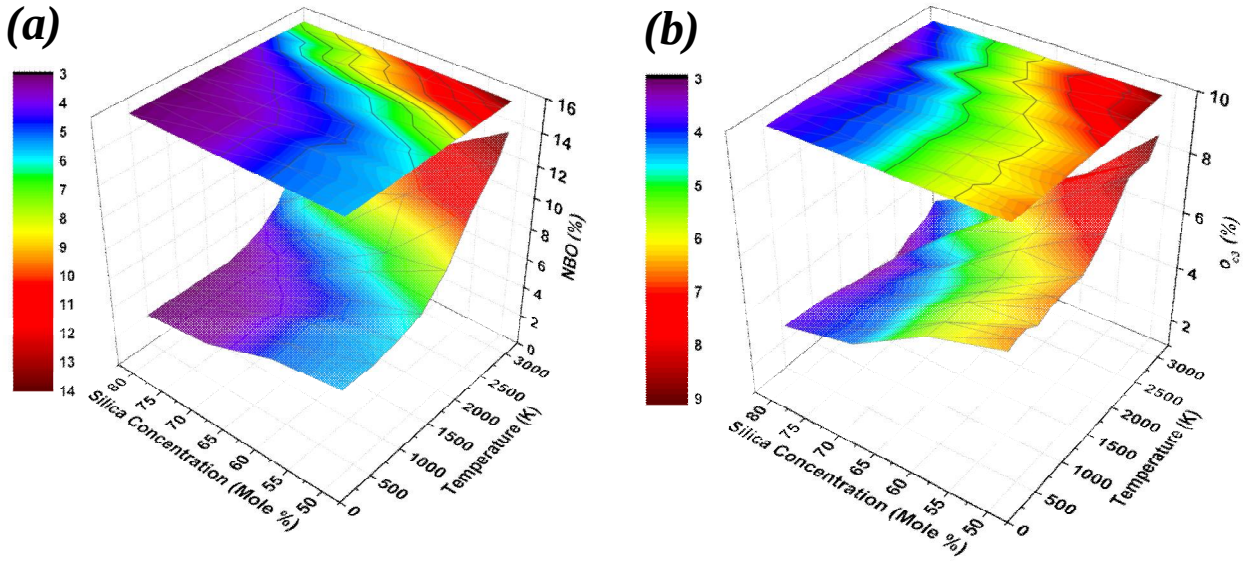

Figure 35: (a) Relative NBO and (b) O_{C3} concentrations in simulated CAS structures as functions of silica concentration and temperature.

There are some notable differences between the trending of aluminum coordination (figs. 10a-c) and that of oxygen-based defects with respect to temperature and/or silica concentration. The data suggests that O_{C3}, and to a lesser extent NBO, concentrations are strongly dependent on fluctuations in silica content relative to changes in temperature. Specifically for the case of O_{C3} occurrence, the data indicates that even at temperatures well above the transition, the relative amount of oxygen atoms in 3-fold coordination is well defined and does not change significantly from melt to cooled glassy state(s). As had been previously mentioned, the existence of NBO in ostensibly "fully-polymerized" CAS glasses has been reported in many of the referenced experimental [6,10,11] and theoretical [18,20,21,50] studies, though the presence of O_{C3} in such glasses has been challenging to experimentally confirm. As such, the existing body of data on O_{C3} concentrations in CAS glasses is comprised solely of MD, whereas published experimental as well as theoretical data are available for NBO. Figures 13a-b show NBO and O_{C3} concentrations, respectively, calculated for tectosilicate CAS glasses as functions of silica content found in the literature, alongside our own results.

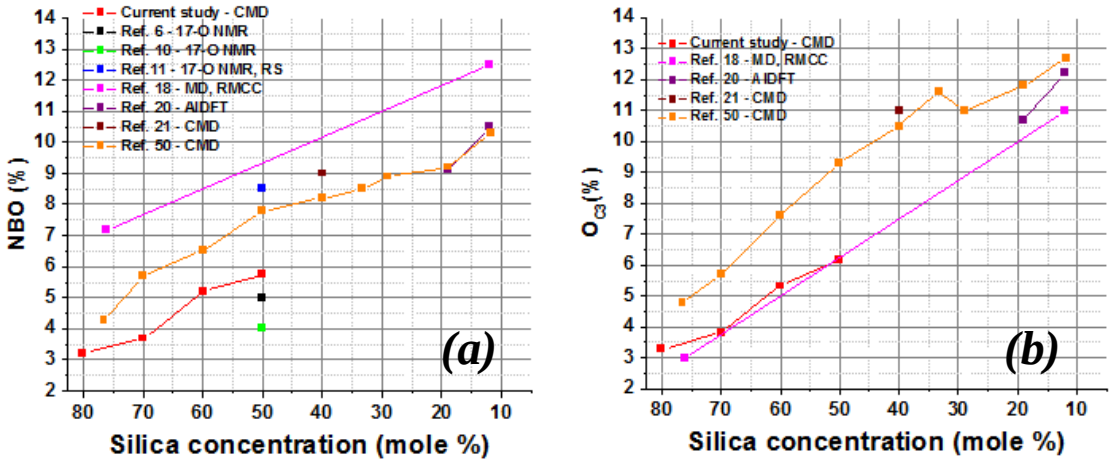

Figure 36: (a) NBO and (b) O_{C3} concentrations in tectosilicate CAS glasses from the present study with published experimental/theoretical data.

The detected concentrations of NBO and/or O_{C3} in simulation data depend on several factors such as interatomic potential used, system size and thermal history, just to mention a few; however the trend of increasing defect concentration(s) with decreasing silica content appears to hold in all surveyed cases. Calculated oxygen defects in our structures also follow this trend whilst exhibiting lower overall values than most other reports.

4.1.3.3 Oxygen and aluminum coordination state(s) relationship

As was previously mentioned, coordination defects, such as Al_{C5} and/or O_{C3}, may form to balance excess charge from NBOs in what should otherwise be fully polymerized CAS glasses. If this were the case, it may be reasonably expected that the total number of over-coordinated oxygen and/or aluminum should approximately equal the number of NBOs. Figure 14 shows the relationship between the total number of over-coordinated oxygen and aluminum (Al_{C5}+O_{C3}) and NBO in our simulated CAS glasses at 300K.

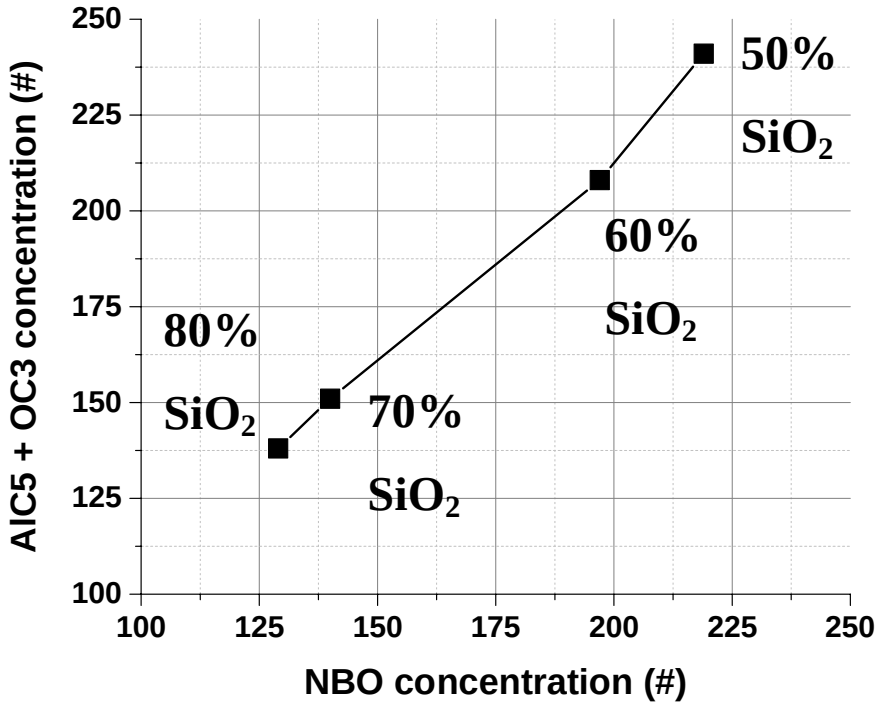

Figure 37: Total number of over-coordinated aluminum (Al_{C5}) and oxygen (O_{C3}) as a function of NBO concentration in simulated CAS structures. Silica concentration at each data point is labeled accordingly.

The nearly linear relationship suggests that charge compensation is a likely reason for over-coordination type defects to form in the simulations. This, along with favorable correlation between our work and data reported elsewhere, allows us to conclude that the current simulation approach for this CAS composition space is sound and produces valid results.

4.2 Surface analysis

The ultimate goal of our study is to investigate the effects of glass surface composition on previously observed charging behavior [1] through comparison of simulation and future experimental measurement of CAS glasses. The bulk structure analyses covered in the previous section suggest that surfaces derived from the base simulations do mimic "real" systems as closely as can be reasonably expected and therefore can be used for reliable study. CAS surface structures were generated for each composition using the procedure described in section 2, and subsequently analyzed for defect concentration/density in the immediate vicinity of the vacuum gap (top ~5Å). This region was defined by inserting an imaginary plane located 5Å from the top most atom into the bulk. Any structural defect found on or above this plane was included in the calculation(s).

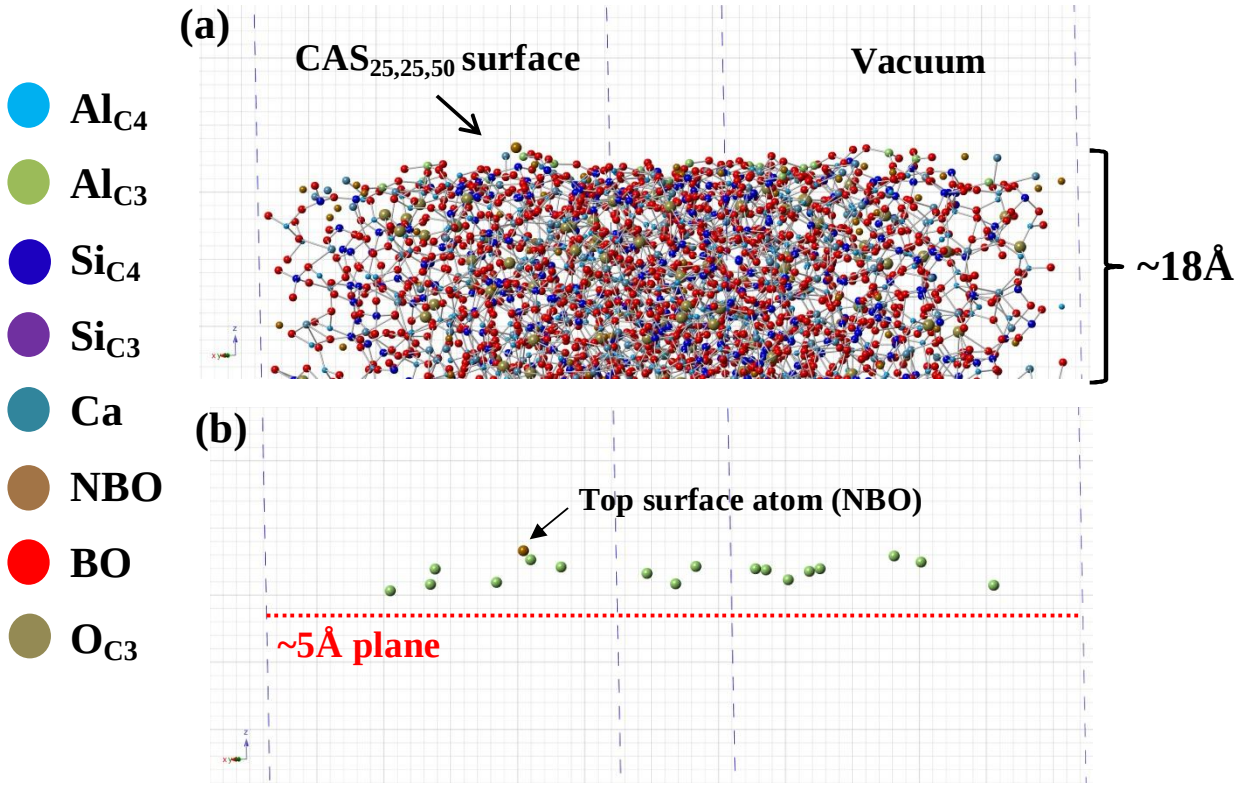

Figure 38: Generated surface structure for $CAS_{25,25,50}$ (a) All atoms (b) Only Al_{C3} highlighted with imaginary 5Å plane within structure measured from top most surface atom. Structures viewed from lattice direction [1.335, -1.771, 0].

For reference, visualizations (using CrystalMaker® 9.1.4) of $CAS_{25,25,50}$ depicting all near surface atoms, alongside the corresponding structure with only Al_{C3} highlighted are shown in figures 15a and 15b, respectively. Near surface NBO, O_{C3}, Si_{C3} and Al_{C5} densities (defects/Å^3) were calculated for each simulated composition and plotted as functions of silica concentration (figure 16). No Al_{C5} was detected in the near surface region for any of the structures. In preparation for future comparison of this simulation data with experimental charge measurements on representative CAS surfaces, defect density values were used to calculate the total number(s) of expected defects in the contacted area between the sphere and glass under Rolling Sphere Test (RST) conditions used in previous experiments [1][17]. These calculations are shown on the secondary Y axis in figure 16.

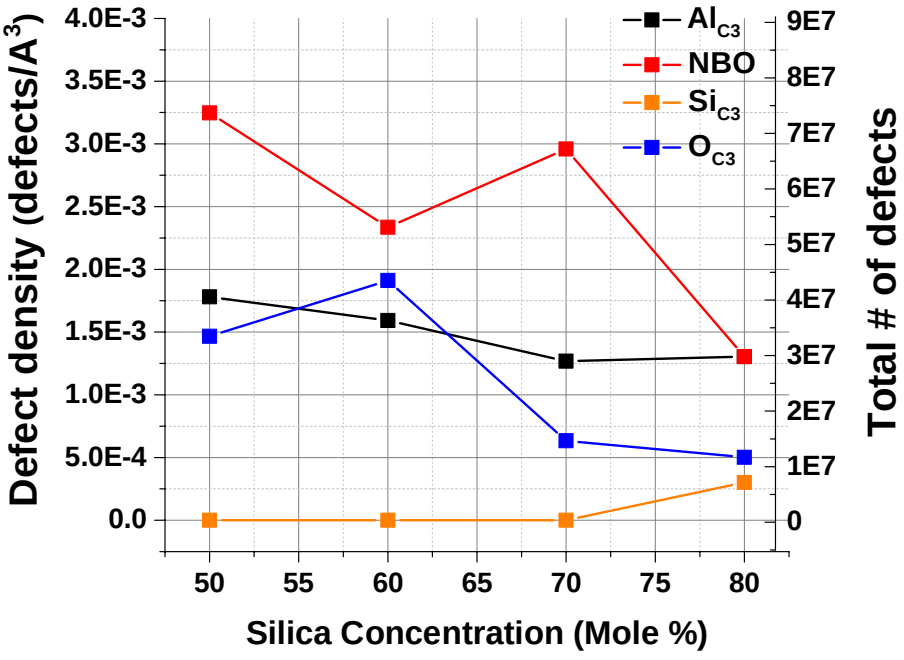

Figure 39: Defect density and total number of defects for near surface region of simulated CAS glasses. Total defect number indicates the expected populations found within contact area between sphere and glass in RST test.

[17] Contact area between sphere and glass calculated assuming gravitational force only using the equation $a = \sqrt[3]{\frac{6mg(1-\gamma^2)r}{E}}$ where m=mass of sphere, g=9.8kg·m/s^2, γ=Poisson ratio (440C steel), r=radius of sphere, E=Young's modulus (440C steel) and a=radius of contact area. Total number of defects calculated for a cylinder of volume = 5πa^2 where 5 is the depth into the glass in angstroms.

The data in figure 16 for oxygen based structural defects correlate well with trends observed for the bulk structures, as shown in figures 12a and 12b. While there is some spread in the data, NBO and O_{C3} surface defect densities generally decrease with increasing silica content. Significant amounts of Al_{C3} were detected in the near surface region, similar to earlier reports [21]. Calculated surface values for Al_{C3} also appear to decrease with increasing silica, though to less of an extent. No Si_{C3} was observed at the surface for any composition under 80% silica content, suggesting that under-coordinated Al is a relatively more stable site under the simulated conditions (vacuum fracture). This observation conflicts with the findings of ref. 21, though that particular study included only one non-compensated CAS composition ($CAS_{21,12,67}$) so direct comparison may be difficult. The presence of under-coordinated network formers should make similar laboratory fabricated surfaces highly reactive under variably humid environments [21], which may contribute to systematic differences in charging behavior. Such reactivity has been recently shown to strongly depend on CAS composition, where glasses with higher silica content exhibited lower dissolution rates/reactivity when placed in aqueous environments [51], which lends further support to our approach here. Experimental electrical measurement of representative surfaces, along with MD interaction of the simulated surfaces with water molecules will be a primary focus' of future studies.

5. CONCLUSIONS

Results from classical MD simulations of silica rich CAS glasses along the tectosilicate join have been reported. Bulk radial/angular distribution function and coordination state analyses suggest that the current MD approach produces reasonable CAS structures with properties that mimic those reported in the literature. Oxygen and aluminum environments vary significantly with silica concentration, and in the case of the latter, temperature. The nearly linear relationship observed between O_{C3}+Al_{5C} and NBO suggests charge compensation to be a likely driver for structural defect formation in these glasses. Calculated defect densities in the near surface (<5Å) region suggest that trends with respect to oxygen based structural defects are similar to those in the bulk, where overall decreases accompany increases in silica content. Significant amounts of surface Al_{C3} were detected in all cases along with a similar, though less pronounced, trend of decreasing concentration with increasing silica content. The relationship between the variable surface defect chemistry observed in our simulations and experimentally measured surface charging behavior will be a focal point of future work.

6. ACKNOWLEDGEMENTS

The authors would like to thank the Corning Display Technologies (CDT) development and fundamental research organizations for funding this work.

7. REFERENCES

[1]. G. Agnello, J. Hamilton, R. Manley, E. Streltsova, W. LaCourse, A. Cormack, "Investigation of contact-induced charging kinetics on variably modified glass surfaces," *Appl. Surf. Sci.*, **356** 1189–1199 (2015).

[2]. G. Agnello, A.N. Cormack, "Coordination state and defect evolution in SiO_2 structures formed using molecular dynamics under variable cooling conditions," *J. Non. Cryst. Solids*, submitted.

[3]. J. Du, A.N. Cormack, "Molecular dynamics simulation of the structure and hydroxylation of silica glass surfaces," *J. Am. Ceram. Soc,*. **88** 2532–2539 (2005).

[4]. G.K. Lockwood, S.H. Garofalini, "Bridging oxygen as a site for proton adsorption on the vitreous silica surface," *J. Chem. Phys.* **131**, (2009).

[5]. G.K. Lockwood, S.H. Garofalini, "Proton Dynamics at the Water − Silica Interface via Dissociative Molecular Dynamics," *J. Chem. Phys. C*, **118** 29750-29759 (2014).

[6]. J. Stebbins, Z. Xu, "NMR evidence for excess non-bridging oxygen in an aluminosilicate glass," *Nature.*, **390** 1996–1998 (1997).

[7]. Mysen, B.O. *Structure and properties of silicate melts*, Elsevier Science and Technology, Oxford, UK, 1988.

[8]. Navrotsky, A. , *Physics and Chemistry of Earth Materials*, Edition 6, Cambridge University Press, Cambridge, UK, 1994.

[9]. J.F. Stebbins, S.K. Lee, J. V. Oglesby, "Al-O-Al oxygen sites in crystalline aluminates and aluminosilicate glasses: High-resolution oxygen-17 NMR results," *Am. Mineral.*, **84** 983–986 (1999).

[10]. J.F. Stebbins, S. Kroeker, S.K. Lee, T.J. Kiczenski, "Quantification of five- and six-coordinated aluminum ions in aluminosilicate and fluoride-containing glasses by high- field high resolution ^{27}Al ," *J. Non. Cryst. Solids.*, **275** 4–9 (2000).

[11]. J.F. Stebbins, E. V. Dubinsky, K. Kanehashi, K.E. Kelsey," Temperature effects on non-bridging oxygen and aluminum coordination number in calcium aluminosilicate glasses and melts," *Geochim. Cosmochim. Acta,*. **72** 910–925 (2008).

[12]. M.J. Toplis, “Peraluminous viscosity maxima in NazO-Alz03-SiOz liquids : The role of triclusters in tectosilicate melts,” *Geochim. Cosmochim. Acta,.* **61** [13] 2605-2612 (1997).

[13]. M.J. Toplis, D.B. Dingwell, “Viscosity maxima of melts close to the ‘charge balanced’ join in the systems Na2O, CaO, MgO)-Al2O3pSiO2: implications for the structural role of aluminum,” *Trans. Am. Geophys. Un.,* **77** F848 (1996).

[14]. J.F. Stebbins, J.V.O. Glesby, S.K. Roeker, “Oxygen triclusters in crystalline CaAl 4 O 7 (grossite) and in calcium aluminosilicate glasses : O NMR,” *Am. Mineral.***, 86** 1307–1311 (2001).

[15]. D.R. Neuville, L. Cormier, D. Massiot, “Al coordination and speciation in calcium aluminosilicate glasses : Effects of composition determined by 27 Al MQ-MAS NMR and Raman spectroscopy,” *Chem. Geology.,* **229** 173–185 (2006).

[16]. D.R. Neuville, L. Cormier, D. Massiot, “Al environment in tectosilicate and peraluminous glasses: A 27Al MQ-MAS NMR, Raman, and XANES investigation,” *Geochim. Cosmochim. Acta,.* **68** 5071–5079 (2004).

[17]. D.R. Neuville, L. Cormier, D. De Ligny, J. Roux, A. M. Flank, P. Lagarde, “Environments around Al, Si, and Ca in aluminate and aluminosilicate melts by X-ray absorption spectroscopy at high temperature,” *Am. Mineral.*, **93** 228–234 (2008).

[18]. L. Cormier, D. Ghaleb, D.R. Neuville, J.M. Delaye, G. Calas, “Chemical dependence of network topology of calcium aluminosilicate glasses: A computer simulation study,” *J. Non. Cryst. Solids,.* **332** 255–270 (2003).

[19]. D.R. Neuville, L. Cormier, A. Flank, D. Massiot, “Al speciation and Ca environment in calcium aluminosilicate glasses and crystals by Al and Ca K-edge X-ray absorption spectroscopy,” *Chem. Geology,.* **213** 153–163 (2004).

[20]. N. Jakse, M. Bouhadja, J. Kozaily, J.W.E. Drewitt, L. Hennet, “Interplay between non-bridging oxygen , triclusters , and fivefold Al coordination in low silica content calcium aluminosilicate melts,” *Appl. Phys. Lett.* **101** 201903 (2012).

[21]. K. Zheng, Z. Zhang, F. Yang, S. Sridhar, “Molecular Dynamics Study of the Structural Properties of Calcium Aluminosilicate Slags with Varying Al2O3/SiO2 Ratios,” ISIJ *Int.*, **52** 342–349 (2012).

[22]. P. Ganster, M. Benoit, J.M. Delaye, W. Kob, “Surface of a calcium aluminosilicate glass by classical and ab initio molecular dynamics simulations,” *Surf. Sci.*, **602** 114–125 (2008).

[23]. P. Ganster, M. Benoit, W. Kob, J.-M. Delaye, “Structural properties of a calcium aluminosilicate glass from molecular-dynamics simulations: a finite size effects study,” *J. Chem. Phys.*, **120** 10172–10181 (2004).

[24]. D. Van Der Spoel, E. Lindahl, B. Hess, G. Groenhof, A.E. Mark, H.J.C. Berendsen, “GROMACS: Fast, flexible, and free,” *J. Comput. Chem.*, **26** 1701–1718 (2005).

[25]. B. Hess, C. Kutzner, D. Van Der Spoel, E. Lindahl, “GROMACS 4 : Algorithms for Highly Efficient , Load-Balanced , and Scalable Molecular Simulation,” *J. Chem. Theory Comput.*, **4** [3] 435-447 (2008).

[26]. R.A. Buckingham, “The Classical Equation of State of Gaseous Helium, Neon and Argon,” *Proc. R. Soc. Lond. A. Math. Phys. Sci.*, **168** 264–283 (1938).

[27]. A.J. Lamphere, “A Structural Study Of A Multicomponent E-Cr Glass Via Molecular Dynamics Simulation,” M.S. Thesis, Alfred University, Alfred, NY, 2015.

[28]. A.N. Cormack, J. Du, T.R. Zeitler, “Sodium ion migration mechanisms in silicate glasses probed by molecular dynamics simulations,” *J. Non. Cryst. Solids.*, **323** 147–154 (2003).

[29]. J. Du, “Molecular Dynamics Simulation of the Structure of Silicate Glasses Containing Hydroxyl Groups and Rare Earth Ions,” PhD Thesis, Alfred University, Alfred, NY, 2004.

[30]. S.H. Garofalini, “A Molecular Dynaics Simulation of the Vitreous Silica Surface,” *J. Chem. Phys.*, **78** [4] 2069-72 (1983).

[31]. B.P. Feuston and S.H. Garofalini, “Topological and Bonding Defects in Vitreous Silica Surfaces,” *J. Chem. Phys.*, **91** [1] 564-70 (1989).

[32]. K. Vollmayr, W. Kob, K. Binder, "Cooling-rate effects in amorphous silica: A computer-simulation study," *Phys. Rev. B.*, **54** 15808–15827 (1996).

[33]. V. V. Hoang, "Static and Dynamic Heterogeneities in Supercooled SiO2," pp. 77-94, Defect and Diffusion Forum, Vols. 242-244, Sept. 2005.

[34]. J. Horbach, W. Kob, "Static and dynamic properties of a viscous silica melt," *Phys. Rev. B.*, **60** 3169–3181 (1999).

[35]. C.C. O, M. Benoit, S. Ispas, M.E. Tuckerman, "Structural properties of molten silicates from ab initio molecular-dynamics simulations," *Phys. Rev. B.*, **64** 1–10 (2001).

[36]. G.E. Brown, G.V. Gibbs, and P.H. Ribbe, "The Nature and the Variation in Length of the Si-O and Al-O Bonds in Framework Silicates," *Am. Mineral.*, **54** 1044 (1969).

[37]. W.S. McDonald, D.W.J. Cruickshank, "A reinvestigation of the structure of sodium metasilicate, Na_2SiO_3," *Acta Crystallogr.* **22** 37–43 (1967).

[38]. M. Bauchy, "Structural, vibrational, and elastic properties of a calcium aluminosilicate glass from molecular dynamics simulations: The role of the potential," *J. Chem. Phys.*, **141**, (2014).

[39]. V. Petkov, T. Gerber, B. Himmel, "Atomic ordering in Cax/2AlxSi1-xO2 glasses (x=0,0.34,0.5,0.68) by energy-dispersive x-ray diffraction," *Phys. Rev. B.*, **58** 11982–11989 (1998).

[40]. V. Petkov, S.J.L. Billinge, S.D. Shastri, B. Himmel, "Polyhedral units and network connectivity in calcium aluminosilicate glasses from high energy X-ray diffraction," *Phys. Rev. Lett.*, **85** 3436(2000).

[41]. R.F. Pettifer, R. Dupree, I. Farnan, U. Sternberg, "NMR determinations of Si-O-Si bond angle distributions in silica," *J. Non. Cryst. Solids.*, **106** 408–412 (1988).

[42]. W. Loewenstein, "The Distribution of Aluminum in the Tetrahedra of Silicates and Aluminates," *Am. Mineral.*, **39** 92 (1954).

[43]. J. Klinowski, S.W. Carr, S.E. Tarling, P. Barnes, "Magic-angle-spinning NMR shows the aluminosilicate framework of ultramarine to be disordered," *Nature.*, **330** 56–58 (1987).

[44]. B. Himmel, J. Weigelt, T. Gerber, M. Nofz, “Structure of calcium aluminosilicate glasses: wide-angle X-ray scattering and computer simulation,” *J. Non. Cryst. Solids.*, **136** 27–36 (1991).

[45]. A. Navrotsky, K.L. Geisinger, P. Mcmillan, G. V Gibbs, “The Tetrahedral Framework in Glasses and Melts - Inferences from Molecular-Orbital Calculations and Implications for Structure, Thermodynamics, and Physical-Properties,” *Phys. Chem. Miner.*, **11** 284–298 (1985).

[46]. I. Farnan, P.J. Grandinetti, J.H. Baltisberger, J.F. Stebbins, U. Werner, M. A Eastman, “Quantification of the disorder in network-modified silicate glasses,” *Nature.*, **358** 31–35 (1992).

[47]. S.K. Lee, J.F. Stebbins,” The Structure of Aluminosilicate Glasses : High-Resolution NMR Study 17Oand 27Al 3QMAS NMR study,” *J. Phys. Chem. B.*, **104** 4091–4100 (2000).

[48]. Baltisberger, J. H., Xu, Z., Stebbins, J. F., Wang, S., Pines, A., “Triple-quantum two-dimensional 27Al magic-angle spinning nuclear magnetic resonance spectroscopic study of aluminosilicate and aluminate crystals and glasses,” *J. Am. Chem. Soc.*, **118** 7209–7214 (1996).

[49]. A. Tandia, N.T. Timofeev, J.C. Mauro, K.D. Vargheese, “Defect-mediated self-diffusion in calcium aluminosilicate glasses : A molecular modeling study,” *J. Non. Cryst. Solids.*, **357** 1780–1786 (2011).

[50]. R. Snellings, “Surface Chemistry of Calcium Aluminosilicate Glasses,” *J. Am. Ceram. Soc.*, **98** 303–314 (2015).

CHAPTER V: TABLE OF CONTENTS

LIST OF FIGURES

LIST OF TABLES

TRIBOELECTRIC PROPERTIES OF CALCIUM ALUMINOSILICATE (CAS) GLASS SURFACES

G. Agnello[a,b18], R. Manley[a], N. Smith[a], W. LaCourse[b] and A. Cormack[b]

g. Science and Technology Division, Corning Incorporated, Corning, NY 14831, USA

h. New York State College of Ceramics at Alfred University, Alfred, NY 14802, USA

ABSTRACT

Recent experiments on flat multi-component glass surfaces have suggested that a particular surface's propensity to absorb water may play a critical role in how that surface accumulates and dissipates electrical charge [1]. It is believed that a key driver for glass surface-water reactivity may be structural defect concentration(s) at the surface, which can be largely influenced by bulk composition. To further explore these hypotheses, a series of CAS glasses were modeled using classical Molecular Dynamics (MD) with the primary goal of understanding how glass composition impacts structural defect concentrations (NBO, under-coordinated Si and/or Al, etc.) in the upper layers (~5Å) of the surface [2]. Concurrently, CAS glass surfaces with the same compositions were prepared in the laboratory and analyzed for charge response at variable humidity using a Rolling Sphere Test (RST) and a newly developed metrology for contact charging phenomena called an Electrostatic Gauge (ESG) [3]. Molecular water interaction with the CAS surfaces was studied using Diffuse Reflectance Infrared Fourier Transform Spectroscopy (DRIFTS). The results of these experiments, along with the corresponding MD calculations, show that glass bulk chemistry and resulting surface defect states (most likely NBO) represent crucial driving factors in how glasses behave when placed in glass-metal contact systems.

Keywords: Charge, contact, flat glass, electrification, surface

[18] Contact: agnellogp@corning.com

1. INTRODUCTION

Flat glass surfaces, as utilized in consumer electronics industries, are specifically prone to charging due to their insulating nature and disproportionately large surface area. This can lead to a plethora of issues within the display manufacturing process including, but not limited to, field induced electrostatic discharge failure of electronic components; particulate based contamination stemming from electrostatic attraction; and electrostatic stiction induced glass breakage during packaging and processing [1,4]. Unfortunately, the physics that dictate both why and how glass surfaces become charged, how charge carriers migrate once located on the surface and how they discharge are all poorly understood. Even the "simple" question "What are the dominant species responsible for charge transfer and conduction on glass surfaces?" does not have a simple answer. We have chosen to attack this complex problem using a combination of theoretical and experimental methods focused specifically on CAS glass surfaces in the high silica portion of the tectosilicate (i.e. charge balanced) join. The CAS ternary system was chosen for two primary reasons. First, because our initial experiments were conducted on complicated many component glass compositions [1], important factors that may be directly related to surface charging are difficult to differentiate. Common sense states that by decreasing the number of components in the glass to three, the data may be easier to understand. Secondly, the CAS system has been studied extensively in the literature and large bodies of structural [2] and electro-chemical (including surface reactivity) [5-10] data are readily available. The purpose of the present article is to report results from experimental measurements done on laboratory fabricated CAS surfaces, and to compare the findings with our previous defect state calculations [2]. We will show data that supports the assertion that glass bulk and surface chemistry largely dictate how surfaces charge when put into contact with another surface (in this case metal). Good correlation is found between RST derived charge rates, DRIFTS data and calculated surface NBO defect concentrations. While there are many available reports in the literature dealing with surface chemistry and/or reactivity of CAS glasses, no body of data exists that focuses on the triboelectric properties of CAS surfaces making this study the first of its kind.

2. EXPERIMENTAL

2.1 Sample preparation

Flat melt surfaces and powders of targeted CAS compositions were generated for RST/ESG and DRIFTS measurements, respectively. The experimental composition-measurement matrix is outlined in table 1

Table 11: List of Generated Sample Compositions, Forms and Measurement/Data Format

CAS(x,y,z)	Form	Measurement	Key metric(s)
CAS(30,30,40) CAS(25,25,50) CAS(20,20,60) CAS(15,15,70)	Melt surface	Rolling Sphere Test (RST), ElectroStatic Gauge (ESG)	Charge rate, surface/metal voltage/charge characteristic
CAS(30,30,40) CAS(25,25,50) CAS(20,20,60) CAS(15,15,70) CAS(10,10,80)	Powder	Diffuse Reflectance Infrared Fourier Transform Spectroscopy (DRIFTS)	Integrated Absorbance (water reactivity)
CAS(25,25,50) CAS(20,20,60) CAS(15,15,70) CAS(10,10,80)	Molecular Dynamics (MD) structures	Simulation, calculation	Surface defect concentration (NBO/cm^2)

Modeled compositions from previous work [2] are also included for comparison. The convention $CAS_{x,y,z}$ where x, y and z indicate CaO, Al_2O_3 and SiO_2 molar percent, respectively, will be used throughout the remainder of the text. Flat "melt" surfaces were fabricated by mixing CaO, Al_2O_3, and SiO_2 batch materials in appropriate proportions (plus 0.015mol%Sb_2O_3 as a fining agent) in Pt crucibles, calcining at 800°C for 6hrs, melting at 1650°C overnight, roller-quenching to produce cullet, then mixing and re-melting at 1650°C before casting flat patties into a block preform. All glasses were annealed at their measured annealing points. Powders for DRIFTS measurement were generated using a combination of mortar grinding / sieve / rotap according to ISO 720, with measurements taken on powders below 270 mesh.

2.2 Measurement techniques

2.2.1 Rolling Sphere Test (RST)

Rolling sphere testing[19] was done at variable relative humidity (~8-45%) using a similar approach as in previous work [1], with a few notable changes. Because the melt surface samples were significantly thick (~20mm), the RST apparatus had to be modified so that the magnet housing and driving motor assembly could be suspended above the surface as opposed to below it. The thickness of the samples prevented the acquisition of suitable signals from the electrode, as well as dampening the magnetic field seen by the sphere to a point where its orbit was uncontrollable. Figures 2a-c show images of the original design as well as the rebuilt system loaded with a CAS surface sample and sphere for charge measurement. All tests were run at 750RPM for 30s. Three measurements of each surface were made by slightly shifting the sample position on the Teflon support and re-measuring what was effectively a different "orbit" on the surface. Charge rates were calculated by using the first 5-10 seconds of peak-valley features and running concatenated linear fits on the values across the three discrete measurements. Lastly, it is worth noting that we observed significant dampening of field strength (i.e. measured charge/voltage) with the electrode suspended above the surface relative to being positioned beneath the glass. This was confirmed by measuring a piece of Corning

[19] Method originally developed by Wiles et al. [11]

EAGLE XG® of normal (0.5mm) thickness under both configurations. Because of this, it is unfortunately not possible to directly compare charge rate data from our previous study with that reported here.

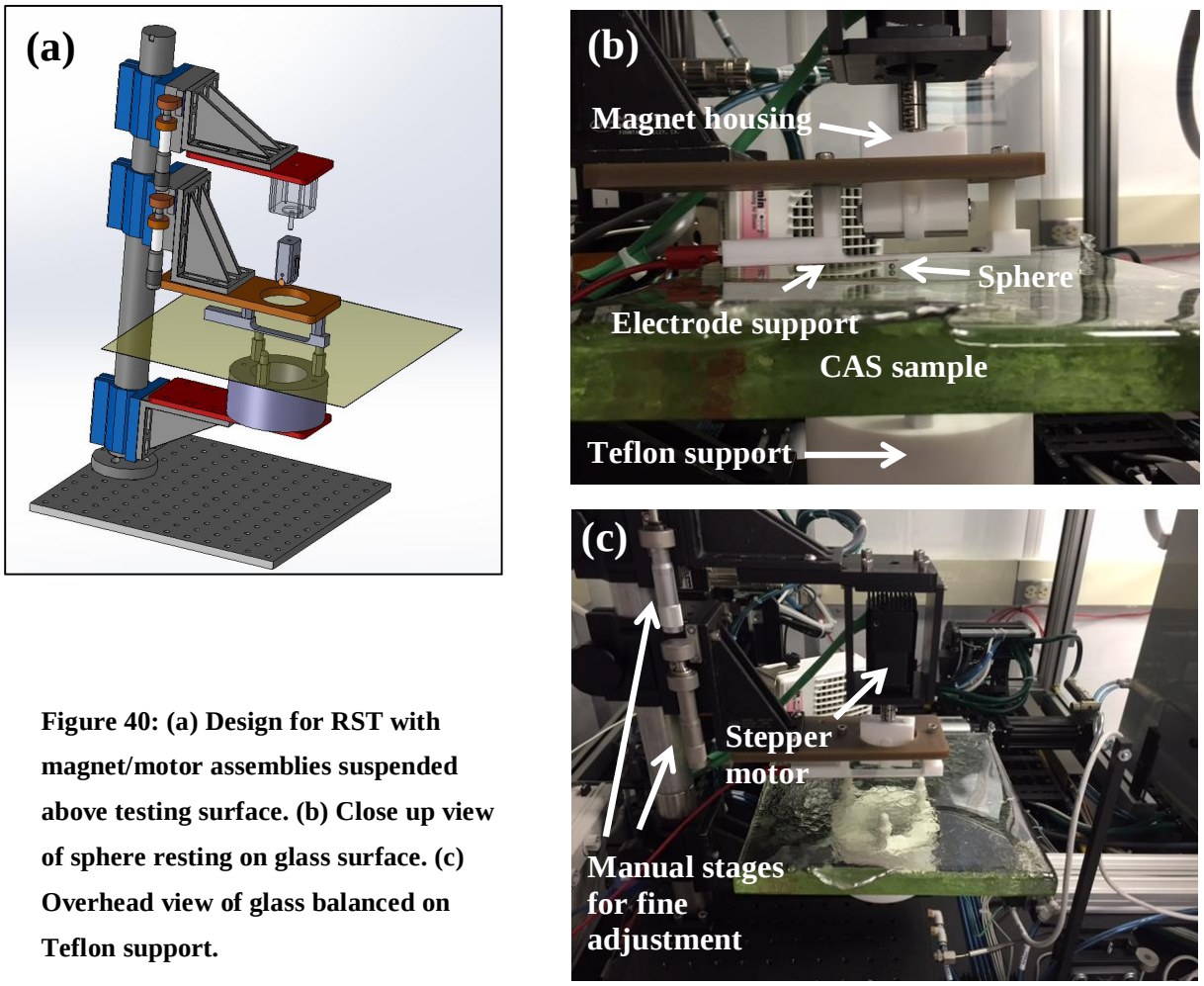

Figure 40: (a) Design for RST with magnet/motor assemblies suspended above testing surface. (b) Close up view of sphere resting on glass surface. (c) Overhead view of glass balanced on Teflon support.

3.2.2 Electrostatic Gauge (ESG)

ESG technology [3] was specifically developed to emulate various types (rolling, vacuum contact, friction, etc.) of tribo-charging mechanisms in a modular, easy to modify platform. The system is comprised of several primary components:

1. An enclosure for precise environmental control of the measurement area consisting of anti-static acrylic side and upper walls, molecular/HEPA filtration of incoming air, and inert gas purge capability

2. Sample stage made of black-anodized aluminum with two vacuum channels for the accommodation of small to large sample sizes (~4”-12” squares). Capable of heating substrates up to 200°C under programmable ramp/cool cycles
3. High current ionizer with static feedback sensor for pre-measurement charge neutralization of the sample surface
4. Fully automated 4 axis (x,y,z,θ) motion system with high resolution (50nm) absolute encoders for ultra-precise positional control of glass “interrogators”. Glass interrogators refer to fixtures intended to contact the surface and initiate a tribo-charging process.

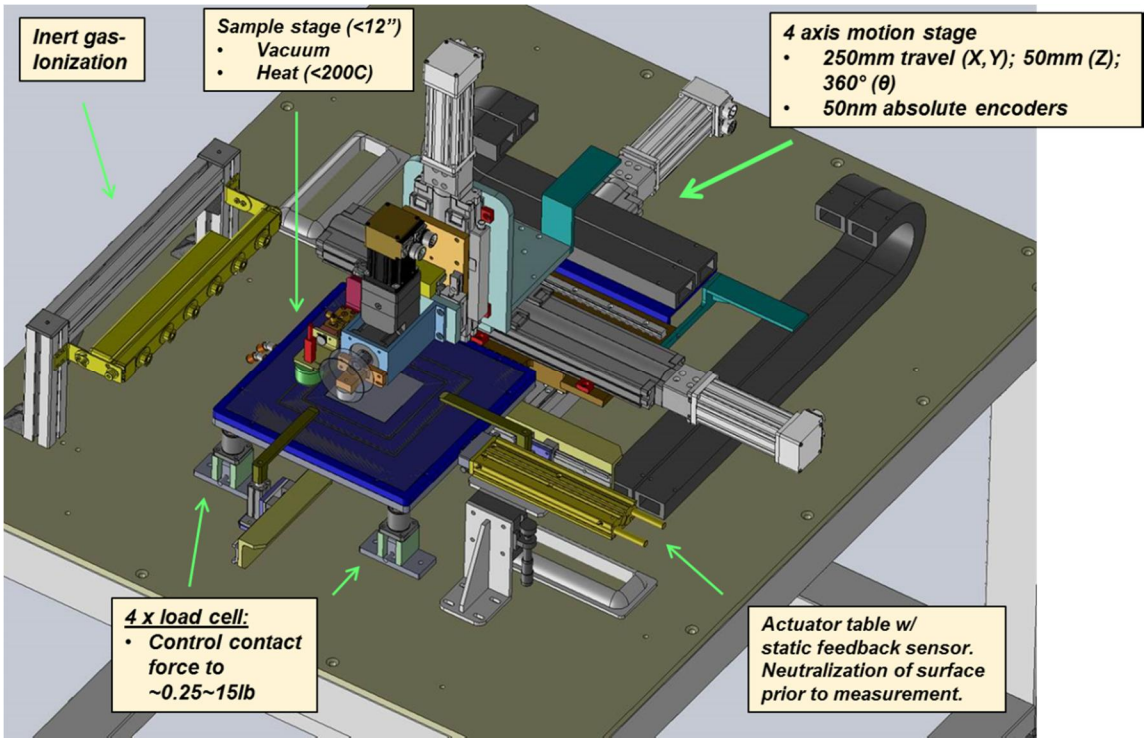

Figure 41: Final design layout for ESG with key features/components labeled.

5. Several measurement sensors set at various positions meant to fully characterize any given charge transfer process

6. Load cells integrated into support legs of the sample stage for precise control of interrogator-glass contact force (0.25~15lb). Feedback loop ensures in-situ maintenance of specified contact force throughout a given measurement sequence.

Figures 2 and 3 show the final system design and fully integrated gauge, respectively. Key components are labeled accordingly.

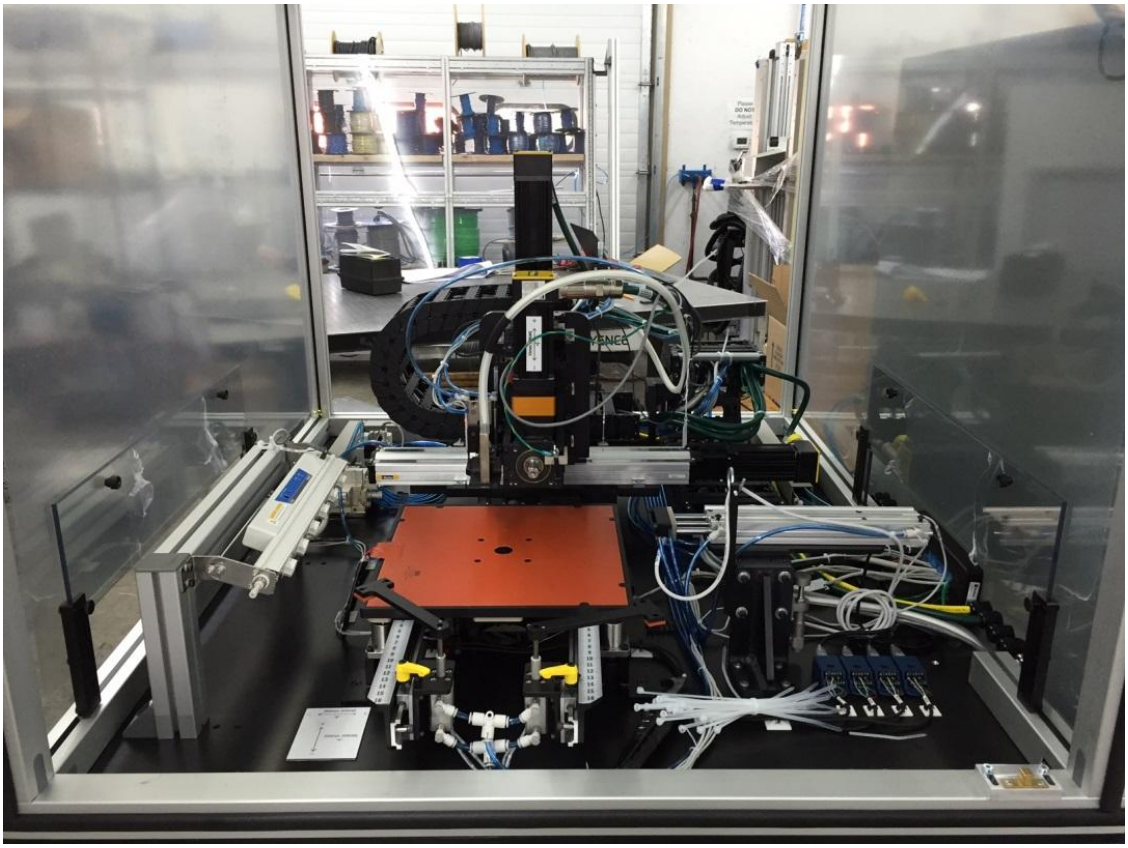

Figure 42: Fully integrated ESG measurement system prior to site acceptance testing

We utilized the ESG roller mode for interrogation of the CAS surfaces[20]. Roller mode was chosen primarily because the mechanical action inherent to this mode is most similar to that of the RST measurement, so comparison between the two techniques was

[20] Roller fixtures include stainless steel, black-anodized aluminum, Teflon and PEEK. Stainless steel roller (3" diameter) was used for all experiments reported here.

thought to be somewhat straightforward. A typical roller measurement is described in the following list and corresponding figures.

1. Roller moves to defined X-Y coordinate on the glass (offset some distance in Y so that the roller will not pass directly over the contact probe). Roller engages the glass surface and moves to a defined contact force. Total engagement force is determined by the summation of the values collected across the 4 load cells integrated into the supporting legs.

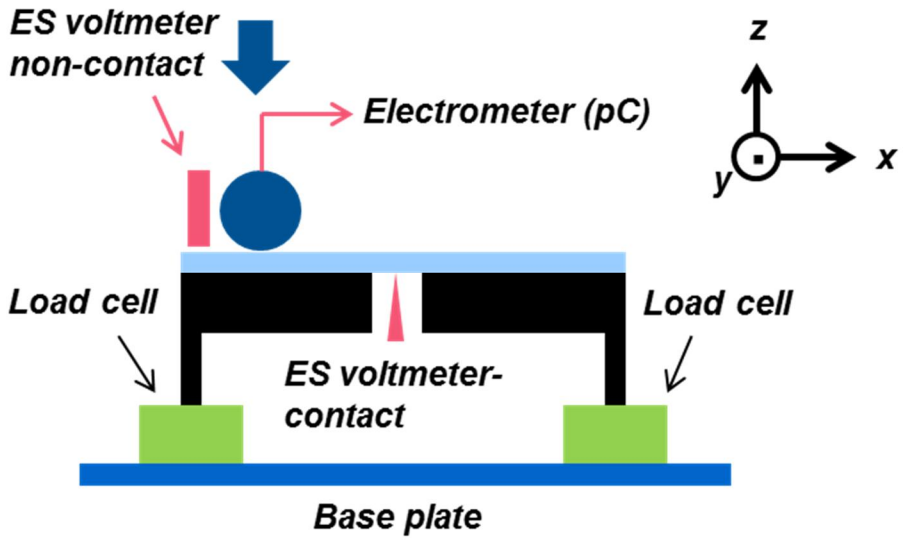

Figure 43: Roller engages glass and moves to target contact load.

2. After a specified time for the roller-glass contact force to rest at the target value, the roller begins to traverse the glass surface in the X direction at a programmed linear velocity. The roller is independently driven by its own dedicated theta drive allowing for precise simultaneous control of its rotational velocity. This allows for the establishment of a parameter called “phase” which is effectively a metric that describes the mixture of “rolling” and “rubbing” action between the roller and glass surface. Phase is defined as $(V_\theta/V_x)*100$, so at a phase of >100% the roller is moving faster around its own axis than in the linear direction, and vice versa. When motion begins, all analog data streams (load, roller position, voltage/charge signals, RH, enclosure temperature, etc.) are

collected with position and/or time stamps. When the interrogator reaches the edge of the sample surface, it reverses course, moving back to its initial position. This is repeated for a specified number of "cycles" where a single cycle is one full +x/-x motion profile. Contact force is maintained throughout the measurement sequence through an active feedback loop between the load cells and the Z drive.

3. After the specified number of cycles is completed, the roller retracts. Additional x-y rows can be programmed for measurement and/or optional post-measurement scans of the surface using the non-contact ES voltmeter for 3D voltage surface mapping can be executed if desired. If no additional rows/post scans are specified, then all drives move to home positions and the measurement surface is ionized for several minutes before removal or re-measurement.

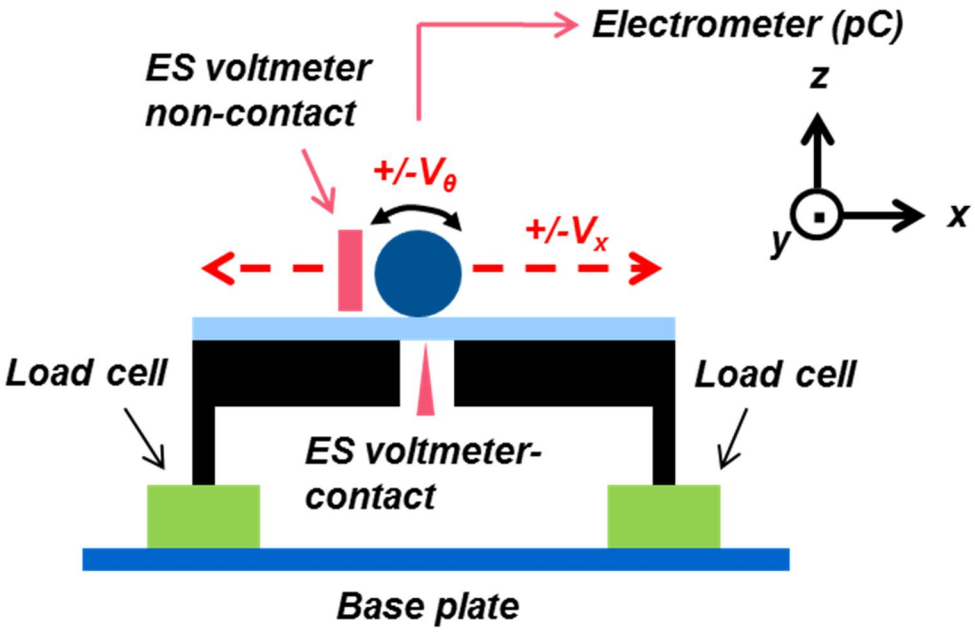

Figure 44: Roller begins motion across the glass surface until it reaches the right edge at which point it returns to its starting position. This is repeated for a specified number of cycles.

As shown in figures 4 and 5, rolling mode testing on ESG provides three main data streams indicative of charge transfer processes. An electrometer (Keithley model 6514) connected to the roller monitors charge accumulation via transfer from the glass. A

non-contact electrostatic (ES) volt meter (Monroe Electronics Isoprobe® model 244A) mounted directly to the drive system and suspended approximately 1mm above the glass follows the linear roller motion. This sensor monitors voltage buildup on the glass immediately following roller contact. Lastly, a contact ES volt meter (Trek Inc. model 820 Infinitron®) monitors voltage on the side of the glass opposite roller contact through a hole in the sample stage. This sensor is stationary; effectively measuring voltage response due to tribo-electrification that occurs some distance away from the point of detection. In a manner of thought, this response reflects motion of charge carriers across the glass (and potentially through it, though this is unlikely given the thickness of the CAS melts). The two volt meters are surface discriminating to a certain extent, meaning that they are measuring two distinct surfaces of the glass; however the spatial/depth resolution of these sensors are not well understood and as such are key focus' of current research efforts.

CAS melt surfaces were measured at low (~8%) relative humidity under the parameters/conditions listed in table 2.

Table 12: Process Parameters for ESG Rolling Mode Testing of CAS Melt Surfaces

Process Parameters for CAS melt surface measurement (all ~8% RH)	**Value**
Phase (%)	110
Linear velocity (mm/s)	25
Cycles (#)	10
Contact force (lbs.)	0.7
Y offset (mm)	30
Stroke length (mm)	100

2.2.3 Diffuse Reflectance Infrared Fourier Transform Spectroscopy (DRIFTS)

Diffuse Reflectance Infrared Fourier Transform Spectroscopy (DRIFTS) is an ideal technique for the study of surface chemistry. The method takes advantage of the wide angle of scatter that results from the interaction of incident radiation with many small particles with irregular shapes. All measurements on CAS powders were made using a Thermo Electron Nicolet 6700 series FTIR coupled with a Harrick praying mantis™ DRIFTS attachment. Samples were heated to approximately 200°C (Harrick model ATC-024 temperature controller) in a high temperature reaction cell for 20 minutes under vacuum to drive off physisorbed water and then cooled to room temperature under a N_2 purge. After a series of room temperature/0% relative humidity spectra were acquired from the "water-free" powders, the humidity was increased to 60% using an SG Instruments RH-200 RH generator under the programmed ramp shown in figure 6.

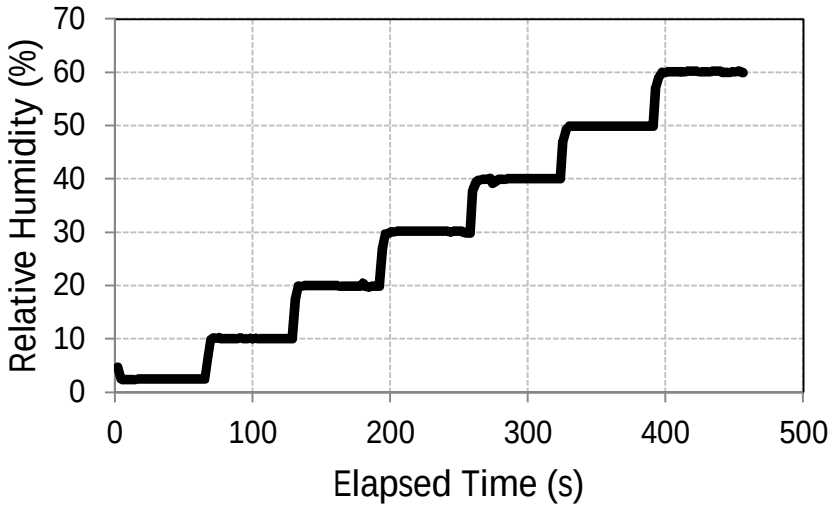

Figure 45: Humidity ramp for DRIFTS analysis of CAS powders. The non-zero data below ~80s are merely placeholders. Actual data begins collection at ~10% RH.

Spectra were collected at regular intervals throughout the ramp and then averaged at each humidity level[21] creating six data points for 10-60%RH in increments of 10%. The

[21] Averaging did not include transient data acquired during initial acclimation of the samples to increased RH%.

data was then background corrected (i.e. self-referenced) to the appropriate 0%RH "dry" spectrum and converted from DRIFTS units (logarithm of inverse reflectance (log 1/R)) to absorbance units. Lastly, reference spectra for gaseous water were subtracted from the data to minimize any effects from residual moisture found inside the optical system. To evaluate physisorbed water at the surface of the CAS powders, we focused on the strong band centered at ~3400cm^{-1}. It has been reported in the literature that this band has at least three (potentially more) primary components corresponding to stretch and/or bend vibrations [12]. The low frequency component (ν_1) is an overtone to the bending vibration found ~1643.5cm^{-1}. The medium (ν_2) and high (ν_3) frequency components correspond to symmetric and asymmetric stretching vibrations, respectively. Component positions and intensities were extracted from the data using a mixed Gaussian/Lorentzian peak fitting procedure (CasaXPS ver. 2.3.16). A sample spectrum with labeled frequency components is shown in figure 7.

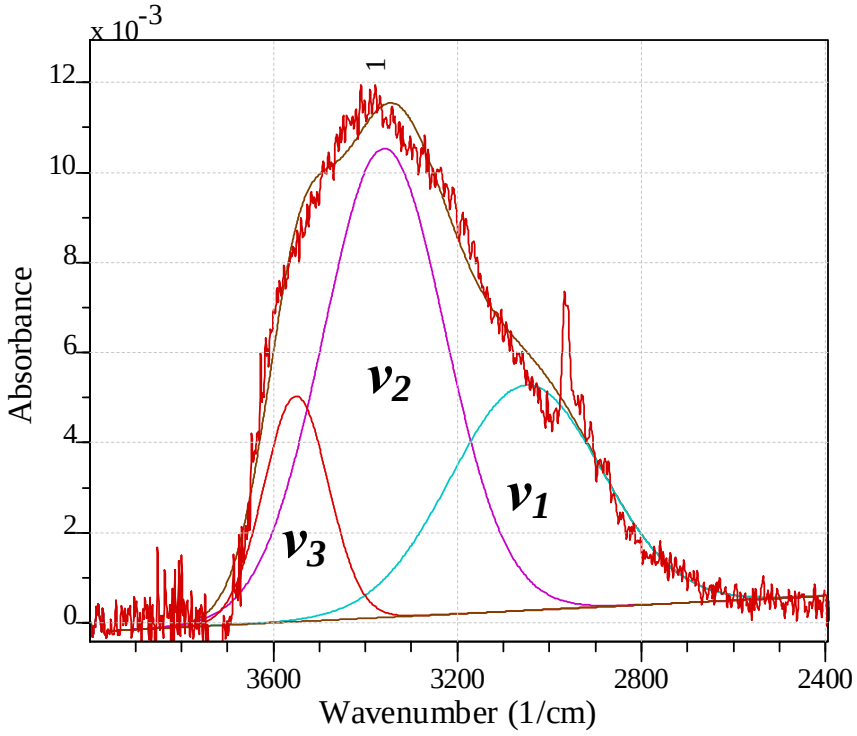

Figure 46: Sample corrected DRIFTS data with low (ν_1), medium (ν_2) and high (ν_3) frequency component fits

DRIFTS data will be presented in terms of integrated component (ν_1, ν_2 and/or ν_3) intensity as functions of humidity for each measured CAS composition.

3. RESULTS AND DISCUSSION

3.1. Triboelectric response(s)

Charge rate data as measured by RST for CAS melt surfaces as functions of relative humidity are shown in figure 8.

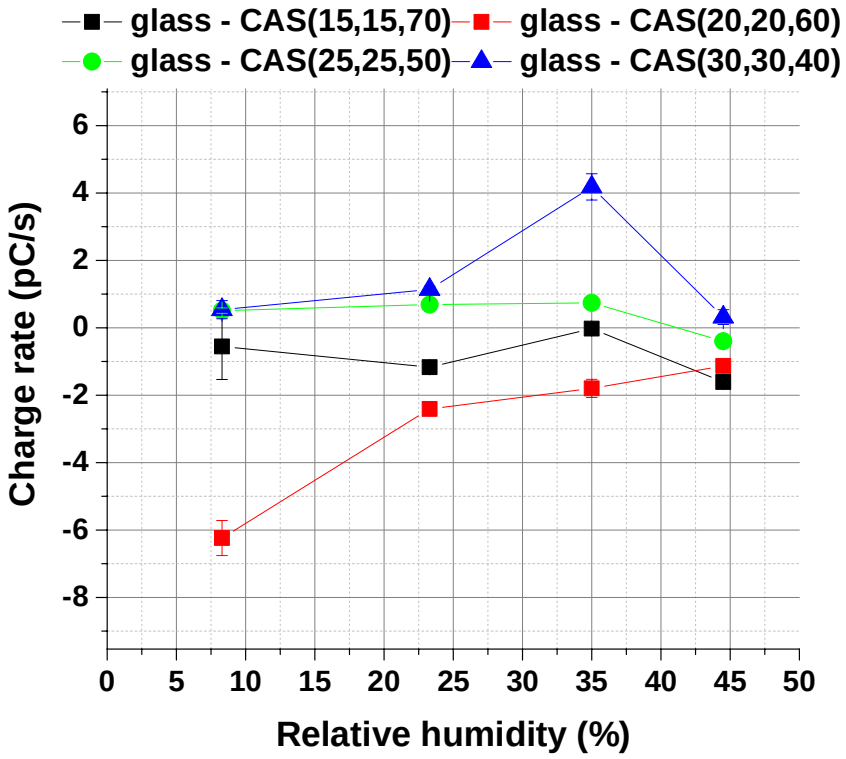

Figure 47: Charge rate data as functions of relative humidity for CAS melt surfaces.

Several aspects of the results shown in figure 8 were somewhat unexpected. Firstly, with the exception of CAS (20,20,60), none of the surfaces showed strong charge rate sensitivity to variations in relative humidity. This result was in contrast to previous data [1] on more complicated multi-component glasses, though as mentioned earlier, these measurements were made under significantly different conditions. With the dampening of signal intensity due to electrode positioning along with a lower magnet speed (750RPM vs. 1000RPM in [1]), any RH dependent charge rate variability may be more difficult to resolve. Perhaps even more surprising than the RH responses were the

differences in the polarity of charge transfer across the four glass compositions. Figures 9a-d show raw RST data for measurements done in ~8%RH for the CAS surfaces in order of decreasing SiO_2 content.

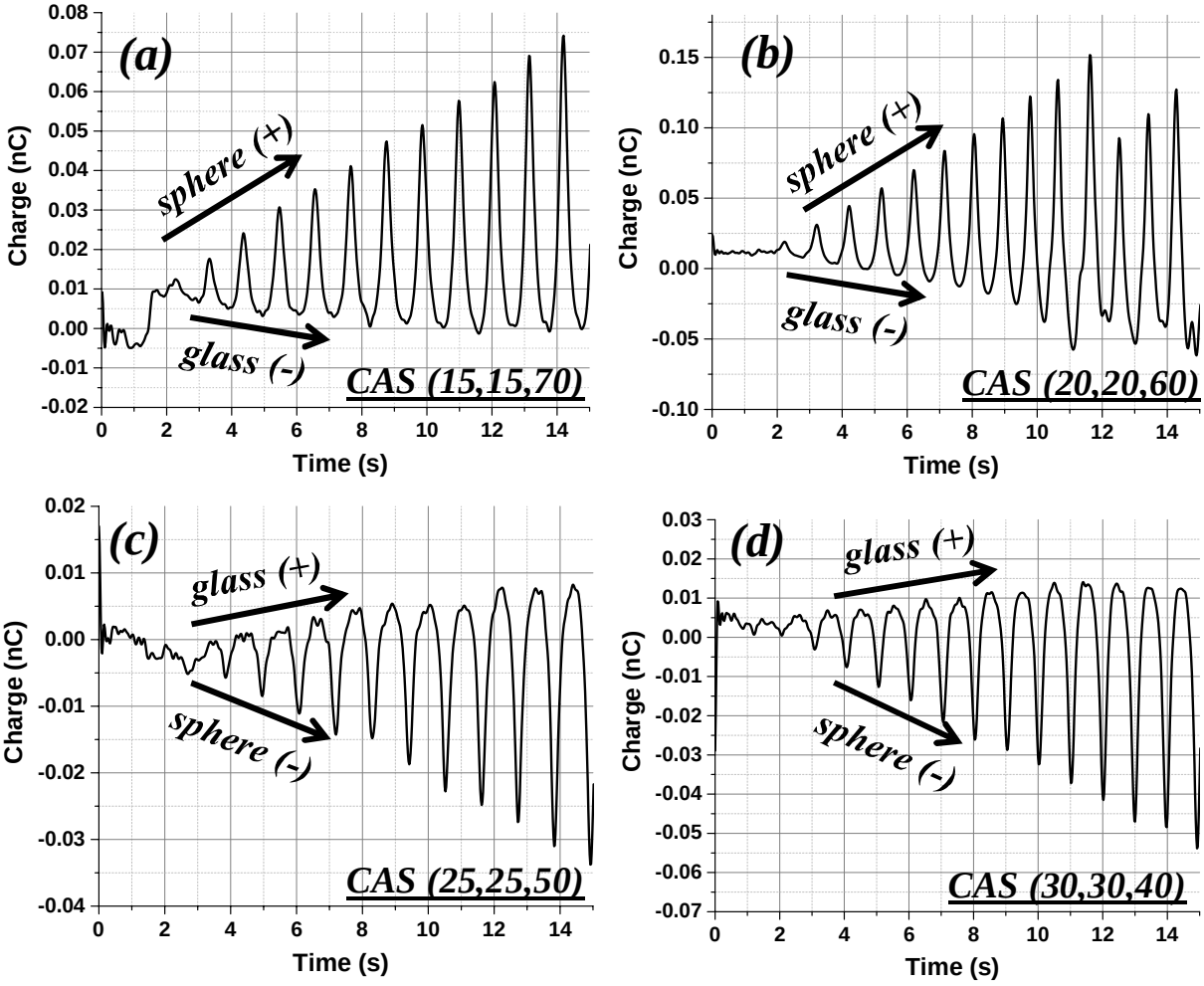

Figure 48: Raw RST data for (a) CAS (15,15,70) (b) CAS (20,20,60) (c) CAS (25,25,50) (d) CAS (30,30,40). Labels on plots show flipped polarity of charge transfer at CAS with ≤50% SiO_2 content.

Based on our proton based charge transfer hypothesis, an increase in negative charge response with decreasing SiO_2 content in the low to medium relative humidity regime may have been a more predictable outcome as opposed to a complete flipping of polarity. This interesting behavior suggests that charging of glass surfaces can be more drastically effected via systematic changes in bulk/surface chemistry than previously thought; even in the complete absence of any form of surface modification and/or treatment whatsoever. Comparing the RST charge rate data shown in figure 8 with calculated surface defect densities from MD simulations [2] further emphasizes the complexity of the underlying physics responsible for these observations. For the comparison, we focused on calculated surface NBO densities (defects/cm^2)[22] primarily because they were the most abundant structural defect found on the simulated surfaces. NBOs also exhibited the widest range of values across the studied composition space. Figure 10 shows charge rate as a function of calculated surface NBO density for the 50,60 and 70% SiO_2 content glasses as measured at the four discrete humidity levels.

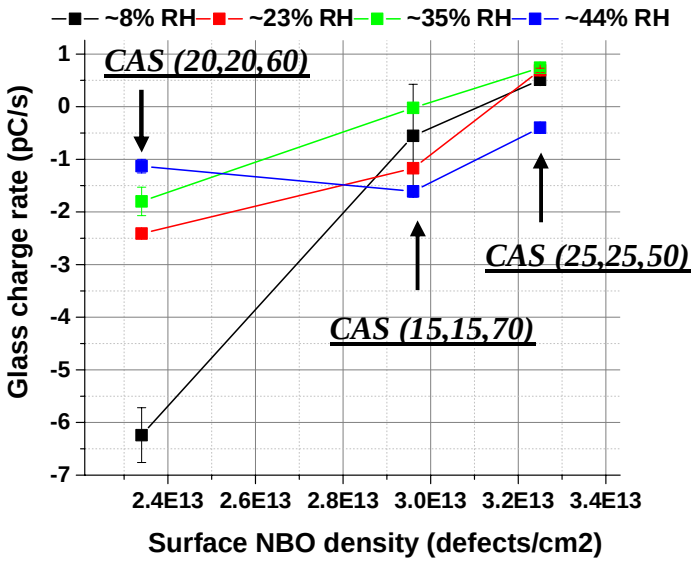

Figure 49: Glass charge rate vs. calculated NBO surface density [2] for 50, 60 and 70% SiO_2 content CAS glasses. 40% SiO_2 content glass was not modeled. The 4 data series represent the 3 glasses measured at 4 different humidity levels.

[22] Values were in units of defects/Å^3 in ref. [2]. Data was converted to more conventional 2D units in this text.

The results suggest that a relationship between the number of NBOs at the glass surface and its measured charge rate does exist, however the observed trend is indicative of increasing charge rate negativity with *decreasing* NBO density. Conversely, as NBO density increases, as shown for the CAS(25,25,50) glass, charge response becomes positive with the exception of the RST data acquired at 44% RH for this glass where the polarity actually flips back to negative. This will be addressed again in latter sections. In general, the results also suggest that as humidity is increased from 8-44%, the sensitivity of charge rate to changes in NBO density decreases. This is shown in figure 11, where "charge rate range" is plotted as a function of RH%. This quantity was computed by simply determining the difference between the highest and lowest measured rates at each humidity, according to the data plotted in figure 10.

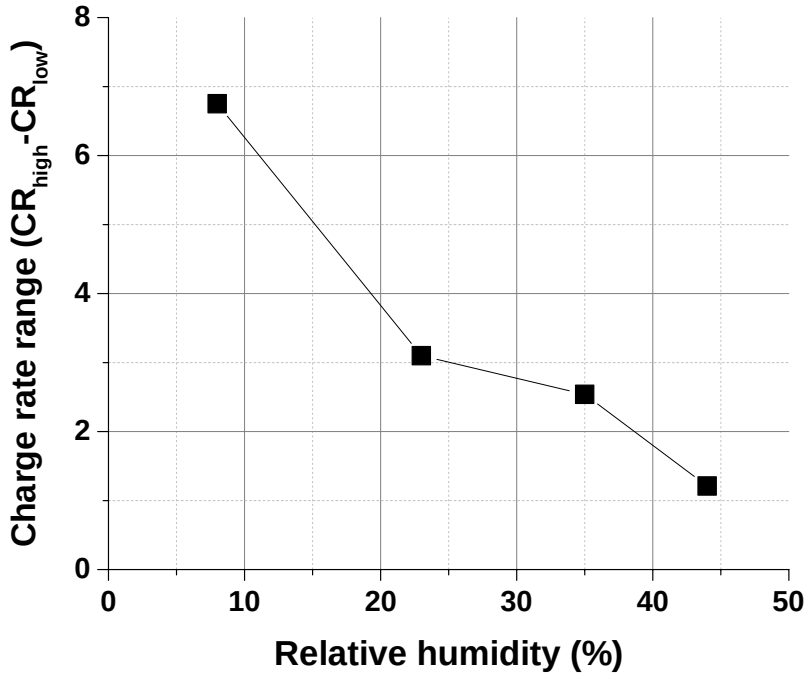

Figure 50: Charge rate range vs. relative humidity.

The data in figure 11 is effectively a metric describing glass surface charging sensitivity specific to NBO concentration as humidity is varied. If we accept the hypothesis that, at

least in part, glass charging is strongly influenced by highly reactive surface sites, then it stands to reason that as a surface becomes progressively more covered in a liquid water layer at higher humidity levels, these sites will be less and less important specific to that surface's charging behavior. Based on this rationale, the result shown in figure 11 could have been reasonably expected.

As a last comment pertaining to the data discussed thus far, it is curious that neither charge rate values nor calculated NBO densities followed linear trends with respect to glass composition. More specifically, the CAS (20,20,60) glass surface exhibited the highest (or perhaps most negative is a more correct description) charge rate of all glasses across most of the measured RH range. Concurrently, the simulated CAS (20,20,60) surface had a lower calculated NBO density than either the CAS (25,25,50) or CAS(15,15,70) MD structures, as indicated in figure 10. Further investigation of these trends, along with our observations of compositionally dependent charge polarity shifts, were primary focuses of ESG experimentation.

As mentioned in the experimental section, ESG rolling mode testing produces several distinct data streams that describe the triboelectrification process from three different perspectives:

1. Charge transfer from glass to roller (metal) via electrometer (EM). This measurement is dynamic in that the sensor directly measures the charge buildup in the roller as it moves.
2. Voltage response of the melt surface immediately post roller interrogation via non-contact electrostatic voltmeter (NC-ESVM). This measurement is dynamic in that the sensor follows the roller.
3. Voltage response of the bottom surface via contact electrostatic voltmeter (C-ESVM). This measurement is static in that the probe is in a fixed position away from the roller-glass contact area.

Each of the CAS samples were measured under the conditions in table 2 at low (~8%) RH. The data presented on the following pages is plotted in three dimensional format

where X, Y and Z axes represent roller position (+/-mm)[23], cycle #[24] and charge response (V or nC), respectively. A "top down" approach is utilized where we will present roller charge behavior first, followed by top and lastly bottom glass surface voltage response.

Figures 12a-d show roller charge accumulation (Q_R) during ESG measurements as functions of position and cycle number in order of decreasing SiO_2 concentration. The results mimic those obtained through RST measurement in a few ways. The polarity of the accumulated charge on the roller was positive for the two highest SiO_2 content glasses and negative for the two lower ones, as labeled in figures 12a-d. This qualitatively correlates with the RST data shown in figure 9. Furthermore, the rank order of charge magnitude was consistent across the two tests. It was pointed out previously that the CAS (20,20,60) glass accumulated charge at a faster rate than any of the other samples. ESG data clearly corroborated this result, demonstrating significantly higher charge accumulation by the roller (~+20nC) during the testing of this glass than any of the other surfaces. The lower SiO_2 content glasses also followed the same rank order as was observed previously, with the roller accumulating approximately twice as much negative charge during testing of the CAS (30,30,40) glass (~-30nC) as compared to the value obtained during the CAS (25,25,50) test (~15nC). Most of the data for CAS (15,15,70), CAS (25,25,50) and CAS (20,20,40) was consistent with respect to roller position as evidenced by the relatively flat charge profiles for each individual cycle. The data for CAS (20,20,60) was significantly different displaying a detailed structure with strong positional dependence. This trending appeared to be consistent from cycle to cycle and was characterized by a broad charge peak/hump centered at the middle of the surface flanked by two dips at the far right and left sides. Top surface voltage response (V_G) profiles as simultaneously measured by the NC-ESVM all exhibited significant structures, though with compositionally dependent shapes. This data is shown in figures 13a-d.

---

[23] 0mm marks the center of the sample stage. Data is from -50mm to +50mm left to right for a total stroke length of 100mm

[24] One cycle is one full left to right back to left motion profile. Data is only collected during left to right motion, though the glass and roller are still in contact during right to left motion.

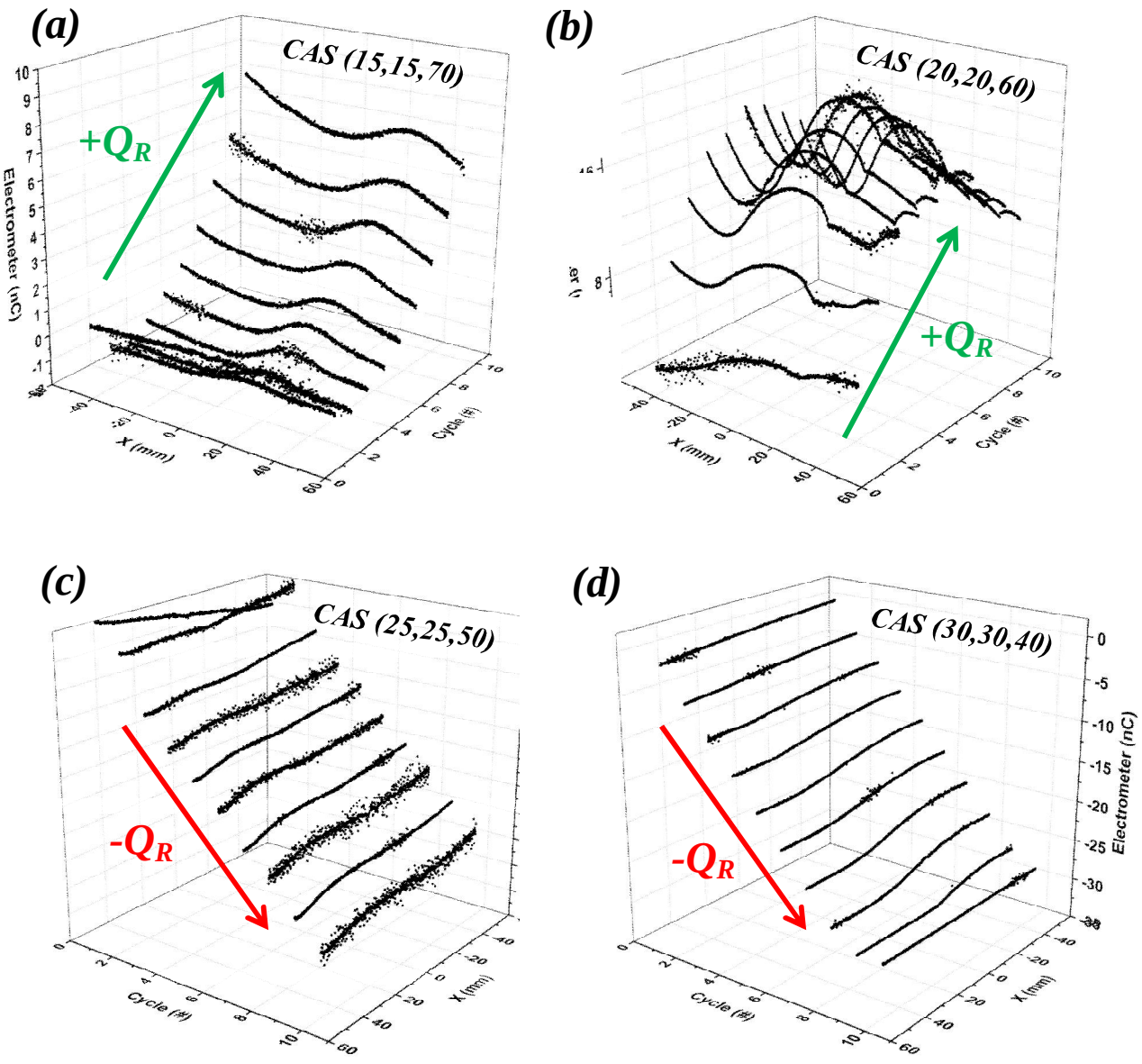

Figure 51: Roller charge accumulation (Q_R) during ESG interrogation of CAS melt surfaces. (a) CAS (15,15,70) (b) CAS (20,20,60) (c) CAS (25,25,50) (d) CAS (30,30,40).

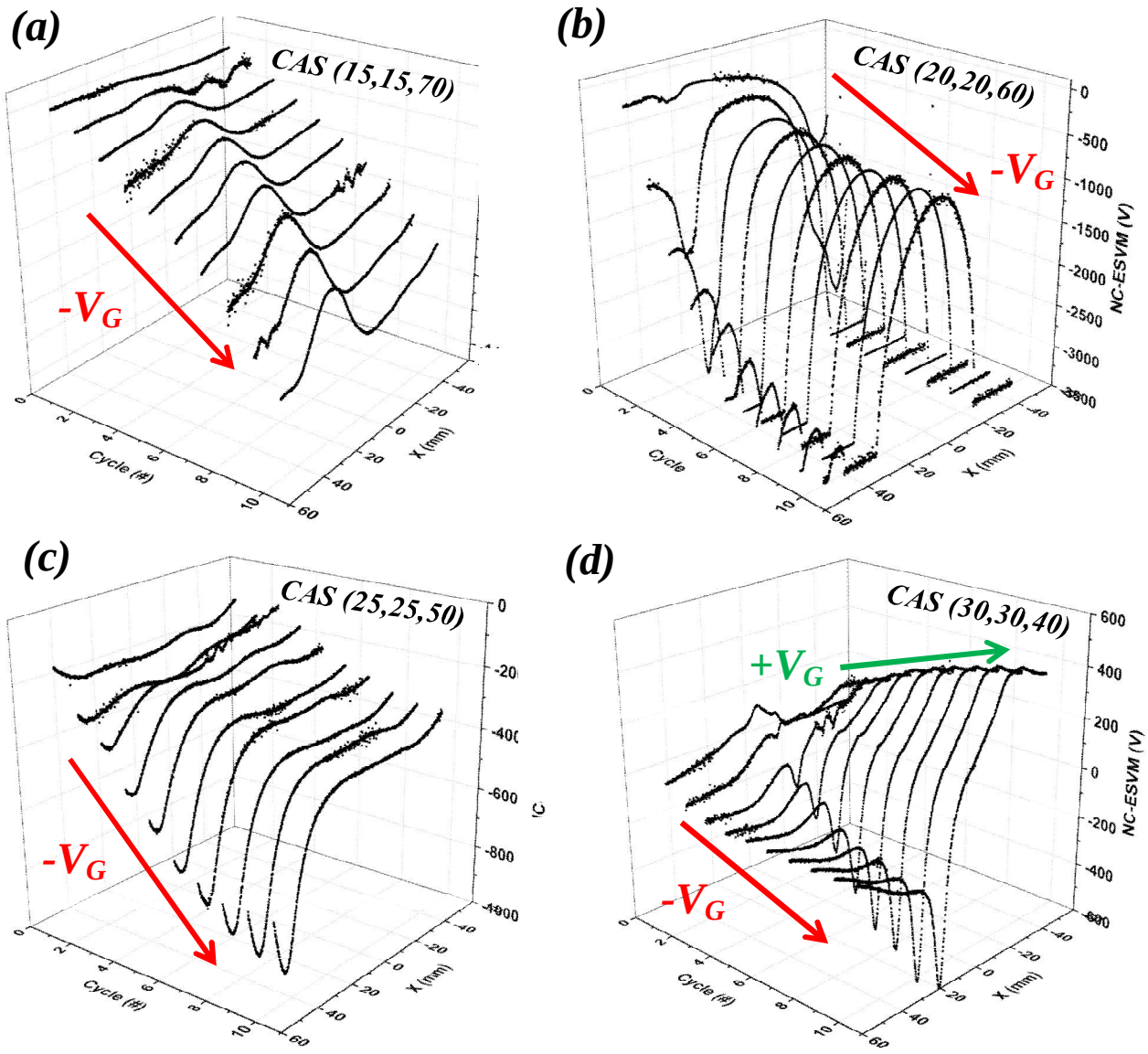

Figure 52: Top glass surface voltage response (V_G) as measured by the NC-ESVM during ESG interrogation of CAS melt surfaces. (a) CAS (15,15,70) (b) CAS (20,20,60) (c) CAS (25,25,50) (d) CAS (30,30,40).

The positional trending of V_G and its relationship to the corresponding Q_R data in figures 12a-d appeared to be strongly dependent on CAS composition. In the case of the high SiO_2 content glasses, the polarity and/or structure of the data correlate well with one another, where overall increases in $+Q_R$ are accompanied by corresponding decreases in $-V_G$. Two dimensional representations of Q_R and V_G for cycle #10 as shown in figures 13a and 13b are used to display this relationship more clearly in figures 14a and 14b. The polarities and rank order magnitudes shown here once again agree qualitatively with our RST results.

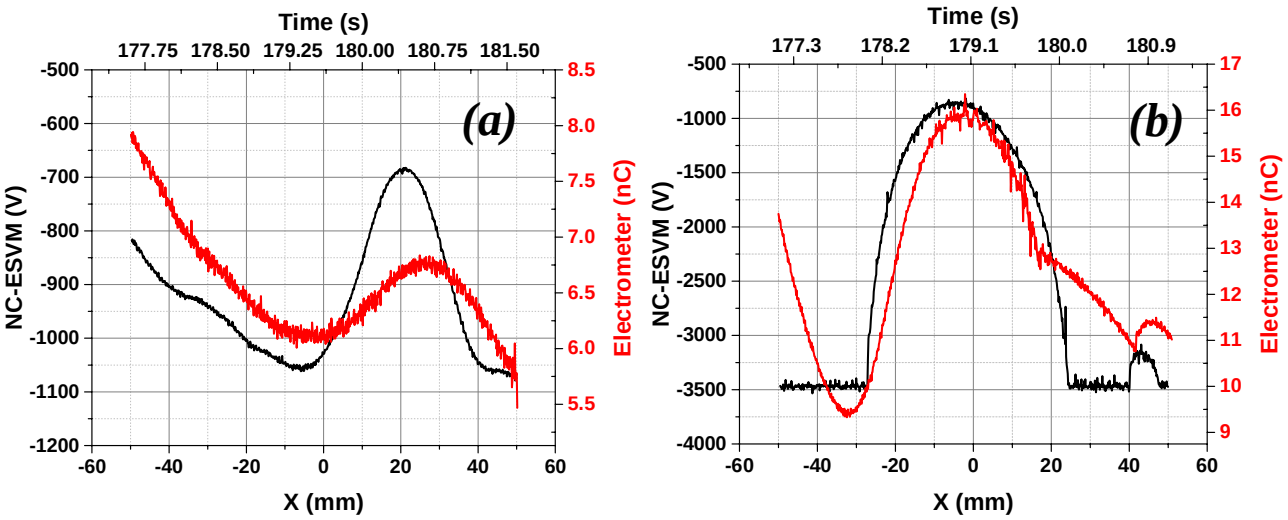

Figure 53: 2D representations of Q_R (in red) and V_G (in black) as functions of roller position and time for (a) CAS (15,15,70) and (b) CAS (20,20,60). The flat V_G data in figure 14b indicates a saturation of the detector below -3500V.

While $+Q_R$ and $-V_G$ trended together in a general sense, local structures in figures 14a and 14b appeared to behave in an opposite manner to what may have been logically expected. More specifically, peaks and valleys in Q_R and/or V_G signals appeared to trend with each other as opposed to moving in directions of opposite polarity.

Comparison of the Q_R and V_G data for the two low SiO_2 content glasses suggested a much different relationship relative to the high SiO_2 glasses, where significant structures were observed in the V_G data but largely void for Q_R.

Furthermore, the overall polarity of the V_G and Q_R responses did not follow expected trajectories relative to one another. For the case of the CAS (25,25,50) measurement, Q_R as well as V_G both became progressively more negative with cycle #. Upon first glance, this behavior (particularly that of V_G) appeared to be contradictory to observations made in RST experimentation, where the glass surface charged positively. Closer inspection of the body of RST data, even that shown in figure 9c and 9d, reveals a subtle but potentially important effect. At certain times, glass charge rates appeared to trend towards zero and even flip to slightly negative values. V_G data acquired from the CAS (30,30,40) glass in figure 13d actually show charge accumulations of both positive and negative polarity from different locations on the surface. These behaviors along with those emphasized in figures 14a and 14b led us to search for additional factors that may have affected charge transfer behavior in these systems.

A key aspect of all ESG test modes is contact force specification and control. Contact force is actively controlled throughout the duration of each measurement by feedback loop between the load cells and Z stage. Roller Z position adjusts in extremely small increments (+/-50nm) in order to maintain the specified value. If the surface being measured does not possess a high degree of flatness, the contact force becomes increasingly difficult to hold. By nature, melt surfaces formed in the manner that our CAS samples were have a gradual “wavy” surface topography that can vary as much as ~0.8mm from one end to another. As such, contact forces as functions of position for these measurements exhibit higher than ideal variability. The effects of contact force on charge transfer in our experimental systems is clearly shown in figures 15a and 15b through a comparison of load and V_G data collected from the CAS (30,30,40) surface. Because of the topographical variation in the glass surface, contact force between the roller and the glass was significantly higher during the +X portion of the measurement than the –X portion. The range of loads shown in figure 15a was similar across the entire sample set The figures show that at low (~<0.8lbs) loads, the glass surface charged positively. As the load increased above this value, the polarity of accumulated charge flipped to negative values; sharply at first as indicated by the negative dip in V_G around +5mm followed by a more gradual progression at higher forces. Similar analyses of contact force and V_G responses for the other CAS surfaces suggest that the

two quantities are closely related; however the trends are compositionally dependent and do not follow the same trajectory shown in figure 15.

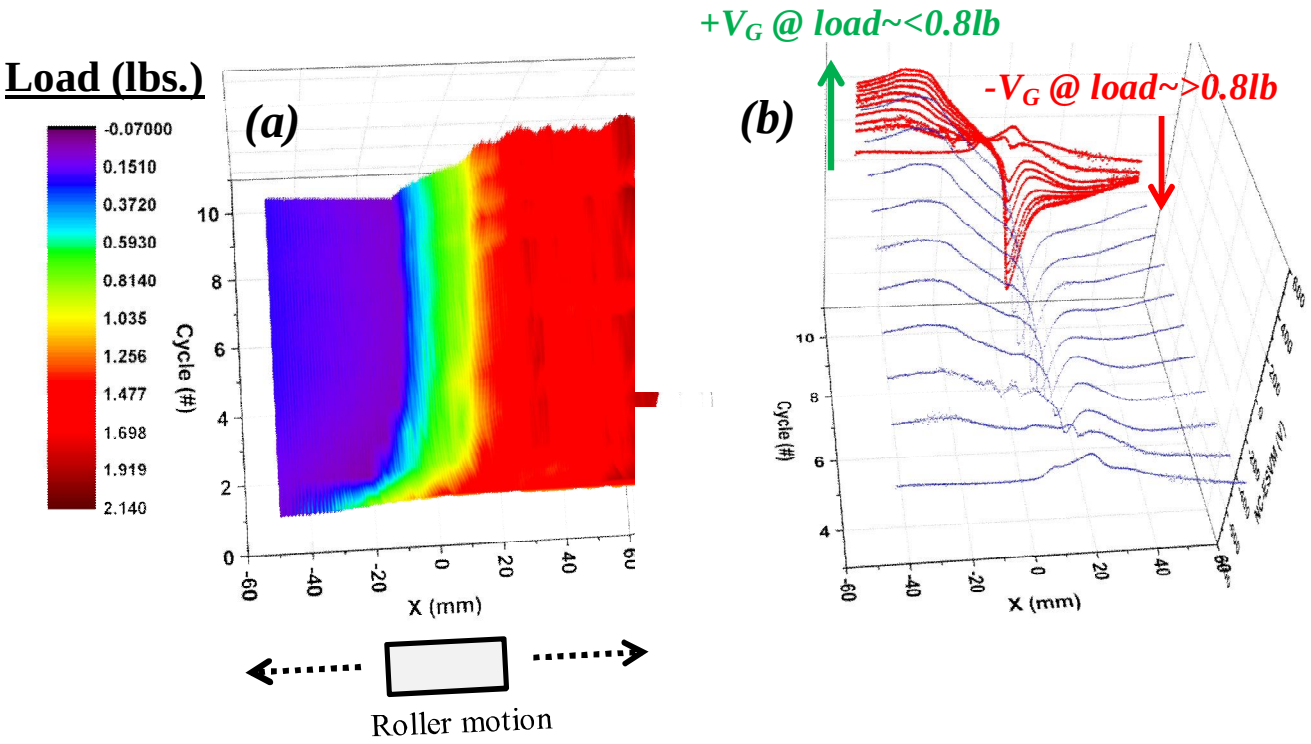

Figure 54: (a) Color surface map showing contact force as a function of roller position and cycle during the measurement of the CAS (30,30,40) glass. (b) NC-ESVM data from fig. 13d re-oriented to show the evolution of V_G more clearly. A YZ projection plot is included in red.

The voltage responses from the bottom glass surfaces as functions of roller position and cycle number, V_{Gbot}, as acquired from the four CAS samples are shown in figures 16a-d in order of decreasing SiO_2 composition. The overall trending of voltage polarity with respect to cycle number correlates well with top surface based V_G measurements, with the exception of the data obtained from the 70% SiO_2 containing glass (fig. 16a). The lack of any observable evolution with cycle number and/or roller position in this data indicates that the probe may have been displaced during the measurement so the experiment would likely need to be repeated for any valid conclusions to be drawn. The low SiO_2 content glass data once again provides the clearest comparison between two experimental quantities, where V_G and V_{GBot} correlate fairly well. Figure 17

expresses the data for cycle 10 (figures 13d and 16d) in 2D format as functions of time and position, similar to that shown in figures 14a-b.

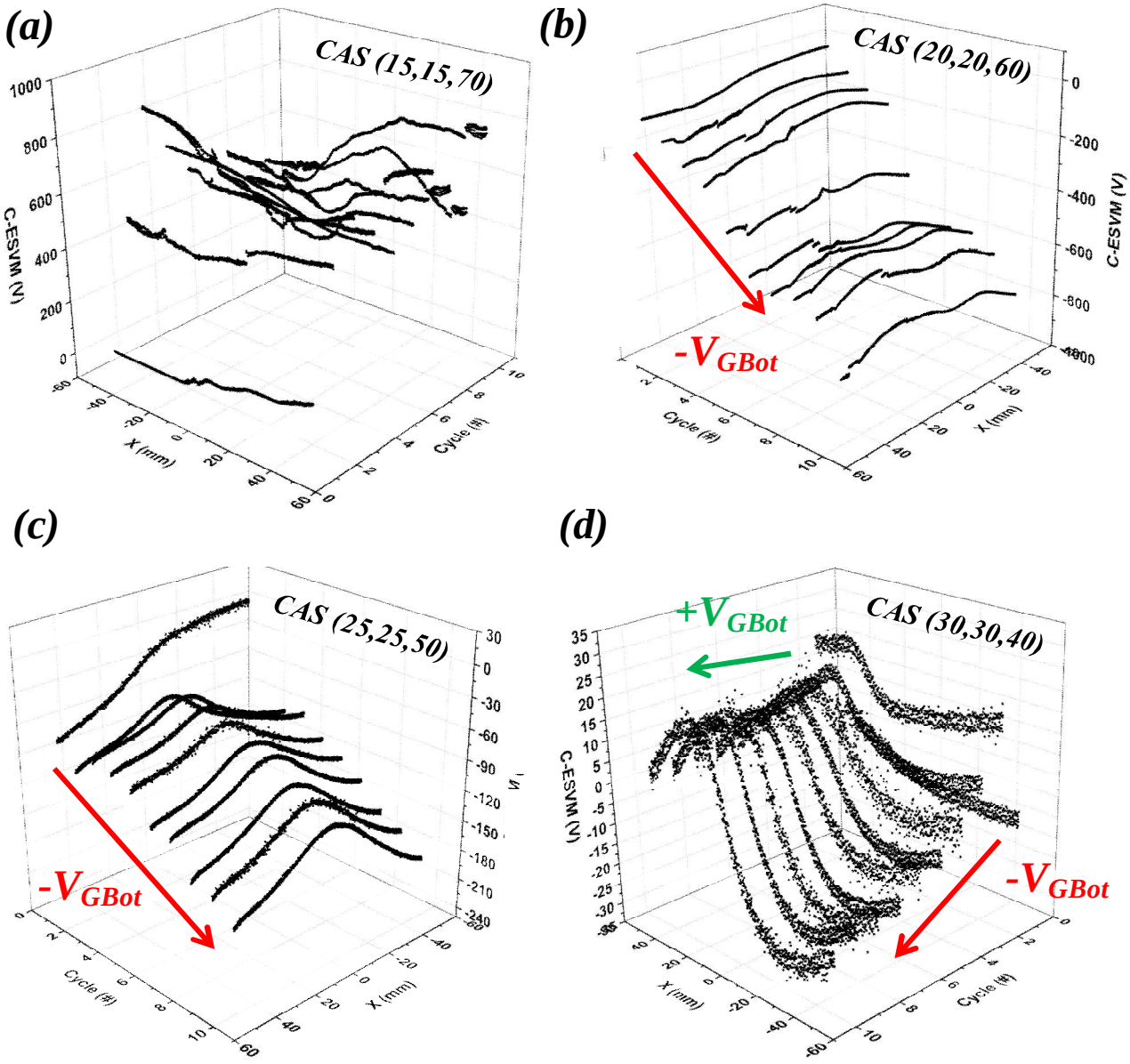

Figure 55: Bottom glass surface voltage response (V_{GBot}) as measured by the C-ESVM during ESG interrogation of CAS melt surfaces. (a) CAS (15,15,70) (b) CAS (20,20,60) (c) CAS (25,25,50) (d) CAS (30,30,40).

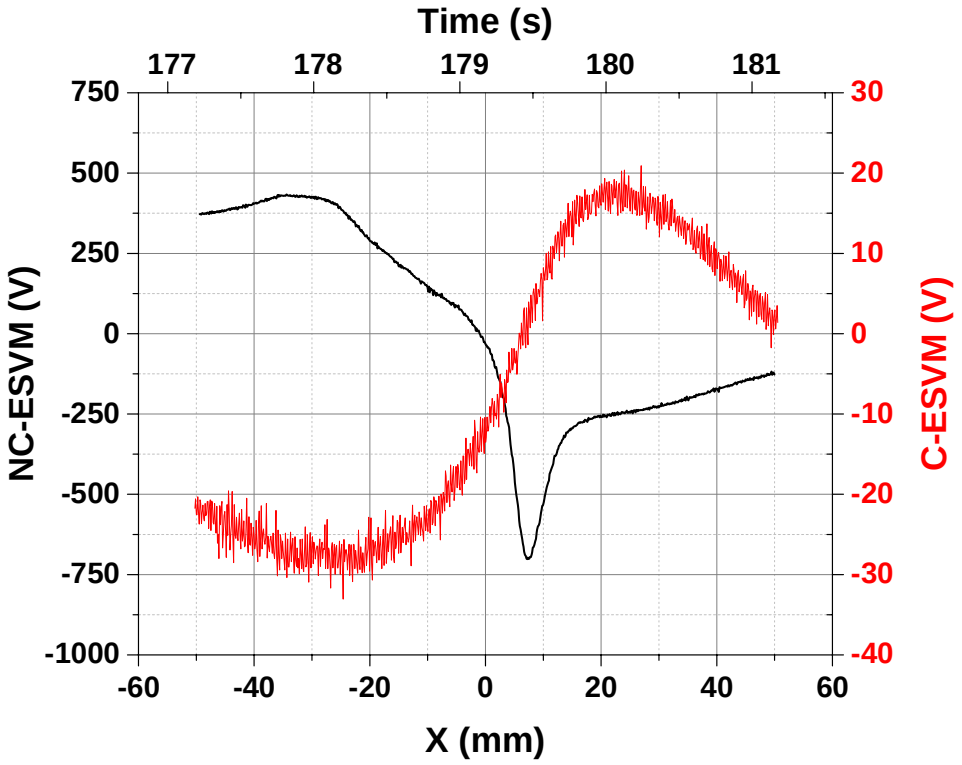

Figure 56: 2D representations of V_{GBot} (in red) and V_G (in black) as functions of roller position and time for CAS (20,20,40).

The data in figure 17 suggests that bottom surface accumulated charge with opposite polarity relative to the top surface. As was the case with contact force and V_G, the additional sample data (with the explained exception of CAS (15,15,70)) suggest some interdependency between V_G and V_{GBot}, though the relationship manifested itself differently for each glass.

The complicated relationships that exist between Q_R, V_G, V_{GBot} and contact force as shown through ESG roller interrogation indicate that contact electrification in these glass-metal systems is largely dictated by the complex interplay of several factors. Furthermore, the nature of these interactions changes easily with variation of glass (or contacting material) composition and/or measurement condition. Additional experimentation will be needed to fully understand these phenomena.

3.2. Water reactivity (DRIFTS results)

As mentioned in earlier sections, many of our hypotheses for how glass surfaces accumulate and dissipate charge are closely related to water reactivity; both in terms of chemisorption (i.e. surface hydroxylation) as well as physisorption (i.e. molecular water absorption). Previous experimental results [1], along with the closely related work presented here thus far, have made notable progress towards the validation of these mechanisms. One significant void in our understanding that required attention is a lack of experimental data specifically quantifying water absorption on glass surfaces. Accurate determination of surface hydroxyl content is quite difficult, and as such it remains an area where our current research efforts are highly focused. Our approach here was focused on understanding the relative propensity for CAS glass surfaces to absorb molecular water.

The CAS powder compositions were all measured using the procedure summarized in section 2.2.3. Figures 18a-c show integrated intensities for the low (ν_1), medium (ν_2) and high (ν_3) frequency components of the main water band ($3700cm^{-1}$-$2600cm^{-1}$), respectively, as functions of relative humidity for each CAS glass. Overall, there were several predictable aspects of the results. Integrated intensities increased systematically for all measured CAS powders as functions of humidity. Intensity trends relative to increases in RH were similar for all measured samples, with the exception of CAS (25,25,50) which exhibited a unique abrupt increase in intensity around 30% RH, that was most noticeable in the high and low frequency component data. This peculiarity is likely related to what was perhaps the most important experimental finding, revealed through comparison of integrated intensity with surface NBO density calculations [2]. Integrated intensities for low, medium and high frequency components as functions of calculated surface NBO concentrations at 10%, 30% and 60% RH are shown in figures 19a-c, respectively. Only 50%-80% SiO_2 glasses are included in figure 19, as CAS (30,30,40) was not modeled. The data suggested that an overall increase in physisorbed water corresponded to an increase in surface NBO concentration for glasses with 60%-80% SiO_2 content. This trend generally held across the RH range exhibiting similar data characteristics in all three plots, and would have likely been expected based on our surface defect facilitated charge transfer hypotheses [1]. The results for CAS

(25,25,50), however, pointed to a decrease in physisorption at all three humidity levels, despite having the highest concentration of NBOs at the surface.

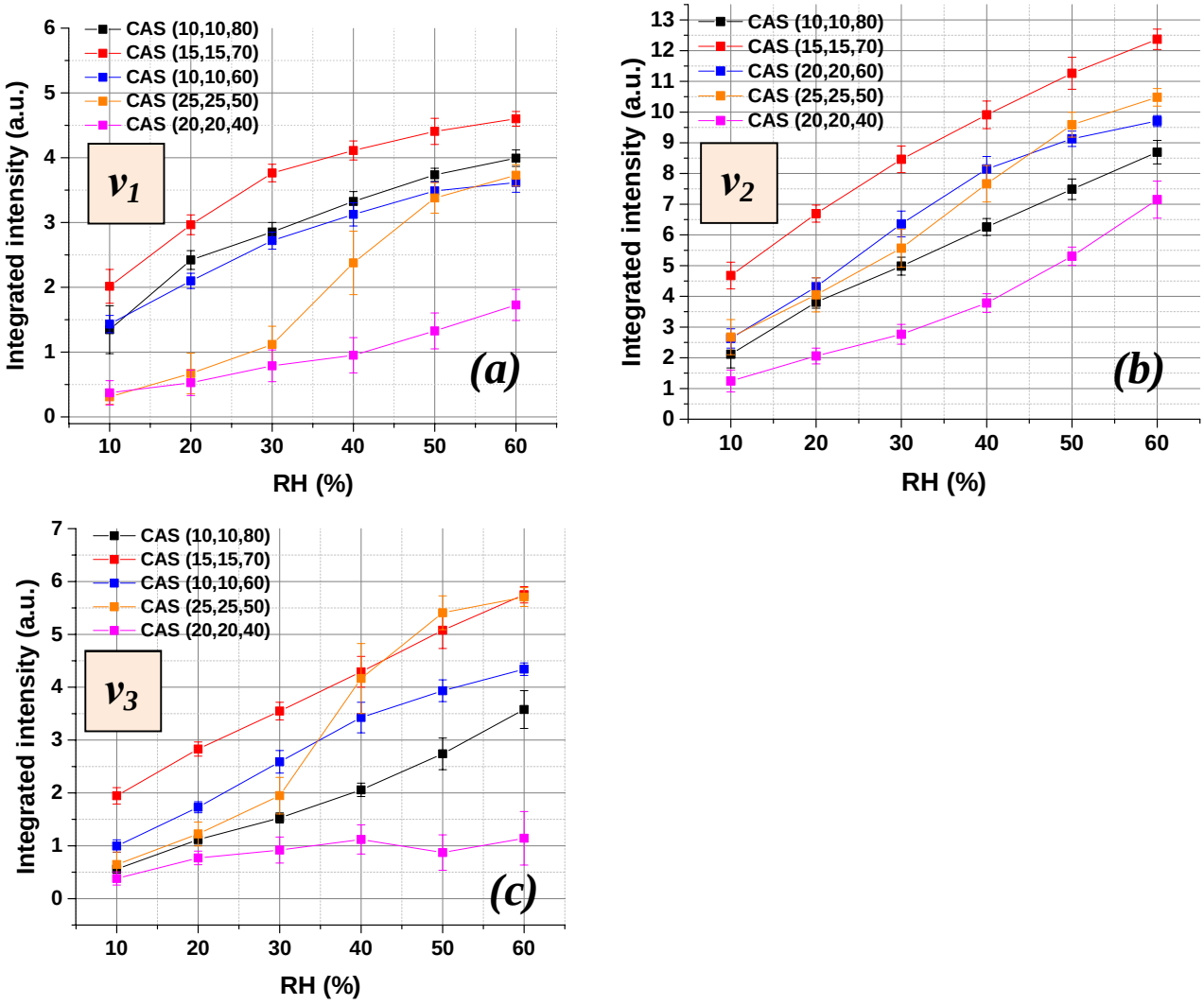

Figure 57: Integrated intensities for low (a), medium (b) and high (c) frequency components of the primary water absorption band.

Even though the CAS (30,30,40) glass was not modeled, the data in figures 18a-c suggest the trend would continue based on this glasses' low overall intensities. This behavior coupled with the observed polarity shifts in RST data and the clear differences in charging behavior during ESG interrogation lead us to believe that the dominant mechanisms responsible for charging in this system experience a fundamental shift as

SiO_2 content reaches some critical level. Gathering additional information to help explain these observations will be a subject for future work.

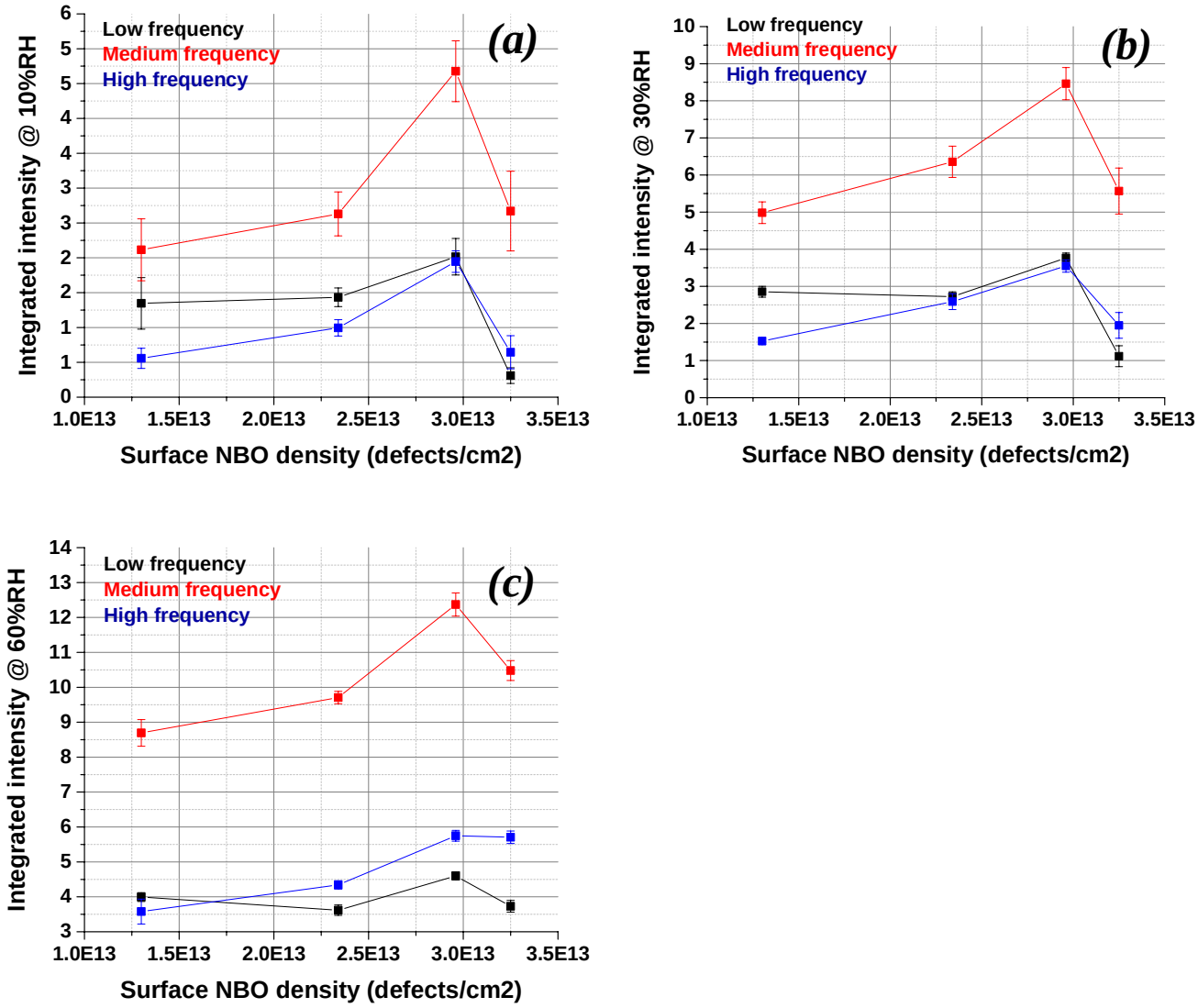

Figure 58: Integrated low, medium and high frequency component intensities as functions of calculated surface NBO densities (MD simulations) at (a) 10% RH (b) 30%RH and (c) 60%RH.

4. CONCLUSIONS

Triboelectric properties of CAS glass surfaces (compositions along the tectosilicate "charge compensated" join) were studied using a combination of experimental and theoretical methods. The Rolling Sphere Test (RST), Electrostatic Gauge (ESG) roller testing and DRIFTS analysis were used to investigate charge transfer behavior as functions of measurement environment (i.e. relative humidity), glass chemistry and variable contact dynamics (i.e. contact force, time, etc.). The data suggest that contact charging is heavily dependent on glass chemistry, where accumulated charge polarity can actually flip in measurements of CAS surfaces with low ($\leq$50%) SiO_2 content. Contact force appears to play a significant role in charge processes as well, having variable effects that are strongly dependent on glass composition. RST and DRIFTS data correlate well with MD based surface NBO density calculations, which partially helps validate the hypothesis that surface charging is strongly related to the reactivity of surface defect sites. Future work will focus on the development of methods to evaluate glass surface hydroxylation, expanding the chemical space of studied glass systems and continued efforts in reactionary modeling.

5. ACKNOWLEDGEMENTS

The authors would like to thank the Corning Display Technologies (CDT) development and fundamental research organizations for funding this work. We would also like to acknowledge Peter Knowles and Susan Warrick for valuable design and/or laboratory support.

6. REFERENCES

[1]. G. Agnello, J. Hamilton, R. Manley, E. Streltsova, W. LaCourse, A. Cormack, "Investigation of contact-induced charging kinetics on variably modified glass surfaces," *Appl. Surf. Sci.,* **356** 1189–1199 (2015).

[2]. G. Agnello, R. Youngman, L. Lamberson, N. Smith, W. LaCourse, A. Cormack, "Bulk and surface structure of silica rich calcium aluminosilicate (CAS) glasses along the molar CaO/Al2O3 = 1 join via Molecular Dynamics (MD) simulation," *To be submitted*

[3]. G. Agnello, "Method and Apparatus for Measuring Electrostatic Charge of a Substrate," USPP # 62/262638, 2015.

[4]. B. Denson, "An electrostatic discharge model for thin-film transistor fabrication," *J. Soc. Inf. Disp.*, **23** 91–96 (2015).

[5]. M.J.A. Qomi, M. Bauchy, F.-J. Ulm, R.J.-M. Pellenq, "Anomalous composition-dependent dynamics of nanoconfined water in the interlayer of disordered calcium-silicates," *J. Chem. Phys.*, **140** 054515 (2014).

[6]. C.A.M. Siskens, H.N. Stein, M. Stevels, "Surfaces of Silicates in Contact with Alkaline Aqueous Solutions II," *J. Colloid Interface Sci.*,**52** [2] (1975).

[7]. M. Gautier-Soyer, H. Cruguel, M.J. Guittet, O. Kerjan, F. Bart, L. Bois, "Surface Analysis of Oxide Glass Surfaces", *J. Surf. Anal.*, **9** 446–450 (2002).

[8]. R. Snellings, "Surface Chemistry of Calcium Aluminosilicate Glasses," *J. Am. Ceram. Soc.*, **98** 303–314 (2015).

[9]. D.A. Weirauch, D.P. Ziegler, "Surface Tension of Calcium Aluminosilicate Glass Using Computerized Drop Shape Analysis," *J. Am. Ceram. Soc.*, **79** 920–926 (1996).

[10]. F. Bouyer, G. Geneste, S. Ispas, W. Kob, P. Ganster, "Water solubility in calcium aluminosilicate glasses investigated by first principles techniques," *J. Solid State Chem.*, **183** 2786–2796 (2010).

[11]. J. A. Wiles, B. a. Grzybowski, A. Winkleman, G.M. Whitesides, "A tool for studying contact electrification in systems comprising metals and insulating polymers," *Anal. Chem.*, **75** 4859–4867 (2003).

[12]. SYu Venyaminov, F.G. Prendergast, "Water (H_2O and D_2O) molar absorptivity in the 1000-4000 cm-1 range and quantitative infrared spectroscopy of aqueous solutions," *Anal. Biochem.*, **248** 234–245 (1997).

Closing Remarks and Future Directions

It is my sincere belief that the work outlined in this dissertation has contributed greatly to our overall fundamental understanding in the area of electrostatic properties and behavior of multi-component glass surfaces. With this being said, the truth is that in many ways we have created more questions than answers, though this is generally the way that most great science comes about. As this work was done with industrial interests in mind, the overall program will continue, using much of our discourse here as a launching pad of sorts. So in closing, I would like to summarize a few key areas that were not covered extensively in this thesis, but will comprise much of the related work in the near term as well as looking forward into the future.

1. Ultimately, we would like to understand why (and if) contact charging in these systems directly leads to electronic device failure in a display fabrication process. Our work dealt exclusively with why and how the surfaces charge in the first place, and not necessarily with "connecting the dots" to the end product. Specific programs will deal with this unique set of questions.

2. Much of our main hypotheses point to surface chemistry as the primary driver for glass surface charging behavior. While we have a significant body of data that supports this indirectly, we have yet to study these surfaces completely from a dedicated analytical perspective. Much of our work in the near term will be focused on the development of analytical methods to quantify the surface chemistry of various multi-component glasses at the "nano" level. Efforts are currently underway in the areas of TOF-SIMS, Low Energy Ion Scattering (LEIS) and "vacuum fracture" XPS techniques amongst others.

3. Water interaction was a recurring theme throughout this thesis, however we have yet to gain deep fundamental understanding of the hydroxylation behavior of these surfaces. Since we believe chemisorption is a vital mechanism related to surface charging, further study in this area is essential. There are significant efforts currently to develop IR, as well as NMR, spectroscopic techniques with the express purpose of

glass surface hydroxyl quantification. The ultimate goal is to better understand reactionary dynamics between glass surfaces and environment.

4. From a theoretical perspective, developing reactionary models will provide an enormous amount of information concerning many of the mechanisms that we believe take place at the surface of glasses. Much of the data can and will be used to validate and/or complement important ongoing experimental work. We are in the process of initiating an SRA between Corning Incorporated and Alfred University for this express purpose.

5. Several types of novel tribo-charge metrologies have been developed over the past several years. Many of these techniques, such as the Electrostatic Gauge, are in the early stages of process development. In fact, the work summarized in chapter 5 of this thesis represents the first extensive experimentation using this technology. As such, measurement process, protocol and capability development for these new systems will receive significant attention over the near to long term.